INAUGURAL-DISSERTATION

zur

Erlangung der Doktorwürde

der

Naturwissenschaftlich-Mathematischen Gesamtfakultät

der

Ruprecht-Karls-Universität Heidelberg

vorgelegt von

Dipl.-Phys.   Dirk Engelmann
aus   Tübingen

Tag der mündlichen Prüfung: 26. Juli 2000

3D-Strömungsmessungen

mittels Stereo Bildverarbeitung

Gutachter: **Prof. Dr.** **Bernd Jähne**

Prof. Dr. **Kurt Roth**

Dissertation
submitted to the
Combined Faculties for the Natural Sciences and for Mathematics
of the Rupertus Carola University of
Heidelberg, Germany
for the degree of
Doctor of Natural Sciences

3D-Flow Measurement
by Stereo Imaging

presented by

Diplom-Physicist: Dirk Engelmann
born in: Tübingen, Germany

Heidelberg, July 26, 2000

Referees: Prof. Dr. Bernd Jähne
                      Prof. Dr. Kurt Roth

Summary

A new method to record three-dimensional liquid flow fields by using 'Particle Tracking Velocimetry' is presented. It is based on a two-dimensional Particle Tracking Velocimetry method. It was extended to the third space dimension in order to include the complete physical space. This procedure allows to determine the Lagrange-flow field and to calculate from it the Euler-velocity flow field obtained from many other flow measuring techniques.

A calibration method was developed for the wind-wave-flume which allows a high resolution in space. The stereo camera setup and the experimental setup were optimized for the liquid flow measurements. For the first time a liquid prism and a Scheimpflug-camera geometry was used.

Numerical calculations using the finite element method demonstrate the complexity of the problem of dealing with free surfaces with wind-induced shear forces as a boundary condition. They show clearly that experimental studies are indispensable for describing phenomena such as 'bursts' (descending of liquid elements from close to the surface into deeper layers).

Flow measurements were performed in a newly constructed wind-wave-flume (AEOLOTRON) and in a smaller predecessor by using the newly developed imaging methods. In this way the flow fields of wind driven water waves could be characterized by the velocity field and the 'turbulence' conditions.

Zusammenfassung

Ein neues Verfahren zur Messung des dreidimensionalen Strömungsfeldes mittels 'Particle Tracking Velocimetry' wird vorgestellt. Ein zweidimensionales Particle Tracking Velocimetry liegt dem Verfahren zugrunde. Es wurde auf die dritte Raumdimension erweitert, um den gesamten physikalischen Raum zu erfassen. Dieses Verfahren erlaubt, das Lagrange´sche Strömungsfeld zu bestimmen, woraus auch das von vielen anderen Verfahren erhaltene Euler´sche Geschwindigkeitsfeld berechnet werden kann.

Das für den Einsatz am Wind-Wellen-Kanal entwickelte Kalibrierverfahren ermöglicht eine hohe räumliche Auflösung. Der Stereokamera-Aufbau und der Versuchsaufbau wurde für die Strömungsmessungen optimiert. Dabei wurde erstmals ein Flüssigkeitsprisma und eine Scheimpflug-Kamera-Anordnung eingesetzt.

Numerische Rechnungen unter Verwendung der finite Elemente-Methode zeigen die Komplexität des Problems, freie Wasseroberflächen mit windinduzierten Scherkräften als Randbedingung zu behandeln. Sie machen deutlich, daß experimentelle Untersuchungen unerlässlich sind, um Phänomene wie 'bursts' (Abtauchen von oberflächennahen Flüssigkeitselementen in tiefere Schichten) zu beschreiben.

Strömungsmessungen wurden an einem neu konstruierten Wind-Wellen-Kanal (AEOLOTRON) und am kleineren Vorgängermodell mit dem neuentwickelten Bildverarbeitungsverfahren durchgeführt. Die Strömungsfelder von windinduzierten Wasserwellen konnten auf diese Weise Geschwindigkeitsfeld und "Turbulenzzustand" charakterisiert werden.

Contents

Chapter 1

Introduction

The major part of the earth is covered by oceans. Gas from the atmosphere is transported into the oceans due to exchange processes at the surface. For gases such as CH_4, O_2 or CO_2 the oceans are a major sink. About 90% of the global CO_2 is dissolved in the oceans. But the amount of CO_2 - one of the most important gases concerning the prediction of climatic changes - transfered from the atmosphere to the oceans is still uncertain and under debate. Estimations deviate by ± 2 Gt from 4 Gt. The concentrations of these gases in the atmosphere influence the climate significantly. It is therefore important to understand air-sea related gas exchange processes.

The atmospheric gas has to pass the air-water phase boundary and the amount of gas transported per time is characterized by the *transfer velocity*. The transfer through the air-water boundary is controlled by a microscopic layer (20-300 μm, Münsterer [1996]) at the water surface in which molecular diffusion is the dominating transport process. Beneath this layer *turbulent transport* is the far more efficient transport mechanism. Water waves affect the gas transport and they show a large variety of different types. On a scale of some centimeters up to several kilometers gravitational waves appear where gravitation is the restoring force. On a smaller scale of millimeters up to centimeters capillary waves show up. Here the surface tension is the restoring force. If air flows over the free surface of the liquid and capillary waves are generated, the transfer of gas in the liquid is considerably increased. The appearance of wind driven water waves is clearly associated with an increase in the gas transfer rate. This effect is well known, but the underlying physical mechanisms are not fully understood. The parameterization of the surface shape is an attempt to characterize the gas transport. The mean square slope was found by Jähne [1985] to be an important parameter. Furthermore the liquid flow field is of importance in order to understand the physical mechanisms in more detail. Air-water gas transport is also important in the field of chemical engineering. For instance gas-liquid reactors are frequently used where the transport of gas drives chemical reactions.

The aim of this work was to study the liquid flow field close to the free air-water surface. A stereo particle tracking velocimetry algorithm was applied and improved. It allows to study the liquid flow field in three-dimensional space. This technique is a major improvement to the well established two-dimensional particle tracking velocimetry by which a two-dimensional flow field is obtained. Since the liquid flow is a three-dimensional phenomenon it is important to study the complete flow field by a stereoscopic method. The particle tracking velocimetry method allows to study the Lagrange-velocity flow field and is therefore especially well suited to study the transport of near surface water elements to the deeper water. New techniques for the visualization of the liquid flow where introduced.

The theoretical background of liquid flow field, gas exchange processes and numerical methods are given in chapter 2. In chapter 3 frequently applied flow visualization methods are introduced and the associated techniques for the flow field evaluation are explained. The stereoscopic geometry and the modeling of the used system are shown in chapter 4. The image sequence processing techniques are explained in chapter 5 and the results are presented and discussed in chapter 6. Finally future steps and tasks for image sequence processing and for improving the experimental setup are proposed in the 'outlook' chapter 7.

Chapter 2

Theoretical aspects of liquid flow and gas exchange

2.1 Description of a liquid flow field

The motion of fluids can be described in one of two ways. The way of description implies directly the experimental techniques to be used (section 3.2).

The first way, the Euler-description of motion, regards the physical quantities such as the velocity $\vec{u}$, pressure p and density ρ as functions of position $\vec{x}$ and time t. Thus

$$\vec{u} = \vec{u}(\vec{x}, t) \tag{2.1}$$

(same for p and ρ) represents the velocity at prescribed points in space-time. The derivatives with respect to $\vec{x}$ and t represent the gradient field at a given time and a given position.

Alternatively, the fluid motion can be described in the Lagrange way. Fluid elements are identified at some initial time t_o with position $\vec{x_o}$. Thus $\vec{x} = \vec{x}(\vec{x}_o, t - t_o)$ where $\vec{x}(\vec{x}_o, 0) = \vec{x}_o$. The velocity of a fluid element is therefore the time derivative of its position:

$$\vec{u}(\vec{x}_o, t - t_o) = \frac{\partial}{\partial t}\vec{x}(\vec{x}_o, t - t_o) \tag{2.2}$$

The total time derivative is written in Euler-terms as

$$\frac{d}{dt} = \frac{\partial}{\partial t} + (\vec{u} \cdot \nabla) \tag{2.3}$$

which is the sum of the rate of change at a fixed point and a convective rate of change.

Many instruments measure fluid properties at a fixed point and provide Euler-flow field information directly. Questions concerning diffusion and mass transport deal with the motion of fluid elements and thus the Lagrange specification of the problem is better suited to treat them. The Lagrange description implies a marking of fluid elements by a dye or other tracers.

The equations of motion are governed by the conservation laws of mass and momentum:

The momentum transport is expressed by the *Navier-Stokes* equation:

$$\frac{\partial \overrightarrow{u}}{\partial t} + (\overrightarrow{u} \cdot \nabla) \overrightarrow{u} - \nu \Delta \overrightarrow{u} + \nabla p = \overrightarrow{f} \tag{2.4}$$

where $\overrightarrow{f}$ is the resultant of all forces acting on the fluid (such as the gravitational force $\overrightarrow{g}$) and ν the viscosity of the fluid.

The conservation of mass (*continuity equation*) is expressed as

$$\frac{\partial \rho}{\partial t} + \nabla \cdot (\rho \overrightarrow{u}) = 0 \tag{2.5}$$

and if the density of a fluid element does not change it takes the form

$$\nabla \cdot \overrightarrow{u} \quad = \quad 0 \tag{2.6}$$

For an unsteady, diffusive mass transport *Fick's 2nd law* applies:

$$\frac{\partial c}{\partial t} + \overrightarrow{u} \cdot \nabla c = D \Delta c \tag{2.7}$$

where c is the gas concentration and D the diffusion coefficient.

The flux density is related to the concentration gradient and defined as $\overrightarrow{j} = -D \nabla c$.

The water (in oceanic and laboratory circumstances considered in this work) can be regarded as an isotropic, incompressible *Newtonian fluid*[1].

2.2 Gas transfer processes

As the transport of atmospheric gases (inert and sparingly soluble) is the physical background of this work, a short overview of models describing basic processes is given.

---

[1] $p_{ij} = -p \delta_{ij} + 2 \nu e_{ij}$, with strain tensor $e_{ij} = \frac{1}{2} \left(\frac{\partial u_i}{\partial x_j} + \frac{\partial u_j}{\partial x_i} \right)$

The transport of inert or sparingly soluble gases between air and water is controlled by molecular transport (diffusion) and by turbulent transport processes. Directly at the water surface molecular diffusion is the process controlling the gas transfer. Turbulent transport vanishes at the water surface[2].

Molecular diffusion is caused by differences in the gas concentration. This is described by Fick´s 1st and 2nd law.

Fick´s 1st law is written as

$$\vec{j} = -D\nabla c \tag{2.8}$$

and describes the proportionality of the flux density $\vec{j}$ to the concentration gradient of the gas ∇c where D is the proportionality constant.

Fick´s 2nd law is written as

$$\frac{dc}{dt} = \frac{\partial c}{\partial t} + \vec{u} \cdot \nabla c = -\nabla j = D\Delta c \tag{2.9}$$

and describes the diffusive transport of mass (generally of scalar tracers). The transport is included in the term $\vec{u} \cdot \nabla c$.

The amount of gas transported through the water surface per time is quantified by the gas transfer velocity

$$\vec{k} = \frac{\vec{j}}{\Delta c} \tag{2.10}$$

and $\Delta c = c_{surface} - c_{bulk}$ is the gas concentration difference between the water surface and the water bulk[3].

The velocity $\vec{u}$ is determined by the Navier-Stokes equation

$$\frac{\partial \vec{u}}{\partial t} + (\vec{u} \cdot \nabla)\vec{u} = \nu\Delta\vec{u} + \frac{1}{\rho}\vec{f} - \frac{1}{\rho}\nabla p \tag{2.11}$$

where $\vec{f}$ is the sum of outer forces, ∇p the pressure gradient and ρ the fluid density. $\vec{u} \cdot \nabla u$ is the convective term and $\nu\Delta u$ the viscous term where ν is the kinematic viscosity.
In order to understand the physical properties of the flow better, frequently a perturbation approach (see Monin and Yaglom [1975]) is used to deal with the equations (2.9) and (2.11). The perturbation is in $\vec{u}$ and c, expressed by $\vec{u} = \overline{\vec{u}} + \vec{u}'$ and $c = \overline{c} + c'$ (barred characters mean average over time, primed characters the fluctuating part).

---

[2]The derivative of a 'mass element' at the water surface $z = 0$ in time is $\frac{\partial \eta}{\partial t}|_{z=0} = 0$.

[3]'water bulk': below a reference depth the mixing of concentration is large and no concentration gradient is present.

Substituting this into equation (2.9) and taking the temporal average $< \cdot >$ yields

$$\frac{\partial \overline{c}}{\partial t} + \overline{\overrightarrow{u}} \nabla \overline{c} = -\nabla \underbrace{(< c' \overrightarrow{u}' > -D\nabla \overline{c})}_{\overrightarrow{j}} \tag{2.12}$$

(where the identity $\overrightarrow{u} \cdot \nabla c = \nabla \cdot (\overrightarrow{u} c) - c \cdot \nabla \cdot \overrightarrow{u}$ was applied). $\overrightarrow{j}$ is the flux density which is the sum of the average molecular diffusion and the turbulent fluxes.

Applying the same substitution to equation (2.11) and considering the case of $\overrightarrow{u}$ in x-direction and depending only on z yields

$$\frac{\partial \overline{u}}{\partial t} = -\nabla \underbrace{(< u'w' > -\nu \nabla \overline{u})}_{=: j_m/\rho} \tag{2.13}$$

where $\overrightarrow{u} = \begin{pmatrix} u + u' \\ v' \\ w' \end{pmatrix}$.

The first term is called *Reynolds stress* (in three dimensions this term $t_{ij} = u'_i u'_j$ is a symmetric second-order tensor for $u_{i,j} = \{u', v', w'\}$). It describes the turbulent transport and the second term describes the viscous transport. For the stationary case $\frac{\partial \overline{u}}{\partial t} = 0$, j_m is a flux density of momentum - similar to equation (2.12). At the water surface the momentum flux density is equivalent to the shear force τ, $j_m|_{z=0} =: \tau$. This leads to the definition of a measure of the surface friction that has the dimension of a velocity, the *friction velocity* $u_*^2 := \frac{\tau}{\rho}$. If the viscous term is zero, the friction velocity becomes $u_*^2 = < u'w' >$ which expresses the correlation of turbulent transport with the fluctuating velocity components (here in x- and z-direction). If laminar flow is considered and the turbulent term is zero, the shear stress tensor becomes $\tau = \nu \rho \nabla \overline{u}$. This can for example be caused by wind stress on the water surface.

The terms *viscous boundary layer* and *aqueous mass boundary layer* are introduced to quantify the momentum transport and the molecular transport, respectively. For the definition of the aqueous mass boundary layer thickness z_* the equations (2.8) and (2.10) are taken and with $j = -D\frac{\partial c}{\partial z}|_{z=0}$ at the water surface[4] $z = 0$ (assuming the concentration is a function of the depth z, $c = c(z)$) it follows:

$$z_* = \frac{\Delta c}{-\frac{\partial c}{\partial z}|_{z=0}} = \frac{D\Delta c}{j} = \frac{D}{k}$$

where Δc is the concentration difference between the surface and the water bulk.

For the viscous boundary layer it follow from $\tau = \nu \rho \frac{\partial u}{\partial z}|_{z=0}$

---

[4]At the water surface the turbulent transport is absent.
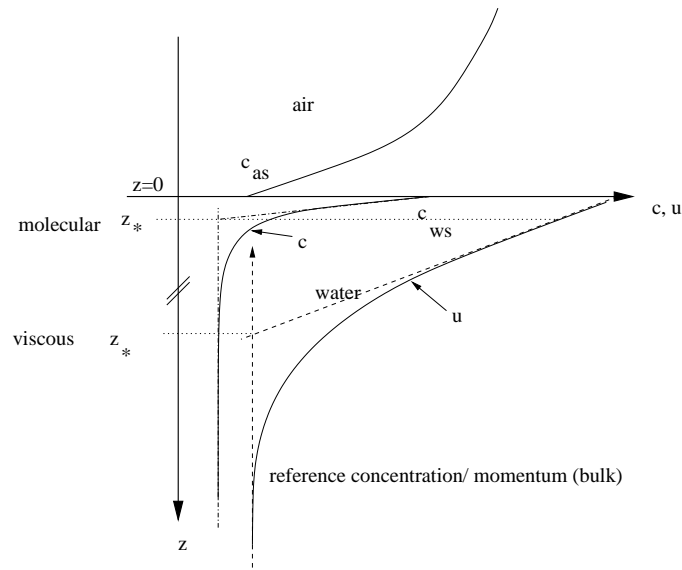
Figure 2.1: Schematic graph of the molecular and the viscous *boundary layers* on both sides of a gas-liquid interface. Due to the larger solubility α of the tracer gas in water as compared to air, the tracer gas concentration is discontinuous at the interface ($c_{ws} = \alpha \cdot c_{as}$).

$$\text{viscous}\, z_* = \frac{\Delta u}{\rho \frac{\partial u}{\partial z}|_{z=0}} = \frac{\Delta u}{\tau/\nu} = \frac{\nu}{k}$$

where Δu is the velocity difference between the water surface and the velocity in a reference depth.

The boundary layers are shown schematically in figure 2.1. The boundary layer of molecular diffusion (for dissolved inert gases in water) is in the order of 100 to $300\,\mu m$. The range of the viscous boundary layer is larger by a factor of 100 to 2000. The Schmidt number *Sc* represents this relation of the boundary layer thicknesses:

$$Sc = \frac{\nu}{D}$$

The turbulent transport terms of equations (2.12) and (2.13) can be replaced by functions which depend on the depth z and the turbulent diffusion coefficients $K_c(z)\frac{\partial \overline{c}}{\partial z}$ and $K_m(z)\frac{\partial \overline{u}}{\partial z}$. The equations can be integrated to obtain the concentration and velocity profiles:

$$\overline{c}(z) - \overline{c}(0) = \int_0^z \frac{j}{D + K_c(z')}dz' \, , \quad \overline{u}(z) - \overline{u}(0) = \int_0^z \frac{j_m/\rho}{\nu + K_m(z')}dz' \, .$$

Depending on the choice of the coefficients $K_c(z)$ and $K_m(z)$ different models are obtained such as the *small eddy model* and the *surface renewal model*. They are discussed in the next sections. The models have to deal with the turbulent transport mechanism and the gas diffusion. The simplest model (*film model*) assumes a stagnant film as a surface layer of thickness z_* where molecular diffusion appears and turbulent transport sets in below this layer. The diffusion of gas through this layer implies a proportionality of the diffusivity D and the gas transfer velocity $k = D/z_*$. The assumption of a linear concentration profile in the film layer is not very realistic and experimental observations contradicted $k \sim D$ (a $k \sim D^n$ with $n < 1$ was observed).

Small eddy model

This model describes the turbulent flux through the boundary layer as a cascade of growing eddies. The turbulent diffusion coefficient $K_c(z) = D - \frac{j}{\frac{\partial \overline{c}}{\partial z}}$ is determined by a Taylor series expansion applied to the concentration $\overline{c}(z)$ where the concentration and velocity fluctuations c', w' are assumed to be small compared to its mean components. According to Coantic [1986] boundary conditions for a rigid and a free interface[5] are applied and the concentration profile $c(z)$ is derived. It shows a lower concentration and a larger decrease in the case of a mobile interface as compared to the rigid interface.

For the gas transfer velocity k the Schmidt number dependency is found as

$$k \sim Sc^n u_*$$

(for $Sc > 100$) with exponent $n = 2/3$ for the rigid wall and $n = 1/2$ for the free interface.

Surface renewal model

The turbulent transport is based on a statistical renewal rate of the surface layer $\lambda = \gamma z^p$ depending on the depth z. For the classical surface renewal model (Danckwerts [1951]) the exponent p is zero, and for $p > 0$ the renewal rate becomes zero at the water surface and is more realistic (Jähne [1985]). The gas is transported through the aqueous boundary layer by diffusion and parts of this surface are exchanged with the water bulk in a statistical rate λ. Equation (2.12) becomes

$$\frac{\partial \overline{c}}{\partial t} = D\frac{\partial^2 \overline{c}}{\partial z^2} - \underbrace{\gamma z^p \overline{c}}_{= \frac{\partial}{\partial z} <c'w'>}$$

---

[5]rigid interface: $u'(z=0) = 0$ and same for v', w'; $\nabla \cdot \overline{u}' = 0 \rightarrow \frac{\partial w'}{\partial z} = 0$, $c'(z)|_{z=0} = 0$
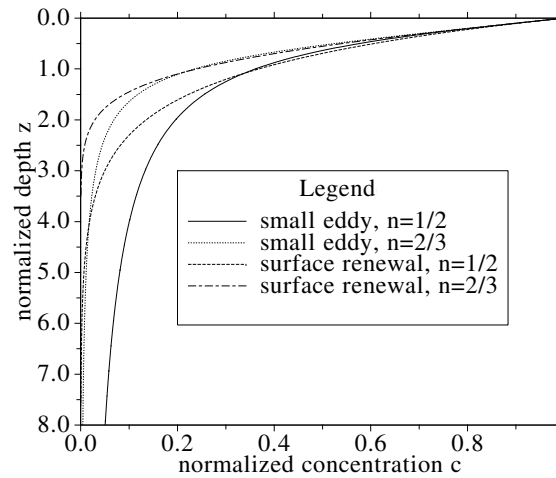free interface: $w'(z)|_{z=0} = 0$, $c'(z)|_{z=0} = 0$

Figure 2.2: The normalized gas concentration profiles for small eddy and surface renewal model with Schmidt number exponent 1/2 (free boundary, 'wavy surface') and 3/2 (rigid boundary, 'flat surface').

Applying the boundary conditions[6] for j yields the mean concentration profile $\bar{c}(z)$, which is an exponential function for $p = 0$ and an Airy function for $p = 1$. The mean concentration profile shows a larger decrease with depth than the small eddy model which expresses the larger scale turbulence postulated by the surface renewal rate. The concentration profiles for the surface renewal and the small eddy model are shown in figure 2.2.

The gas transfer velocity k can be predicted (Csanady [1990]) and is found as $k \sim Sc^n u_*$, where $n = 1/2$ for $p = 0$ and $n = 2/3$ for $p = 1$ interpreted as free and rigid interface respectively.

Influence of wind driven water waves on the gas transfer

If the wind speed over the water surface is increased, surface waves (capillary waves) appear. The gas transfer velocity k changes significantly with the appearance of surface waves. This is illustrated in figure 2.3 where k (for CO_2) is increased with the appearance of waves as compared to a smooth water surface. The transfer velocity k for CO_2 - which is controlled by the water side - is plotted versus the transfer velocity for water vapor k_{H_2O} - which is controlled by the air side.

---

[6]All the fluxes through the surface at z=0 and no flux in the bulk $z \to \infty$:

$$j(z=0) = D\frac{\partial \bar{c}}{\partial z}|_{z=0} = j_o$$
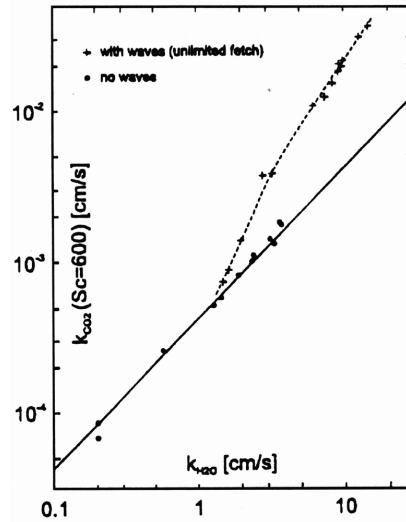$$\lim_{z\to\infty} j(z) = 0$$

Figure 2.3: Transfer velocity of CO_2 plotted against the transfer velocity of water vapor (measured in a circular wind-wave facility, Bösinger [1986], Huber [1984], Jähne [1980]). Smooth water surface conditions are marked by circles, wavy conditions by stars. The solid line is the prediction of a smooth rigid wall.

The effect of waves on the turbulent transport at the water side is stronger than on the turbulent transport at the air side and results therefore in an asymmetry seen in figure 2.3.

With the occurrence of waves the Schmidt number exponent n decreases (Bösinger [1986]). This indicates the enhanced gas transfer k by a factor of 3, but can not explain the increase of k by up to a factor of 5 from the predictions. This means, the turbulence level in the mass boundary layer is increased by a factor of 2. Pure surface increase can not explain this effect (Tschiersch and Jähne [1980]).

The wave generation begins at low wind speed (1-5m/s) with capillary waves (wave length in the range of cm). These capillary waves induce turbulent transport close to the water surface, which leads to the increased gas transfer velocity. Therefore this investigation is concerned with effects close to the free water surface in the range of cm. Capillary waves do also appear in connection with gravitational waves which dissipate energy from the gravitational waves (figure 2.4).

The energy flow of wind generated waves is displayed schematically in figure 2.5. The air flow over the water surface transfers energy and momentum to the water by the shear stress tensor (which includes pressure, viscous- and Reynolds-stress). The energy is either dissipated in near surface turbulence or to the same amount transfered to water (capillary and gravitational) waves. Due to non linear
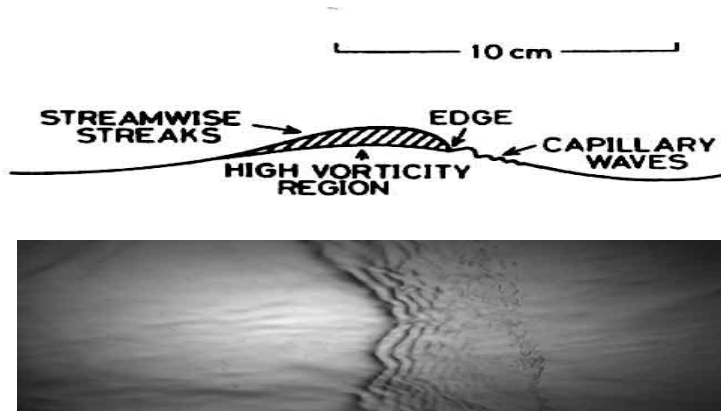
Figure 2.4: Gravitational wave and parasitic capillary waves (small 'ripples' on the leeward side of the gravitational wave). In the lower image is a view on the water surface where the steepness of the wave is represented by the grey-value, obtained by the imaging slope gauge (ISG, Balschbach [2000]) technique.

wave-wave interaction the capillary and gravitational waves are coupled. Energy of gravitational waves is transfered into capillary waves (*parasitic* capillary waves) and further transfered to turbulent flow, or directly to turbulent flow by wave breaking. The breaking of waves is another mechanism for turbulent flow generation.

2.3 Numerical solutions and models

The physical model describes the flow of an incompressible Newtonian fluid[7] in an area Ω and time T for a given boundary and initial conditions. The variables sought-after are the velocity $\overrightarrow{u}(\overrightarrow{x}, t)$ and the pressure $p(\overrightarrow{x}, t)$ which are functions of time t and the location in physical space $\overrightarrow{x} = (x_1, x_2, x_3)^T$. The system is described by the Navier-Stokes (momentum transport) equation and the incompressibility condition:

$$\frac{\partial \overrightarrow{u}}{\partial t} + (\overrightarrow{u} \cdot \nabla) \overrightarrow{u} - \nu \Delta \overrightarrow{u} + \nabla p = \overrightarrow{f}$$

$$\nabla \cdot \overrightarrow{u} = 0 \qquad \text{in } \Omega \times T$$

(2.14)

with outer forces f, the kinematic viscosity ν (ρ is included in p and f compared to (2.11)).

---

[7]Newtonian fluid: The shear stress tensor is defined as $T_{ij} = -p\delta_{ij} + \mu\left(\frac{\partial u_i}{\partial x_j} + \frac{\partial u_j}{\partial x_i}\right)$; in the one dimensional case the shear stress is $\tau = \mu\frac{du}{dy}$ (μ is the coefficient of viscosity, the dynamic viscosity $\nu = \mu/\rho$).
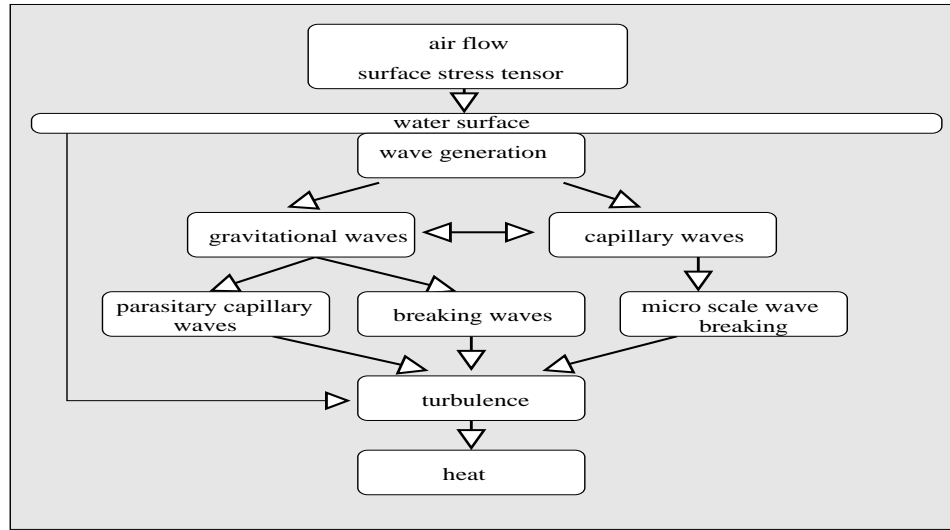
Figure 2.5: Scheme of interaction processes close to the water surface: The air flow over the water surface transfers momentum and energy via the surface stress into the water. The surface stress generates surface waves which induce gravitational and capillary waves (due to nonlinear interaction). Finally the energy is dissipated to turbulent flow (small scale velocity fluctuations) and into heat.

These equations describe many occurrences in nature such as flow of water or 'slow'[8] air flow, but also serves as a basic model for more complex systems such as combustion processes, chemical reactions, turbulence or multi-phase flow. The mathematical problem to be solved is a time dependent three dimensional nonlinear partial differential equation (PDE). Because of the nonlinearity of the problem direct solution methods can not be applied and iterative solution methods are required. The type of the problem can vary in time t and space Ω and this has to be taken into account for the method of solution. If the term $(\vec{u} \cdot \nabla)\vec{u} \gg -\nu\Delta\vec{u}$ (equivalent to $Re \gg 1$), the type of PDE has a hyperbolic character, for $-\nu\Delta\vec{u} \gg (\vec{u} \cdot \nabla)\vec{u}$ (equivalent to $Re \simeq 1$) the PDE has an elliptic character[9]. The local character of most of these problems demands also a local refinement in time and space or other techniques which take local properties into account such as multigrid methods. Without local refinement the capacity of computer memory would by far exceed the availability (a box of a resolution of 100x100x100 points would require 1GByte RAM, if a typical size of 1 KByte storage per point is assumed).

---

[8] otherwise the incompressibility condition is not given.

[9] Second order PDE: $Au_{xx} + 2Bu_{xy} + Cu_{yy} + Du_x + Eu_y + F = 0$

Let $Z = \begin{pmatrix} A & B \\ B & C \end{pmatrix}$

Elliptical PDE: Z positive definite ($det(Z) > 0$) (i.e. Poisson equation, Laplace equation)
Parabolic PDE: $det(Z) = 0$ (i.e. heat conductivity equation, diffusion equation)
Hyperbolic PDE: $det(Z) < 0$ (i.e. wave equation).

For the Navier-Stokes equation the elliptic type is of interest and considered here. This leads to the linear differential operator of second order L in the region Ω limited by the border $\Gamma = \partial\Omega$, where $Lu = f$ in Ω for a given f. The elliptic boundary value problem is characterized by the following boundary conditions[10]:

• Dirichlet boundary condition (for 'solid walls'):

$$u = \text{const on } \Gamma \tag{2.15}$$

• Neumann boundary condition (for 'free surface'):

$$\frac{\partial u}{\partial n} = n \cdot \nabla u = \text{const on } \Gamma \tag{2.16}$$

If gas transport is considered, the first Fick´s law (equation (2.7)) applies

$$\frac{\partial c}{\partial t} + \vec{u} \cdot \nabla c = D\Delta c$$

with concentration c and diffusion constant D. The equation can be solved easily, if the velocity was determined by the Navier-Stokes equation.

Sample model

The model for a channel flow is shown in figure 2.6. At the bottom and side Γ_b there are solid walls and the Dirichlet boundary condition (equation 2.15) for the velocity is $u = 0$. For the surface Γ_b the free surface boundary conditions are valid (equation 2.16)[11]. The in- and outflow conditions are cyclic $u_l(z,t)|_{\Gamma_l} = u_r(z,t)|_{\Gamma_r}$ on Γ_l, Γ_r and the Neumann boundary conditions are applied.

---

[10]There is also a 'mixed' boundary condition, the Robin boundary condition $\frac{\partial u}{\partial n} + \sigma u = const$ on $\Gamma (\sigma \neq 0)$.

[11]If the pressure and surface tension γ and the associated surface curvature R^{-1} are considered, the dynamical boundary condition is also valid:

$$t^{(i)} T(u,p) n = 0 \qquad i = 1,2$$
$$n T(u,p) n = -p_a + gh + 2\gamma R^{-1}$$

$T(u,p)$: surface stress tensor
$t^{(i)}, n$: tangent, normal to Γ_b
p_a: outer pressure
γ: surface tension
R^{-1}: average curvature of the free surface
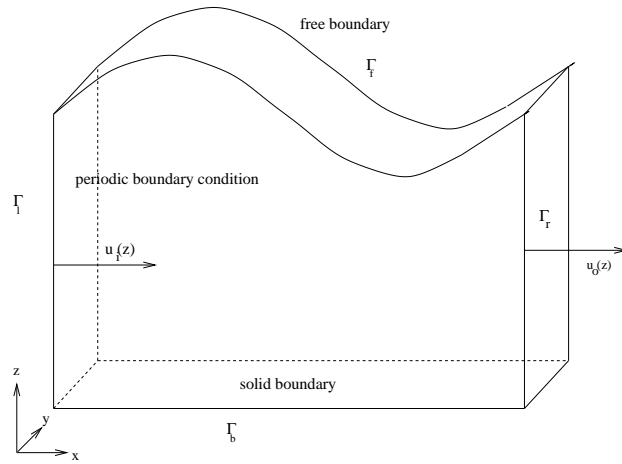g,h: gravitation, height of the water surface

Figure 2.6: Model for channel flow showing the boundary conditions.

Methods for solving partial differential equations

There are quite a number of methods to solve partial differential equations analytically (for example: characteristic methods, variable separation, Bäcklund transform, Green´s method, Lax Pair). In many cases, however the problem can not be solved analytically. Frequently there is not even a prove for the existence of a solution. Numerical solution methods are therefore required such as finite difference methods, finite volume methods, finite element methods or spectral element methods.

As far as flow dynamics is concerned, in many cases a direct simulation of the flow variables velocity $\vec{u}$ and pressure p is not workable. In viscous flow the movement in the fluid is conform, which means the viscous shear forces (section 2.1) are large enough to maintain a uniform movement. This leads to so called turbulence models where a large difference in the length scale exists. The relation between the largest to the smallest length scale is at least in the order of 10^3. This model class implies a strong simplification of the models by empirical parameters in a limited class of geometries and boundary conditions. Such an approach was already discussed in section 2.2 where the perturbation in velocity $\vec{u}'$ and pressure p' from their mean values $\overline{\vec{u}}$ and $\overline{p}$ was applied;

$$\vec{u} = \overline{\vec{u}} + \vec{u}'$$
$$p = \overline{p} + p'$$

This leads to the Navier-Stokes and continuity equation averaged in time:

$$\rightarrow \quad \frac{\partial \overline{\vec{u}}}{\partial t} + \vec{u} \cdot \nabla \vec{u} = -\nabla p + \nabla \cdot (\nu \nabla \vec{u} - \tau) + f$$
$$\nabla \cdot \overline{\vec{u}} = 0$$

with the Reynolds stress tensor τ. The modeling of the tensor $\tau = \tau(\overrightarrow{u}, p)$ leads to a number of different attempts for solutions. Some are listed in the following:

- Boussinesq hypothesis (1887):
  τ is modeled like the stress tensor of viscous forces acting on Newtonian liquids. The parameters are the velocity u and the length parameter l, which is assumed to be constant (the numerical solutions does therefore not differ from laminar flow).

- Mixing length theory:
  The assumption is that the fluid flow dominates in one direction $u = l \left| \frac{\partial u}{x} \right|$. The turbulent viscosity coefficient and the turbulent energy and the mixing length l (free parameter) are connected.

- Energy-equation model (k-model):
  The scale of fluctuating and mean velocity gradients is determined from the Navier-Stokes equation (one equation model), which includes two empirical constants (k: kinetic energy of turbulent motion and the length parameter l, the same as in the mixing length theory).

- Energy-dissipation model (k-ε model):
  l and k are obtained from the transport equations (two equation model) and it follows for the energy-dissipation $\varepsilon = \varepsilon(k, l) = k^{3/2}/l$. This is one of the most frequently used models. It implies four free parameters, and boundary and initial conditions for k and ε are required.

Finite element method and Navier-Stokes equation

The finite element method (FEM) allows to solve the Navier-Stokes equation directly (without modeling assumptions as the Reynolds stress tensor τ mentioned previously) and offers efficient numerical solution methods. The efficiency concerns numerical stability, convergence rate and flexibility for various posed limiting conditions. Therefore the FEM is the most widespread technique applied nowadays in computational fluid dynamics.

The equations (2.14) are split into different parts for solving the problem: The Poisson equation ($-\varepsilon \Delta u = f$), the convection-diffusion equation[12] ($-\varepsilon \Delta u + \widetilde{u} \nabla u = f$, $\widetilde{u}$ is constant and an approximation of u) and the Ossen equation ($-\varepsilon \Delta u + \widetilde{u} \nabla u + \nabla p = f$, which is the Stokes equation if $\widetilde{u} \nabla u$ is neglected). The equations have to be discretized and an appropriate numerical solver has to be applied.

First the time derivative operator in the Navier-Stokes equation is applied Müller et al. [1994]:

$$\frac{u - u(t_n)}{k} + \Theta(-\nu \Delta u + (u \cdot \nabla)u) + \nabla p = g(t_n, t_{n+1}), \ \nabla \cdot u = 0 \ \text{in} \ \Omega$$

---

[12]linearized Burgers equation

where $k = t_{n+1} - t_n$ is the time step, $g(t_n, t_{n+1})$ is the right hand side[13] and Θ characterizes the time stepping scheme. In each time step the following problem has to be solved for $u = u(t_{n+1})$ and $p = p(t_{n+1})$

$$\underbrace{[I + \Theta k(-\nu\Delta + (u \cdot \nabla))]}_{S} u + k\nabla p = G, \ \nabla \cdot u = 0$$

$\Leftrightarrow$

$$Su + kBp = G, \ B^T u = 0 \tag{2.17}$$

where B is the gradient matrix and S the velocity matrix. $u(t_n)$, the parameters $k = k(t_{n+1})$, $\Theta = \Theta(t_{n+1})$ and the right hand side[14] are given. This is the incompressible Navier-Stokes equation reduced to a discrete nonlinear saddle point problem.

The spatial discretization is the next step to be applied on equation (2.17) using the finite element method (see chapter D) and Galerkin discretization. Frequently used FEM Ansatz functions for the Stokes elements (equation (2.17)) are approximated by quadrilateral elements on Ω: a) linear in velocity and pressure approximations at the vertices ($Q1/Q1$), b) velocity at the vertices and constant pressure in the cell ($Q1/Q0$) and c) non-conforming elements[15] ($\widetilde{Q}1, Q0$) quasi-linear velocity at the vertices and constant pressure in the cell. The elements ($\widetilde{Q}1, Q0$) have advantages as compared to the ($Q1, Q1$) and ($Q1, Q0$) because no additional stabilization (of pressure) is needed (see Rannacher and Turek [1992]). The problem to be solved for each element is the matrix equation (2.17)

$$\begin{bmatrix} S & 0 & 0 & B_1 \\ 0 & S & 0 & B_2 \\ 0 & 0 & S & B_3 \\ B_1^T & B_2^T & B_3^T & 0 \end{bmatrix} \begin{bmatrix} u_1 \\ u_2 \\ u_3 \\ p \end{bmatrix} = \begin{bmatrix} G_1 \\ G_2 \\ G_3 \\ G_4 \end{bmatrix}.$$

The treatment of this problem is shortly sketched:

The Navier-Stokes solver can be split into its tasks (Turek [1999]): In the *outer control part* which is responsible for the global convergence rate and accuracy of the overall problem and in the *inner part of the solver* which provides approximate solutions within a given discrete framework.

There are two ways to split the problem into parts.

---

[13] $g(t_n, t_{n+1}) := \Theta f(t_{n+1}) + (1-\Theta) f(t_n) - (1-\Theta)(-\nu\Delta u(t_n) + (u(t_n) \cdot \nabla) u(t_n))$

[14] I: unit matrix, right hand side $G = [I - \Theta_1 k(-\nu\Delta + (u(t_n) \cdot \nabla)) u(t_n)] + \Theta_2 k f(t_{n+1}) + \Theta_3 k f(t_n)$ with parameters $\Theta_i = \Theta_i(t_{n+1}), i = 1, 2, 3$

[15] 'non conforming' means: 1) boundary conditions are only approximated or 2) $V_h \subset V$ or 3) the bi-linear and linear forms are only approximated numerically.

1. Linearize first the outer iteration problem (*adaptive fixed point defect correction* - or *quasi Newton* method and extrapolation of time), then solve the linear, indefinite problem in a inner iteration procedure (applying for instance the *coupled multigrid techniques*)

2. Solve first in the outer iteration the definite problem in u (Burgers equation) and p (linear pressure-Poisson equation), then solve the nonlinear subproblems in u (applying nonlinear iteration or linearization techniques).

Most Navier-Stokes solver are constructed from this scheme where details of implementation are of course various. However, the effective implementation is difficult in general situations. Modern solvers are based on multigrid and adaptive grid techniques and provide good convergence rates and high stability even for complex geometries of the posed problem.

Even if computing power improves quickly, computational fluid dynamics is still one of the big challenges and far from being applied in most 'real world' situations. Currently the available software has no proven control mechanism to determine deviations of the calculated result from the (unknown) exact solution. Beside this are many problems concerning numerical simulations. The large amount of required memory is one problem if three dimensional problems are considered. Local variation of the problems character result in difficulties in respect to stabilization (of convective terms) and require tricky methods of adaptivity in time and space. Boundary layers and complex geometries demand local mesh refinement methods.

Even 'simple' posed benchmark problems such as benchmark simulations of laminar (three-dimensional) flow around a cylinder (Schäfer and Turek [1996]) in a channel with solid walls pose the difficulties in obtaining quantitative results (even for low Reynolds numbers in the order of 10^2 to 10^3). A free boundary problem such as the model considered in this work is far more complicated. If a two-phase flow problem is considered with an air flow over a (wavy) water surface, the shear forces and pressure on the water surface can be determined rather easily. But calculations of the flow field close to the free water surface have not yet been carried out successfully. Even for low shear forces a high spatial resolution of the discretization mesh is required, particularly for high Reynolds numbers as considered here (in the order of 10^4 to 10^5). Due to the free surface condition (Neumann boundary) the surface location varies with each time step and requires a complete renewing of the mesh after a few time steps already. Computational efforts and memory requirements are therefore enormous and not even a qualitative solution is guaranteed. The main improvements needed are of algorithmic nature. It is of crucial importance to treat the local character of the problem. First steps in this direction are for instance the local refinement of meshes by using adaptive grid techniques and combined multigrid techniques (Becker and Braack [2000]). The improvements in computational power and computer memory will even in the far future

not solve these problems without essential improvements of numerical algorithms and methods.

Chapter 3

Flow visualization

3.1 Flow-field measurement techniques

In this section a number of frequently applied methods for liquid flow field measurements are mentioned. They differ in the way they can be applied and in the type of physical data they supply.

Classical *point measuring methods* provide information of the flow field at only a single point in the physical space, such as heat wire anemometry, Laser Doppler velocimetry and acoustic Doppler velocimetry (next sections 3.1.1, 3.1.2).

Most other methods use tracer material. The tracers can be either continuous or discrete providing information on the two- or three-dimensional flow fields.

A continuous tracer material (molecular tracer, fluoresceine) is applied in the Laser induced fluorescence method (Münsterer [1996]). This technique is also used in biological sciences (Uttenweiler and Fink [1999]) and in observing mixing (Koochesfahani and Dimotakis [1986]), (Koochesfahani and Dimotakis [1985]) and exchange processes (Eichkorn et al. [1999]). A frequently used continuous tracer for air flow field measurements is a dye aerosol injected into the air flow. The *Schlieren* method uses inherent properties of the liquid (or gas) such as the refraction number dependency on the density: the deflection of the optical ray results in an intensity modulation of the image. Flow field properties which are related to these inherent properties (i.e. heat, density and refraction number) can therefore be deduced (Oertel and Oertel [1989]).

The most frequently methods used for liquid flow field measurements use (macroscopic) seeding particles. These methods are divided into two branches (see also section 2.1) and determine the type of method for the flow visualization as discussed in section 3.2. One type of methods are region oriented such as *Laser speckle velocimetry (LSV)* or *particle imaging velocimetry (PIV)* and provide a velocity vector field (section 3.1.3). The other type of methods detects single (seed-

ing) particles and persecutes them in time (*particle tracking velocimetry* PTV, section 3.1.4).

3.1.1   Hot wire anemometry

A thin wire, surrounded by a liquid medium, is connected to a constant electrical voltage source and heated. The flow of the liquid around the wire determines the rate of the heat transport from the wire to the liquid. The temperature change of the wire causes a change in the electrical current through the wire. This current is a measure of the flow speed of the liquid (Klages [1977]).

The thinner the wire (some microns), the lower the heat capacity and the better the time constant of the temperature adaption. Due to this time constant, the sampling frequency is typically up to 50 kHz. If several wires are positioned crosswise, even two- and three-dimensional velocities can be determined (Tsinober et al. [1991]).

This is an invasive method and frequently used in commercially available devices. The precision is better than 1%.

3.1.2   Laser Doppler anemometry (LDA), acoustic Doppler velocimetry (ADV)

The LDA method is based on the Doppler effect of small particles (seeding particles or naturally found particles) in the liquid for two crossed Laser beams.

A Laser beam is divided into two single beams which are crossing each other at the volume of interest. In this volume (typically $0.15 \cdot 0.15 \cdot 2\,\mathrm{mm}^3$) an interference pattern of light and dark stripes occurs (Wiedmann [1984]). The particles crossing this volume change their scattering intensity in a certain frequency according to the distance of the stripes and to the velocity of the particles. A photo-detector records this changing intensity and the velocity is then readily calculated (by a signal processor). If more Laser-beam crossings are used (of different wave length[1]), the three-dimensional velocity can be determined with a precision of about 1% and the sampling rate can exceed 100 kHz.

The ADV method is very similar to LDA but uses an acoustic signal. For three dimensional measurements three acoustic generators are necessary. They are positioned in a plane with equal distance from each other generating an interference pattern. An acoustic sensor measures the intensity changes of moving particles due to the interference pattern.

Both methods, LDA and ADV, are invasive and are restricted to one single point.

---

[1]Such as Argon-Ion Laser lines with 514, 488 and 476 nm.

3.1.3 Particle imaging velocimetry (PIV)

This method yields dense velocity vector fields in Euler-coordinate representation (2.1). Either continuous or dense particles are required. The PIV method (for review see Grant [1997]) takes a spatial limited window of the image and cross-correlates this in time to the subsequent image. The result is a displacement vector, averaged over the correlation window. Moving the window over the whole image yields the velocity vector field. The correlation procedure with a window of a certain size is a low pass filtering procedure - depending on the size of the correlation window - and therefore information on small scale fluctuations are lost. Usually this method requires a high seeding particle density (several thousands per image) to gain a good spatial resolution - typically a correlation window should contain some tenths of particles. At the Heidelberg wind/wave facility PIV measurements were performed close to the aqueous boundary layer by Dieter et al. [1994].

3.1.4 Particle tracking velocimetry (PTV)

This method follows single (seeding) particles in time over a sequence of images. The result is therefore the Lagrange velocity field of the flow (2.2) which consist of particle trajectories (Hering [1996]). Most PTV techniques use streak photography as a tool for determination of the flow field (Hesselink [1988]). The velocity can be obtained by measuring the length, orientation and location of each streak (Gharib and Willert [1988]). Interpolating the velocity of the particles onto a regular grid allows to calculate the Euler-velocity field (equation (2.3)).

This method is quite critical concerning the density of particles (number of particles per volume/image). The higher the density and the higher the speed[2] of particles the more likely is the overlap of the streaks. Overlap of streaks means a loss of the particle tracking in the image sequence. Either the trajectory is interrupted or has to be reconstructed by some interpolation algorithms. The maximum number of particles per image is limited to about 1000-2000.

An important aspect is the type of velocity information to be extracted. There are basically two different approaches: The particle-imaging velocimetry (PIV) and the particle-tracking velocimetry (PTV) techniques. Continuous or discrete tracers can be applied for both of these techniques. The best spatial resolution is achieved by using discrete tracers.

The PIV and PTV techniques are distinct in respect to the observation of the velocity flow field (see section 2.1). The PIV technique yields a 'snapshot' of the flow field, which is $\vec{v}_i = \vec{v}(\vec{x}_o, t - t_o)|_{t=t_i}$, the *Euler*-representation of the velocity v_i at a certain time t_i for each spatial location $\vec{x}_o$.

In contrast to this, the PTV technique follows a 'mass point' - actually a particle - in time. It yields the *Lagrange*-representation of the velocity, which is

---

[2]The higher the speed, the longer the streak image of the particles.

$\overrightarrow{x} = \overrightarrow{x}(\overrightarrow{x}_o, t - t_o)$ where the particle was at position $\overrightarrow{x} = \overrightarrow{x}_o$ at the time $t = t_o$ and is moving in a trajectory to position $\overrightarrow{x}(t_i)$ at time t_i.

The Lagrange-representation allows also to calculate the Euler-flow field by simply differentiating $\dot{x}$ in time. The purpose of this work was to determine the Lagrange velocity field of seeding particles. Therefore the choice of the method was the PTV method. More details about the PTV techniques are found in section 5.2.

3.2   Techniques for flow field visualization

The flow field can be visualized by using either discrete tracers, such as seeding particles or bubbles, or by continuous tracers, such as fluorescent dyes using Laser induced fluorescence (Eichkorn et al. [1999]). The visualization techniques discussed here use tracer particles which are either mixed into the liquid before or locally added to the flow. Properties and characteristics of tracer particles such as seeding particles and hydrogen bubbles are discussed in section 3.2.1 and 3.2.2.

Depending on the physical properties of the liquid to be examined the type of tracer has to be chosen carefully. To investigate the velocity flow field of the liquid, discrete tracers are suitable. Either seeding particles (perspex, polycrystalline material) or hydrogen bubbles generated by electrolysis are chosen.

3.2.1   Seeding particles

There are several criteria which the seeding particles have to fulfill. The main criteria are: they should disturb the measurement respectively the liquid flow in a minimal way and they should be sufficiently visible for the observing device (CCD camera[3]).

The following points are important:

- The size/diameter d of the particle:
  The smaller, the less disturbing; but the visibility (refractivity/ reflectivity) is reduced (proportional to the area). Another important effect of the size is the ability of the particles to follow the flow field of the fluid. This can be deduced from the equation for the motion of small spherical particles, first introduced by *Basset, Boussinesq* and *Ossen* (Hinze [1959]). The analysis of this equation shows the ability of particles to follow a fluctuating flow field with frequency ω. The deviation is given by

$$\varepsilon(\omega) = \text{const.}\, \omega^2 d^4$$

  The choice of smaller particles reduces this deviation, but the *visibility* of the particles is proportional to d^2 and therefore larger particles are better visible.

---

[3]CCD stands for 'Charge Coupled Device'.

- The material properties:

  - the intensity of the scattered light, depending on the observation and illumination angle, where the intensity should be as large as possible (next section 3.2.1.1)

  - the density which should be rather close to the liquid density to allow for a minimum buoyancy

- The particle density (number of particles per volume) which is usually not critical because the average free length is much smaller.

3.2.1.1   Scattering properties

In this section the scattering cross section $\sigma(\Omega)$ and its dependency on the steradian Ω is briefly discussed.

The scattering cross section[4] is defined as

$$\sigma(\Omega) = \frac{dI(\Omega)}{d\Omega}$$

which is the scattered light intensity dI in the differential steradian $d\Omega$.

The seeding particles are large compared to the wavelength of the light source. Therefore the Mie scattering theory has to be applied.

The scattering is described by the Maxwell equations written in a symmetric form (Born and Wolf [1984]) using the vector potential[5] $\overrightarrow{\Pi}_e$ and $\overrightarrow{\Pi}_m$:

$$\overrightarrow{E} = \nabla \times \left(\nabla \times \overrightarrow{\Pi}_e \right) - ikc\overrightarrow{\Pi}_m$$

$$\overrightarrow{H} = \nabla \times \left(\nabla \times \overrightarrow{\Pi}_m + ikc\frac{n^2}{c^2}\overrightarrow{\Pi}_e \right) \tag{3.1}$$

where

n: refraction index

c : light speed

k : wave number

---

[4]more precisely: the differential scattering cross section

[5]The magnetic field potential expressed as $A = ikc\frac{n}{c^2}\overrightarrow{\Pi}_e + \nabla \times \overrightarrow{\Pi}_m$

and the electric field potential $\Phi = -\nabla \cdot \overrightarrow{\Pi}_e$

The particle shape (can be assumed as spherical) leads to spherical symmetry of the electromagnetic waves. Therefore the vector potentials can be written as the *Debey potential*

$$\overrightarrow{\Pi}_{e/m} = \Pi_{e/m} \cdot \overrightarrow{x} \tag{3.2}$$

where $\overrightarrow{x}$ is the radial direction of the wave extension.

The equations (3.1) can be solved through (3.2) written in spherical coordinates (r, φ, ϑ) with

$$\Pi_{e/m}(r, \varphi, \vartheta) = Y_l^m(\varphi, \vartheta) \cdot z_l(r) \tag{3.3}$$

where the equation contains an angular part with $Y_l^m(\varphi, \vartheta)$, the spherical surface function[6], and radial part with the spherical Bessel function $z_l(r)$. This spherical Bessel function $z_l(r)$ can be written with the Bessel function $Z_{l+\frac{1}{2}}(r)$ for uneven number $l + \frac{1}{2}$ as $z_l(r) = \sqrt{\frac{\pi}{2r}} Z_{l+\frac{1}{2}}(r)$. $Z_{l+\frac{1}{2}}(r)$ has to be chosen according to the initial conditions as the Bessel function of the first type $J_l(r)$, the Bessel function of the second type (*Weber function*) $W_l(r)$ or a linear combination of both $H_l(r)^{(1,2)} = J_l(r) \pm iW_l(r)$ (*Hankel function*).

The Debey potentials can then be written as

$$\Pi_{e/m}(r, \varphi, \vartheta) = e^{i\omega t} \sum_{l=1}^{\infty} (-i)^l \frac{2l+1}{l(l+1)} P_l^1(\cos \vartheta) j_l(kr) \begin{cases} \cos\varphi, \text{ for } e \\ \sin\varphi, \text{ for } m \end{cases}.$$

The solution of the incoming wave scattered on a sphere (particle) has to be divided up into the inside of the sphere (refraction index *n*) and the outside of the sphere. *Outside the sphere* the Ansatz function is:

$$\Pi_{e/m}(r, \varphi, \vartheta) = e^{i\omega t} \sum_{l=1}^{\infty} (-i)^l \frac{2l+1}{l(l+1)} P_l^1(\cos \vartheta) h_l^{(2)}(kr) \begin{cases} a_l \cdot \cos\varphi, \text{ for } e \\ b_l \cdot \sin\varphi, \text{ for } m \end{cases} \tag{3.4}$$

where the Hankel function related Ansatz function $h_l^{(2)}(kr)$ has to be chosen (because the Ansatz function has to be a spherical wave $\lim_{r\to\infty} h_l^{(2)} \sim \frac{i^{l+1}}{kr} e^{-ikr}$). The coefficients a_l, b_l, c_l, d_l are determined by the boundary conditions on the sphere (transition from vacuum to matter).

Inside the sphere the Ansatz function is:

---

[6]$Y_l^m(\varphi, \vartheta) = \sqrt{\frac{2l+1}{2\pi} \frac{(l-m)!}{(l+m)!}} P_l^m(\cos \vartheta) e^{im\varphi}$, where $P_l^m(x)$ is the Legendre function to the associated Legendre polynomial $P_l(x)$; $l \geq |m| \geq 0$.

$$\Pi_{e/m}(r,\varphi,\vartheta) = e^{i\omega t}\sum_{l=1}^{\infty}(-i)^l\frac{2l+1}{l(l+1)}P_l^1(\cos\vartheta)\,j_l(nkr)\begin{cases} n\cdot c_l\cos\varphi, & \text{for }e \\ n\cdot d_l\sin\varphi, & \text{for }m \end{cases} \quad (3.5)$$

where the Bessel function related to Ansatz function $j_l(nkr)$ has to be chosen (because $\lim_{r\to 0}W_l(r)\to\infty$ and $\lim_{r\to 0}H_l(r)\to\infty$).

The main interest is the intensity characteristics of the scattered light in a large distance (large compared to the sphere/particle size). Substituting $\lim_{r\to\infty}h_l^{(2)}\sim\frac{i^{l+1}}{kr}e^{-ikr}$ in equation (3.4) yields

$$\Pi_{e/m}(r,\varphi,\vartheta) = \frac{ie^{i\omega t}}{kr}\sum_{l=1}^{\infty}\frac{2l+1}{l(l+1)}P_l^1(\cos\vartheta)\begin{cases} a_l\cos\varphi, & \text{for }e \\ b_l\sin\varphi, & \text{for }m \end{cases}. \quad (3.6)$$

The electrical and magnetic fields can be expressed as

$$\overrightarrow{E}_\vartheta = c\overrightarrow{H}_\varphi = \frac{i}{kr}e^{-i(kr-\omega t)}\cos\varphi\,S_1(\vartheta) \quad (3.7)$$

and

$$-\overrightarrow{E}_\varphi = c\overrightarrow{H}_\vartheta = \frac{i}{kr}e^{-i(kr-\omega t)}\sin\varphi\,S_2(\vartheta) \quad (3.8)$$

which is a product of an outgoing spherical wave and the *form factors* $S_{1,2}(\vartheta)$:

$$S_1(\vartheta) = \sum_{l=1}^{\infty}\frac{2l+1}{l(l+1)}\left(a_l\frac{P_l^1(\cos\vartheta)}{\sin\vartheta}+b_l\frac{\partial P_l^1(\cos\vartheta)}{\partial\vartheta}\right) \quad (3.9)$$

$$S_2(\vartheta) = \sum_{l=1}^{\infty}\frac{2l+1}{l(l+1)}\left(a_l\frac{\partial P_l^1(\cos\vartheta)}{\partial\vartheta}+b_l\frac{P_l^1(\cos\vartheta)}{\sin\vartheta}\right) \quad (3.10)$$

Finally the intensity $I(\vartheta)=\left|\overrightarrow{E}\right|^2/2$ is

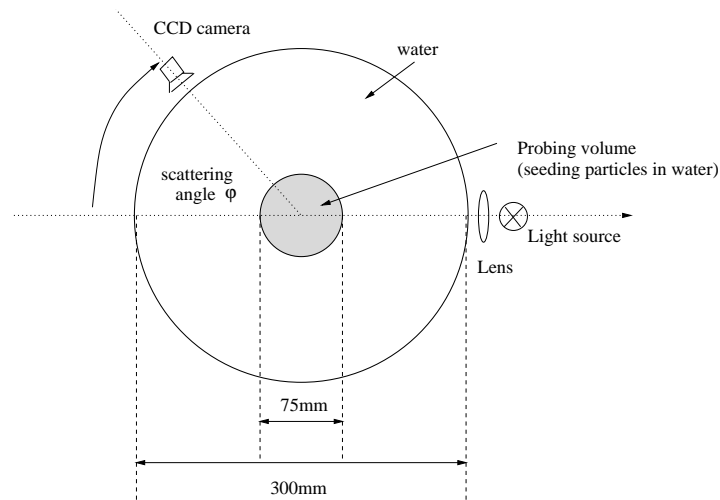$$I(\vartheta) = \frac{|S_1|^2+|S_1|^2}{2k^2r^2}I_o \quad (3.11)$$

Figure 3.1: Principle of the setup for measuring the scattering angle.

Comparison of Mie-scattering theory with experimental results

The scattering properties of some frequently used seeding particles such as poly-crystalline seeding particles (Optimage company), hollow glass spheres and per-spex seeding particles of $30\mu m$, $35\mu m$ and $180\mu m$ in diameter are shown in figure 3.2. The size (diameter) distribution of the particles is, due to production conditions, a normal distribution (20%-50% full width half length). The dependency of the scattered light intensity (expressed in mean grey-value) on the scattering angle is shown in figure 3.2 and was measured by Garbe [1998] and Hering et al. [1998]. A white light source (glow-discharge lamp, Cermax) was used and an angle of about 320° (excluding 40° of direct view into the light source) was covered. The intensity measurement was done by a CCD camera (50 images were averaged). The principle of the experimental setup is shown in figure 3.1. An inner cylinder contains water and the seeding particles. Close to the water-filled outer cylinder a CCD camera and a light source were mounted. The outer cylinder reduces the refraction effect due to a smaller curvature.

The results of the light intensity on the scattering angle show a good agreement to the calculated curve (solid lines in fig. 3.2) from the minimum angle (about $\pm 20°$) up to $\pm 80°$. Calculated values deviate by about $\pm 10\%$ for angles of $|\pm\varphi| \geq 80^o$.

The differences in scattering intensity of hollow glass spheres and the other seeding particles in between the range of $\pm(50°\text{-}80°)$ scattering angle are caused by the different refraction indices. The hollow glass spheres behave like air bubbles (glass volume is about 1/10 of the air volume).

The consequences for the measurements are:

- The scattering angle around 90° shows a plateau-like minimum in intensity.
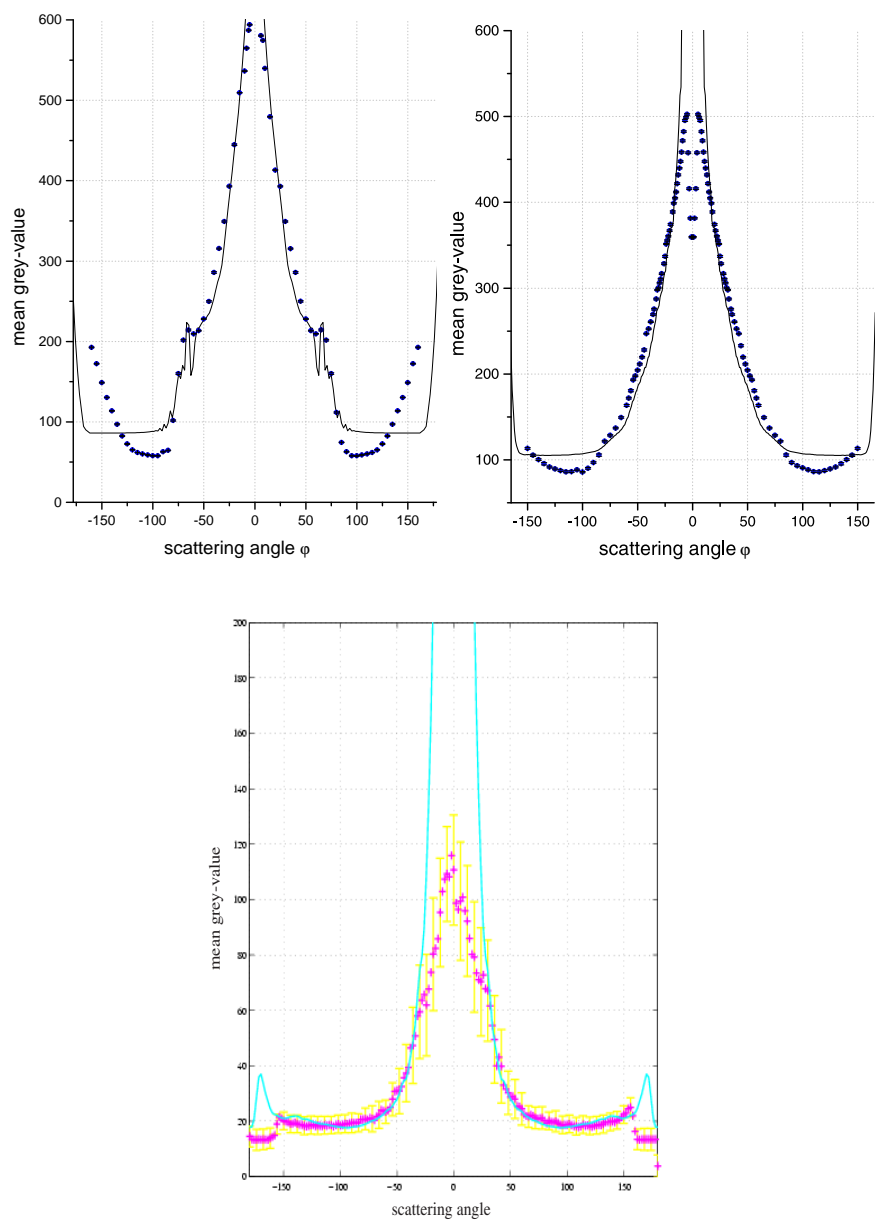
Figure 3.2: Scattered light intensity (expressed in mean grey-value) dependency on the scattering angle. Solid lines: calculated values according to the Mie-scattering theory averaged for wavelengths $\lambda = 400\ldots800nm$. Top left: Hollow glass spheres (diameter $d = 35\mu m$, refraction index $n = 1.0$); top right: polycrystalline seeding particles ($d = 30\mu m$, $n = 1.6$), (diploma thesis by Garbe [1998]); bottom: perspex seeding particles ($d = 180\mu m$, $n = 1.6$), (by Hering et al. [1998]).

Therefore the traditional illumination technique (section 3.3.1) where usually an angle of slightly less than 90° was used is not well suited.

- The intensity raises rapidly for scattering angles from 80° to the minimum angle. A better choice for particle tracking velocimetry (PTV) is therefore to take the angle close to forward scattering. A drawback is the large change of intensity with a small change in scattering angle which limits the usage of the continuity of optical flow as a correspondence correlation criterion for PTV[7].

3.2.1.2 Buoyancy

It is required that the particle velocity does not deviate significantly from the fluid velocity in order to avoid distortion of the fluid motion. This is the case for the particles used in this work.

Nevertheless the entrainment of the particles by the liquid, especially in the case of hydrogen bubbles, has to be taken into account. The movement of solid spheres can be calculated by the *Basset-Boussinesq-Ossen* equation which is in the one dimensional case described by:

$$m_p \frac{du_p}{dt} = \underbrace{G}_{g(m_p - m_F)} - \underbrace{W}_{3\pi d \mu_F (u_p - u_F)} + m_F \cdot \frac{du_F}{dt} + \chi m_F \frac{d(u_p - u_F)}{dt} -$$

$$\sqrt{\pi \rho_f \mu_F} \cdot \int_{t_o}^{t} \frac{d(u_p - u_F)/dt'}{\sqrt{t - t'}} dt' \tag{3.12}$$

where the meaning of the symbols is:

u_p:	velocity of the particle
$m_p = \rho_p \pi d^3/6$:	mass of the particle with density ρ_p
$m_F = \rho_F \pi d^3/6$:	superseded mass of the fluid with density ρ_F by the particle
g:	gravitational constant
u_F:	flow velocity
d:	diameter of the particle
μ_F:	the kinematic viscosity $\nu_F = \mu_F/\rho_F$
χ:	parameter which describes the dissipation of kinetic energy to the fluid

The meaning of the terms of equation (3.12) (balance equation for the forces acting on the particle) is the following:

---

[7]Especially if the light source is mounted above the water surface the refraction angle - and therefore the scattering angle - changes with the steepness of the waves. Small capillary waves show a large steepness and therefore the scattered light intensity fluctuates quite heavily.

The first term G is the sum of the external forces acting on the particle which is the difference of the weight of the masses m_p and m_F. The second term W is in this case the Stokes air resistance (for u_F constant). If u_F is not constant, then three further terms have to be added. The third term is the inertia of superseded mass of the fluid from particle. The fourth term takes the dissipation of kinetic energy toward the liquid into account with the factor χ for the partition of the superseded mass of the liquid by the particle. The last term is caused by the shear force of the particle from the beginning of the particle movement (where $u_p \neq u_F$) at time t_o to the present time t.

Equation (3.12) can be simplified. Assuming that the last term (the integral) is small compared to the other terms and setting $\chi = 1/2$ the dissipation of kinetic energy towards the liquid is taken into account with half of the mass from the superseded liquid. Defining $u' = u_p - u_F$ for equation (3.12) it follows

$$\frac{du'}{dt} + \frac{u'}{\tau} = \frac{\rho_p - \rho_F}{\rho_p + \rho_F/2}(g - \frac{du_F}{dt}) \qquad (3.13)$$

with the characteristic time

$$\tau = \frac{d^2(\rho_p + \rho_F/2)}{18\mu_F}. \qquad (3.14)$$

If the liquid medium is at rest ($u_F = 0$, $du_F/dt = 0$), equation (3.13) is written as

$$\frac{du_p}{dt} + \frac{u_p}{\tau} = \frac{\rho_p - \rho_F}{\rho_p + \rho_F/2}g \qquad (3.15)$$

Because $\lim_{t\to\infty}(\frac{du_p}{dt}) \longrightarrow 0$, the velocity u_p is constant in the limit of $t \to \infty$. The buoyancy velocity is therefore

$$u_{p\infty} = u_p(t \to \infty) = \frac{\rho_p - \rho_F}{\rho_p + \rho_F/2}g\tau$$

$\Leftrightarrow$

$$u_{p\infty} = \frac{d^2(\rho_p - \rho_F)}{18\mu_F}g \qquad (3.16)$$

where $u_{p\infty}$ is in the direction of the gravitational force g if $\rho_p > \rho_F$ and against g if $\rho_p < \rho_F$ such as for H_2 bubbles.

Taking $u_{p\infty}$ from equation (3.16) the equation (3.15) results in

$$\frac{d(u_{p\infty} - u_p)}{u_{p\infty} - u_p} = -\frac{dt}{\tau}. \qquad (3.17)$$
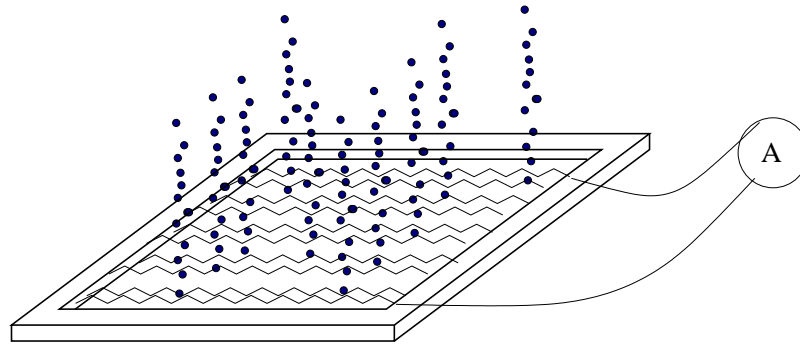
Figure 3.3: Hydrogen/oxygen generator: A wire frame with jagged platinum coated tungsten wire connected to a current source. The bubbles are generated at the inflection points.

If the initial condition is assumed as $u_p(t=0)=0$ the integration of equation (3.17) is

$$u_p = u_{p\infty}(1 - e^{-t/\tau}). \tag{3.18}$$

In the case of $\rho_p \ll \rho_F$ the buoyancy velocity is $u_{p\infty} = -d^2 \rho_F g/18\mu_F$ and the time constant $\tau = d^2 \rho_F/36\mu_F$ and therefore $u_{p\infty} = 2g\tau$ (if $\rho_p \gg \rho_F$ it follows $u_{p\infty} = g\tau$).

3.2.2 Hydrogen/oxygen bubbles

Compared to solid particles hydrogen and oxygen bubbles have the major advantage that they are easy to produce by electrolysis and that they do not pollute or disturb the environment. They can also be placed rather precisely into the measuring volume. A disadvantage of this method is the disturbance induced by the hydrogen/oxygen generating device.

The device to generate the bubbles (fig. 3.3) is mounted in some distance from the measuring volume. The distance has to be chosen appropriately depending on the velocity range of the along-wind (horizontal) velocity of the water in the measuring volume. De-ionized water is used and *KCl* is added (concentration $0.24 \cdot 10^{-6}$ M) in order to get a sufficiently high conductivity. The size of the hydrogen and oxygen bubbles is in the range of the wire[8] diameter. To produce bubbles more regularly in time the oxygen cathode has to be separated and current pulses have to be applied (up to 100 Hz). Oxygen is more irregularly produced as compared to hydrogen. The conditions prevailing in this work did not require to separate the oxygen from the hydrogen bubbles and the cathodes and anodes were placed just opposite to each other in the wire frame. If the medium of the fluid is water, and the electrolysis of water produces H_2 and O_2 (where $\rho_{H_2} \ll \rho_{H_2O}$ and $\rho_{O_2} \ll \rho_{H_2O}$ with $\rho_{H_2O} = 998.2\,kg/m^3$, $\rho_{H_2} = 8.379 \cdot 10^{-2} kg/m^3$ and $\rho_{O_2} = 1.341\,kg/m^3$), the
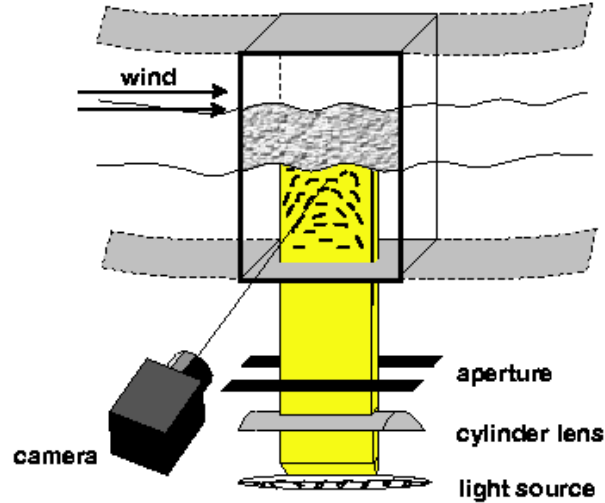
---

[8]platinum coated tungsten

Figure 3.4: Scheme of the experimental setup used for classical PTV. A light sheet is generated by a cylindrical lens (from Hering [1996]).

kinematic viscosity is $\mu_{H_2O} = 1.004 \cdot 10^{-3}\,kg/ms$, and from equation (3.16) the buoyancy (ascending) velocity is calculated as

$$u_{p\infty}(d = 30\mu m) = 0.49\,mm/s$$

for H_2 and O_2 bubbles of $30\mu m$ in diameter. The buoyancy velocity is almost immediately achieved with a time constant $\tau = 25\mu s$.

3.3 Experimental setup for particle tracking velocimetry

3.3.1 Traditional setup

The two dimensional - traditional - flow visualization uses a light sheet to cut out a small slice of a fluid volume. The light sheet can be generated for example by a Laser scanner or by an optical system (figure 3.4).

3.3.1.1 Observation close to the water surface

The main interest of this study is the influence of small scale waves, such as capillary waves, on the flow field. The typical wave length is in the order of *cm*. There-

fore the aim is to get as close as possible to the water surface and to obtain a high spatial resolution[9]. The experimental setup has to

- minimize disturbances due to light reflections at the water surface and

- optimize the scattering angle of the seeding particles (see section 3.2.1.1) with the angle of light source and the camera.

There are basically two ways for the camera and illumination to obtain the volume of observations close to the water surface. In the first method a camera is looking from the side (figure 3.4), inclined in a small angle away from the water surface, beneath the water surface. In the second method the camera looks from the bottom to the water surface (optical axis of the camera and lens system perpendicular to the water surface). Each method has its advantages and disadvantages:

An important advantage of the first method is the possibility to follow the water surface by a wave follower which shifts the observation area/volume according to a certain reference point at the water surface.

Wave follower

This method was established and applied for Laser induced fluorescence (LIF) measurements (Münsterer [1996]) but could also be applied for PTV measurements. The setup is shown in figure 3.5. The goal of the experiment was to visualize the two-dimensional concentration profile of gas in the aqueous boundary layer. In this experiment the water contained *fluoresceine* where the fluorescence intensity is related to the dissociated *HCl* concentration in the water bulk.

A Laser beam[10] and a scanner mirror generate a light sheet perpendicular to the water surface and excites the fluorescence of fluoresceine. This intensity profile is seen by a CCD camera where the imaging area was shifted by the wave follower scanning mirror. To avoid optical distortions caused by the scanning mirror a so called *f-theta lens system* was used instead of an achromatic lens. The scanning mirror was controlled by the line array camera attached to a micro controller (Sorcus Multilab 2) which is in turn connected to a host PC computer. The line array camera takes a profile image perpendicular to the water surface which images the height of the water surface. This system allows to follow waves of $5\,cm$ amplitude.

A major drawback of this technique for application in PTV is the measurement of the scanning mirror position; precise position measurement is required for PTV. Deviations in the determination of the mirror position increases the error of the particle and trajectory position in the image. Another drawback is the inertia of the

---

[9]A high spatial resolution means a small volume of observation for a given lens system and a given number of CCD-elements (CCD-sensor).

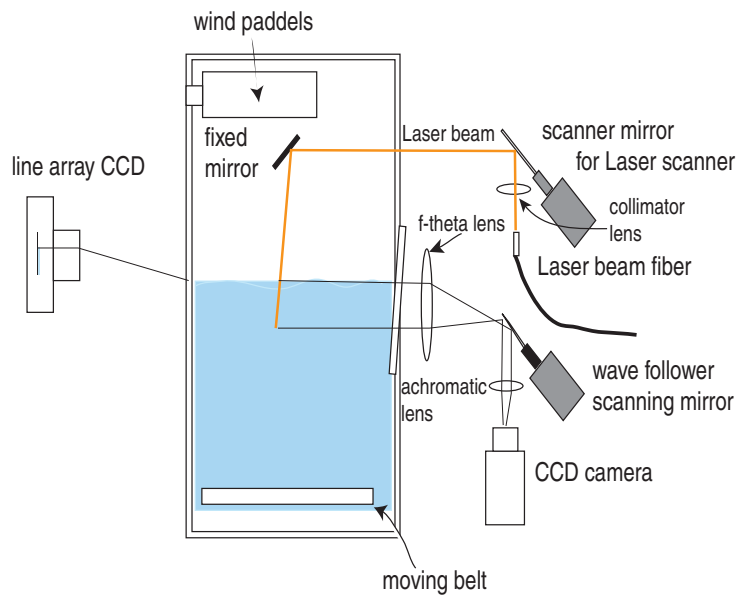[10]1W Argon ion laser at 488nm wavelength.

Figure 3.5: Wave follower installed at the Heidelberg wind-wave facility. The moving belt moves in the opposite direction of the flow and reduces the average flow speed.

scanning mirror which does not allow to follow the water surface precisely - this reduces the size of the clipping area of the image.

3.3.2 Stereo setup

Experiments were carried out at the circular Heidelberg wind-wave facility and the newly constructed AEOLOTRON circular wind-wave facility, which is about three times larger in the extend to the former. This section explains the stereoscopic setups constructed for the stereo PTV at the wind-wave facilities.

3.3.2.1 Heidelberg circular wind-wave facility

The (small) wind/wave facility at the Institute of environmental Physics at the University of Heidelberg has a cylindrical shape and the measures are as given in figure 3.6. The wind is generated by a rotating paddle ring. The main reason for the choice of a cylindrical shape is the infinite fetch which simulates optimally the conditions on the ocean. Because the interest of the studies lies in small scale processes such as capillary waves and related effects, which are in a range of $1 - 10\,cm$ in wave length, the resonant waves as a boundary effect are only a minor distur-
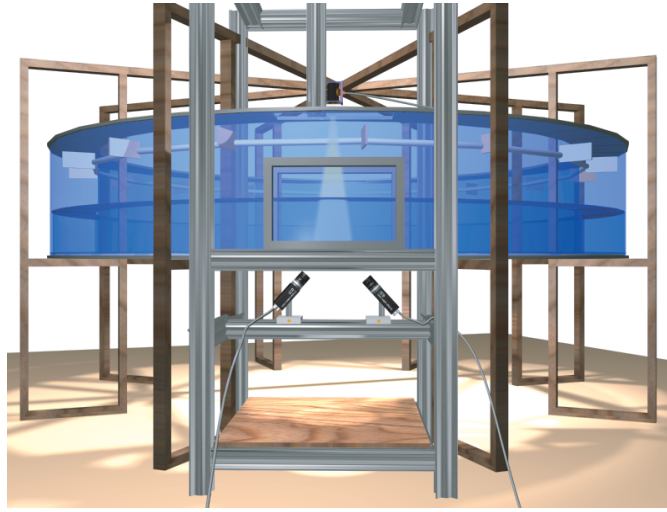
Figure 3.6: Circular wind-wave facility (previous) at Heidelberg University and the stereo PTV setup. Diameter (outer) = 4m, width = 0.3m, height = 0.7m, typical water height = 0.25m.

bance. This is demonstrated by a good agreement between wave spectra analysis of field and laboratory measurements (Klinke [1996]).

A major disadvantage of a circular flume is the wind induced momentum into the water bulk which causes a water current in the wind direction. The water current amounts up to $30\,cm/s$ at the water surface. The effects on the flow induced by the Corriolis-force are of minor importance. But the large (average) speed of the water bulk reduces the time of observation: A typical area of observation is of a size of $5\,cm$, which means the time of observation is about $1/6$ of a second only. To increase the time of observation a *moving bottom* has been installed. It rotates with a speed of up to $0.6\,m/s$ against the wind direction, and the mean water bulk velocity can therefore be compensated. The dependency of the moving belt speed to the induced surface velocity is almost linear (Münsterer [1996]).

The two CCD-cameras look from beneath the water surface through the transparent bottom and enclose symmetrically to the bottom an angle of about $90°$. This implies a significant refraction and therefore a dispersion of the (white) light rays hitting the camera CCD-plane. The dispersion was reduced by the usage of a color filter. For this reason the filter had to be chosen in such a way, that the spectral sensitivity of the CCD is high and the light source is of sufficient spectral intensity. The sensitivity of the CCD and the spectrum of the light source are both around $500\,nm$. A red-filter was used, where the band width was large enough to obtain a sufficient intensity of the light passing through. The refraction has to be taken into account for the model of the optical system and is discussed in section 4.3.
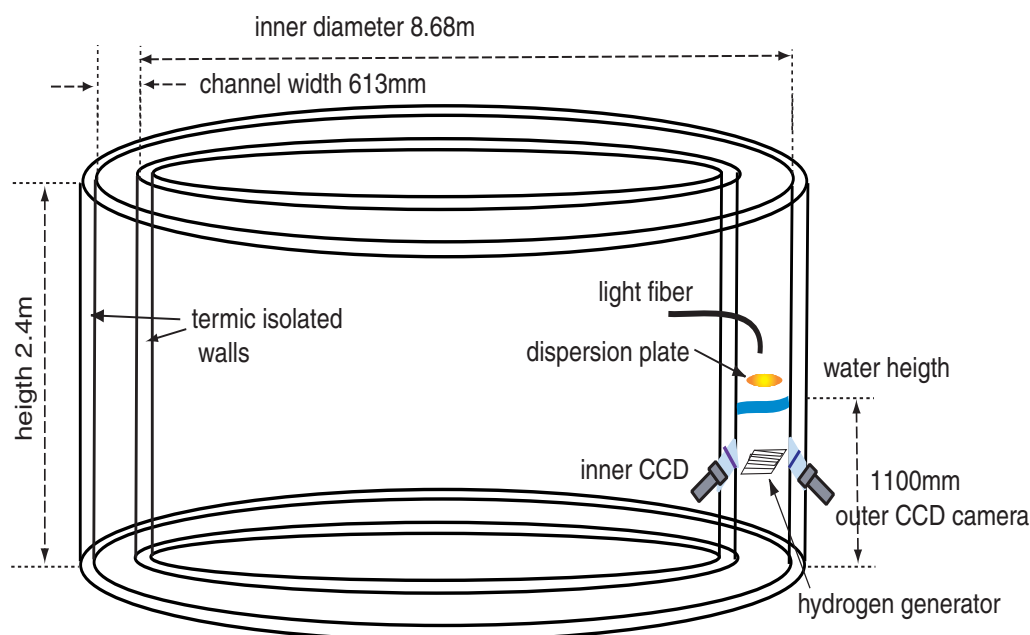
Figure 3.7: Scheme for the stereo PTV and the measures at the AEOLOTRON circular wind-wave facility at the Institute of environmental Physics, Heidelberg.

3.3.2.2 The large Heidelberg wind-wave facility (AEOLOTRON)

In the scope of this work the AEOLOTRON wind-wave facility was constructed. The measures are shown in figure 3.7. The inner diameter is 8.68 m and the inner width of the channel is 0.614 m, and the water fill height was 1.1 m from the channel bottom.

The walls of the channel are isolated by a 90 mm thick thermal insulator[11], which allows to set a water temperature range of 10°C to 50°C. An inner layer of a foil provides gas tightness of the channel and a second layer of an aluminum coated bitumen foil on the innermost side guarantees water tightness. Similar to the small wind-wave facility a belt driven paddle ring serves as the wind generator (0 to 25 m/s).

The two CCD-cameras look from the inner and the outer side of the channel, enclosing an angle $\theta = 26°$ to the flat water surface, through a pipe into the channel. Inside the pipe a plane window of optical glass, perpendicular to the optical axis of the lenses, works as a 'liquid prism' to minimize the refraction and dispersion effects of the light. The angles and position of the cameras can be moved as shown in figure 3.8.

---

[11]Styrodur, BASF AG.

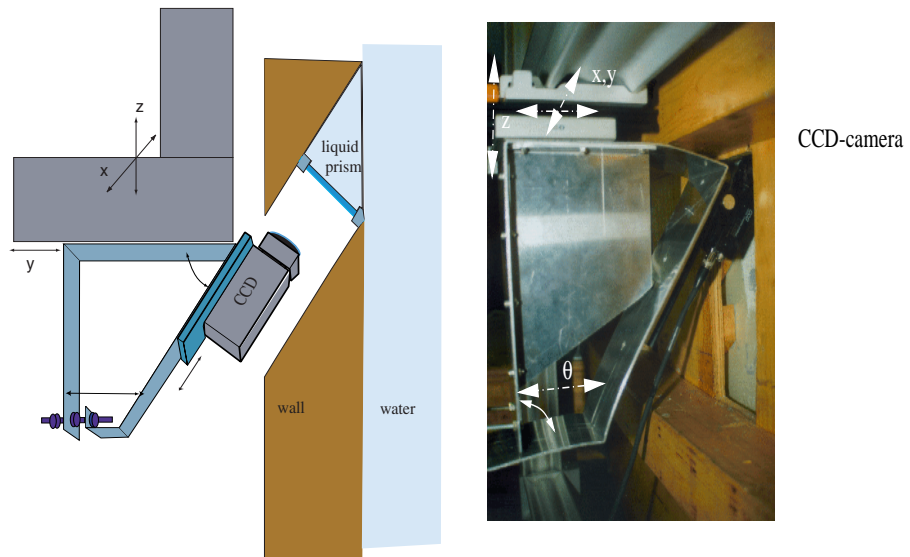Figure 3.8: CCD-Camera mount at the lateral walls of the channel. The camera is mounted on a x,y,z-shift device, the viewing angle θ of the camera can be adjusted. The camera view is directed against the inner of the channel through a pipe. A plane window of optical glass perpendicular to the optical axis of the lenses constitute a liquid prism. Left: Scheme of a single camera mount setup. Right: One of the two camera mounts.
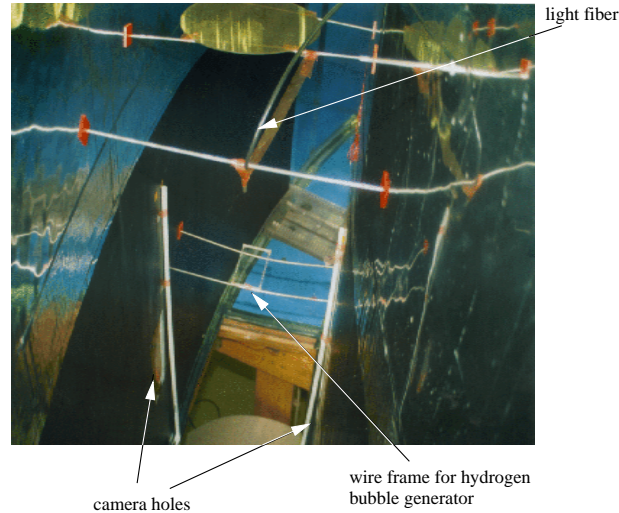
Figure 3.9: Stereo PTV setup. The optical fiber guides the light into the channel, the dispersive plate homogenizes the light and a wire frame generates the hydrogen bubbles.

A liquid optical fiber connected with a glow-discharge lamp guides the light into the channel (see figure 3.9). A dispersive plate homogenizes the light intensity in the volume of observation. The hydrogen/oxygen bubble generator is mounted beneath the volume of observation. It is slightly shifted in the opposite direction to the mean flow, depending on the speed of the flow and the velocity of the uprising hydrogen bubbles.

The setup for the calibration procedure is displayed in figure 3.10. The calibration target consist of an aluminum frame mounted between the walls of the channel and contains two grid planes separated by a given distance in z-direction. The two grid planes consist of intersecting lines at each grid point. The two planes are separated by a different orientation of the grid lines for each plane.

3.3.2.3 Volume of observation for stereo camera setup

The volume of observation is determined by the intersection of the two camera perspectives (figure 3.11). The optical axes of the cameras form an angle φ of about $26°$ in respect to the surface normal of the bottom window. It can be calculated from the parameters of the camera (which are determined by the calibration procedure) and the projected coordinates from the edge points of the two camera sensor planes to the world coordinates. The projected coordinates result in a ray (see section 5.3.5) and the world coordinates are determined by the top and bottom range

Calibration target   scattering disk   hydrogen generator
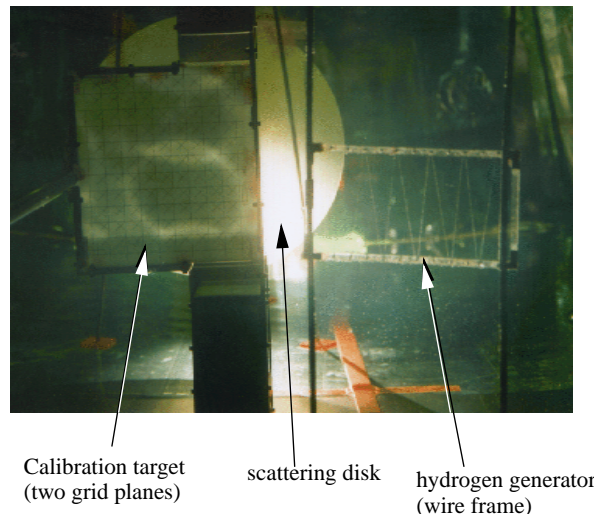(two grid planes)   (wire frame)

Figure 3.10: Calibration setup for stereo PTV measurements. The view is from the bottom of the channel.

of the focal depth (see section C.1). Due to lens distortions and other disturbances the rays are not straight, but slightly bent. The rays starting from the sensor and cutting the intersection volume determine the edges of a pyramid.

If the cameras are assumed to be aligned exactly opposite to each other with the optical axes enclosing an angle φ to the surface normal, and assuming furthermore the extend of the volume of observation being small in comparison to the distance between the sensor and the volume of observation, the pyramid lines (edge lines in figure 3.11) can be assumed to be parallel. This case can be reduced to two dimensions as shown in figure 3.12. The area A is then determined by $A = \Delta x \cdot \Delta y = 4D^2 \cdot \cos(\varphi)\sin(\varphi)$ which is maximized at $\varphi = 45^o$. The same considerations can be applied to a single CCD-sensor element. The volumetric resolution of the stereoscopic camera setup is then determined by the intersecting volume given by the CCD-sensor element. The choice of the angle φ depends on the requirements of resolution and on the restrictions given by the conditions of the experimental setup.

3.3.2.4   Technical data of used imaging devices

The technical data of the used lens system, cameras and frame grabber are listed in table 3.1. The frame grabbers have to have the capability to connect two cameras. The cameras have to be synchronized in time in order to get image pairs for each time interval of an image frame. The camera Pulnix TM 6701 AN is able to operate
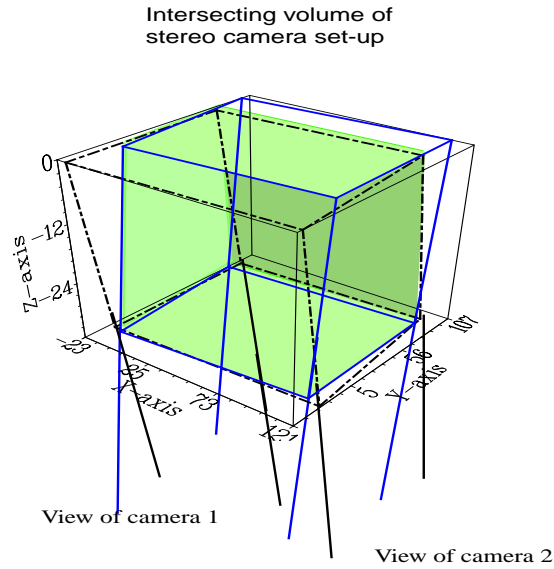
Figure 3.11: Volume of observation given by the intersection of the two camera views. The dashed and solid lines mark the views of camera 1 and camera 2, respectively. Bottom and top (Z-axis) are determined by the focal depth range of the two cameras.
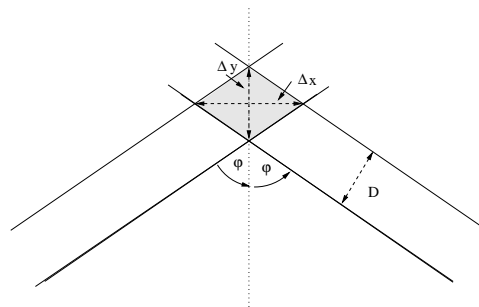

Figure 3.12: Volume of intersection as a function of the angle φ in two dimensions, simplified.

Camera	Pulnix TM 6701 AN	Sony XC-73CE
CCD-type	1/2" progressive scanning interline transfer CCD	1/3"
Pixels	648 (H)*484 (V)	752 (H)*582 (V)
CCD-cell size	$9.0\,\mu m$*$9.0\,\mu m$ (square pixels)	$6.5\,\mu m$*$6.25\,\mu m$
CCD size	5.83 mm*4.36 mm	6.0 mm*4.96 mm
Scanning frame rate	60 Hz full frame (non interlaced)	30 Hz (non interlaced)
Pixel clock	25.49 MHz	14.1875 MHz
Lens system	Tamron Zoom 35-70 mm (modified with shift and tilt device for Scheimpflug setup)	fixed focal length 25mm
Aperture	3.5-4.5	2.8
Frame-grabber	Mikrotron INSPECTA 2	Eltec PCEYE 4
Input channels	3*8 Bit RGB	3*8 Bit RGB

Table 3.1: Technical data of lens system, camera and frame-grabber.

in full resolution (648 horizontal and 484 vertical pixels) mode at 60Hz (standard video is 30 Hz). The higher the frame rate, the higher are the particle velocities which can be extracted. Therefore the frame rate is an important parameter for the dynamic resolution of the flow field.

The Sony XC-73CE was used for the determination of the hydrogen bubble velocity distribution where the frame rate (30 Hz) was of no importance.

3.3.3 Improvements for stereoscopic flow visualization

Compared to the classical PTV setup, the following improvements for the experimental setup were made:

- illumination from the top of the water surface

- liquid prism

- Scheimpflug camera setup

The classical PTV used a light source from the bottom of the channel (see section 3.3.1). This resulted in light reflections at the water surface which disturb the images taken by the CCD camera. An illumination from the top avoids this effect but results in light intensity variations depending on the steepness of the water surface.

A main disadvantage of the stereo PTV setup in 3.3.2.1 was the refraction of light at the air-water interface of the channel (air/ perspex/ water interfaces) due to the large angle of refraction (about 45°). This caused a bending of the epipolar lines which could not be compensated well enough by a multiple media module in the calibration and stereo coordinate evaluation module. Therefore a liquid prism (see figure 3.8) was introduced in the AEOLOTRON wind-wave facility (section 3.3.2.2) and the angle of refraction was minimized.

A further improvement is the Scheimpflug setup (discussed in the next section) which increases the depth of field range. This depth of field is a crucial parameter for the spatial resolution of the stereo PTV method. The depth of field for a usual lens system is only about 10-30 mm whereas the volume of observation should exceed a depth range of about 30 to 150mm.

3.3.3.1   Scheimpflug stereo camera setup

Three different typical stereoscopic setups are shown in figure 3.13 (a) to (c). For the translational method 3.13 (a) all its planes (object, lens and image) are parallel. For the angular method 3.13 (b) the image and lens planes are parallel, the object plane is turned by an angle of θ towards these planes.

The accuracy of the out of object plane component z depends on the distance S, where the translational system imposes an upper bound of the value S and therefore a limit on the visible area in the object plane. The angular method implies a larger angle θ which has no upper bound. Therefore the accuracy of the out of plane component of the angular system is, in principle, higher. Furthermore the visible area in the object plane is larger in the angular system due to the CCD sensor in the image plane, which is in standard cameras symmetric to the center of the lens. Obviously the objects in the object plane are no longer in the focal plane in the case of the angular method. This leads to an increase of the depth of field of the optics. The depth of field is given by

$$\Delta z = 4(1 + M^{-1})^2 O^2 \lambda$$

where M is the magnification of the object, O is the *f-number* (section C) and λ is the wave length of the light source.

A sketch of the Scheimpflug setup is shown in figure 3.13 (c). The Scheimpflug condition is described in the following: The center of the coordinate system is placed to O, the z-distance of the planes from the lens plane through O is

for the lens plane
$$z = 0$$

for the object plane

$$z = x \cdot \tan(\theta) - d_o$$

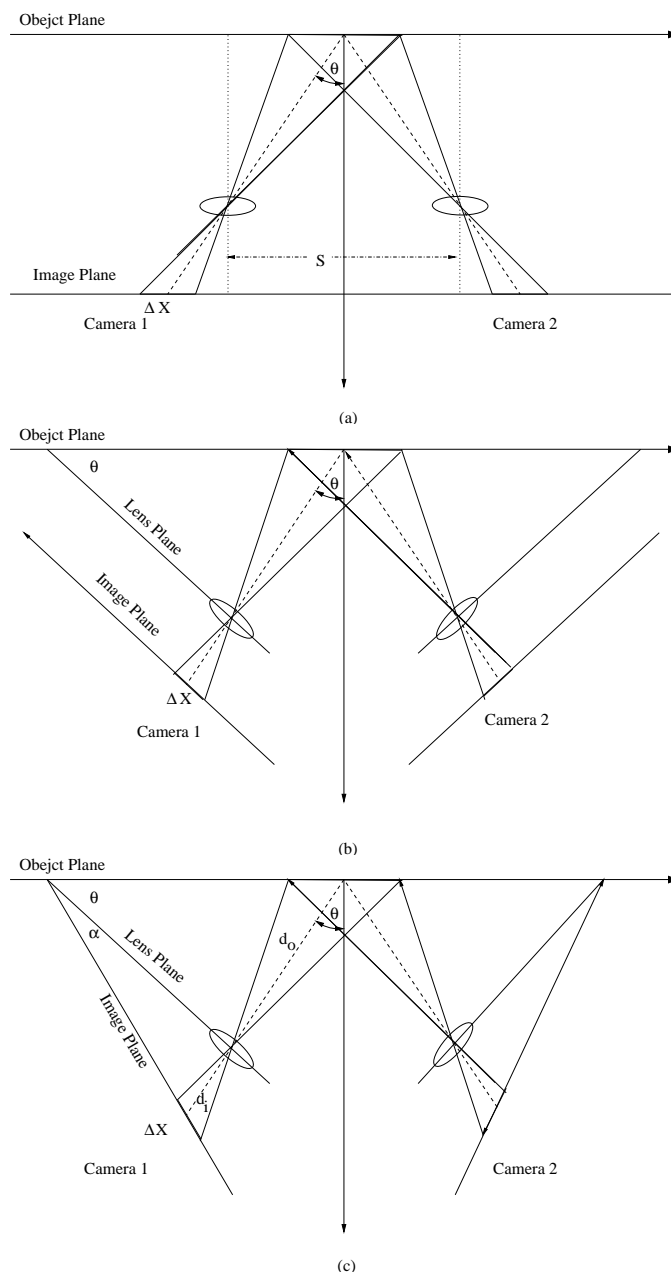and for the image plane

$$z = -x \cdot \tan(\alpha) + d_i.$$

Figure 3.13: Different stereoscopic methods. (a) translational method, (b) angular method, (c) Scheimpflug method.

Chapter 4

Geometry of the stereoscopic system

To handle the system numerically, a model has to be specified. This is done in this chapter by splitting the system into its single components. Basically the system looks as shown in figure 4.1. Each component requires a description. The stereo camera setup used here requires two of these basic systems. The exactness of the model description is of crucial importance in order to obtain a high accuracy in the calibration procedure.

4.1   Model of the stereoscopic system

The stereoscopic system requires at least two different views of one scene. This can be obtained either by two or more cameras for a stationary or non stationary object, or by a moving camera where the object is stationary. A two camera system including the used coordinate systems is shown in figure 4.2.

The object is located at $\overrightarrow{U}$ in the world coordinate system (U_1, U_2, U_3). The object point $\overrightarrow{U}$ is projected by the perspective transform through the center of projection ('pinhole') to the image planes of the left and right camera $\overrightarrow{u}_l$ and $\overrightarrow{u}_r$ respectively. The origin of the sensor coordinate system $(x_{l,r}, y_{l,r})$ is given by the intersection point - the *principal point* $\overrightarrow{P}_l$ on the left and $\overrightarrow{P}_r$ on the right image plane - of the optical axis and the image plane. The image plane is in a distance of the focal length $Z_{l,r} = f$ from the center of perspective. The sensor coordinates are transformed to the the image coordinate system $(u_{l,r}, v_{l,r})$, which is usually chosen with the origin at the top left corner.

Principally the camera model consists of intrinsic and external parameters. The external parameters describe the geometry and position of the camera system. This is shown for the simplest model, the pinhole model, in section 4.2.2. The intrinsic

Camera   Lens System   Mutliple Media   Object

CCD Sensor
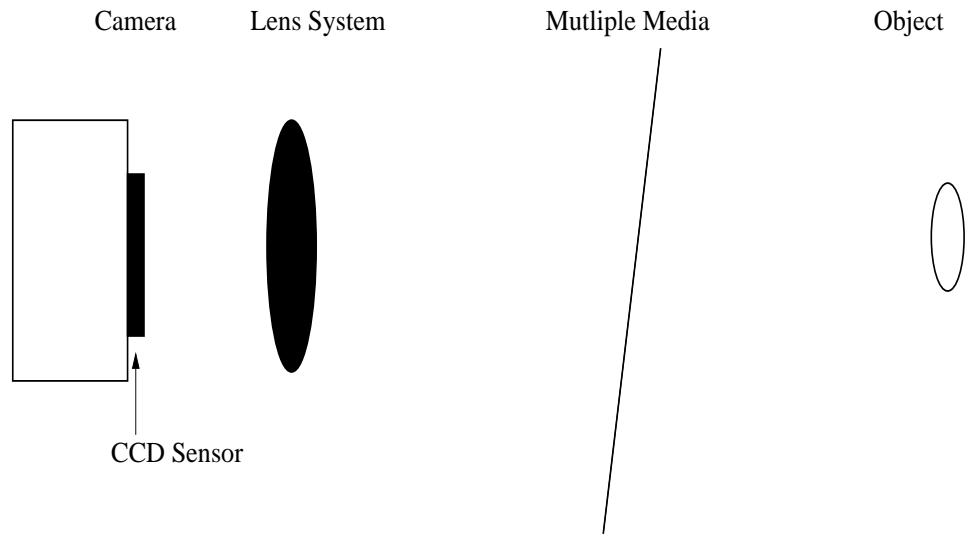
Figure 4.1: Basic system and its components for each camera setup.

image plane for left camera

image coordinate system

image plane for right camera

principal Point

u_l

x_l

$\vec{P_l}$

$\vec{u_l}$

v_l

y_l

center of perspective

O_l

X_l

Y_l

Z_l left ray

camera coordinate system
for left camera

v_r

$\vec{u_r}$

$\vec{P_r}$

u_r

x_r

y_r

center of perspective

O_r

camera coordinate system
for right camera

Y_r

Z_r

X_r

right ray

U_3

world coordinate system
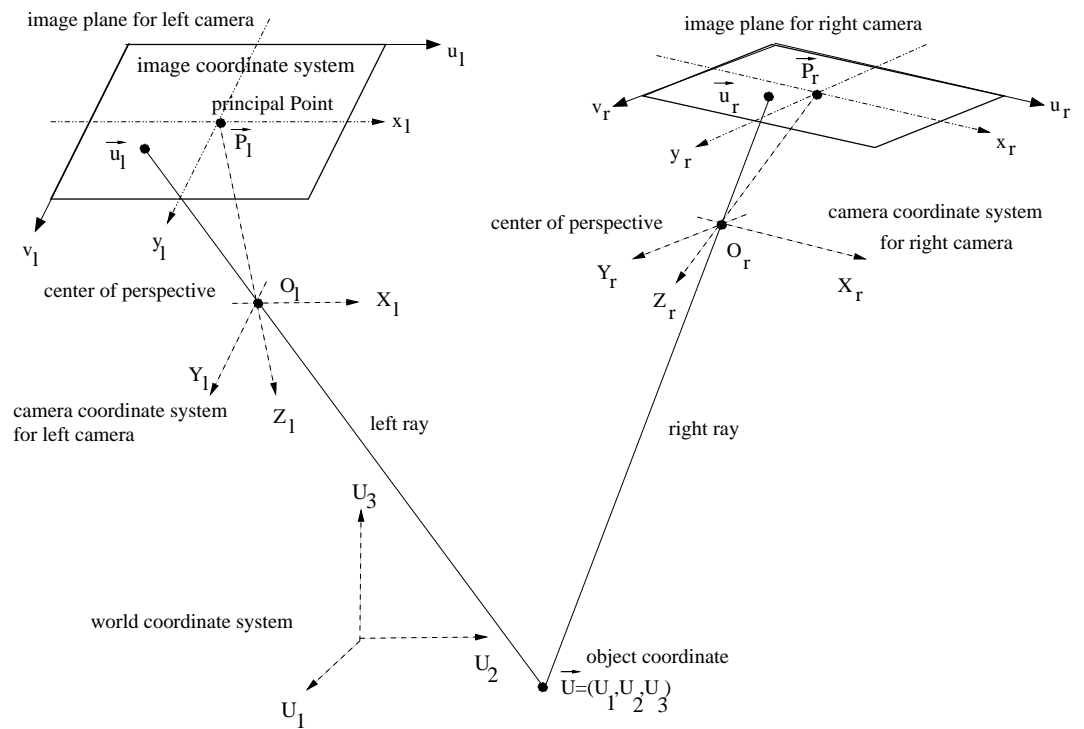
U_2

object coordinate
$\vec{U}=(U_1,U_2,U_3)$

U_1

Figure 4.2: Basic system for the pinhole camera model. The world coordinate $\vec{U}$ is
projected to the image coordinate $\vec{x_l}$ on the left, and $\vec{x_r}$ on the right image plane.
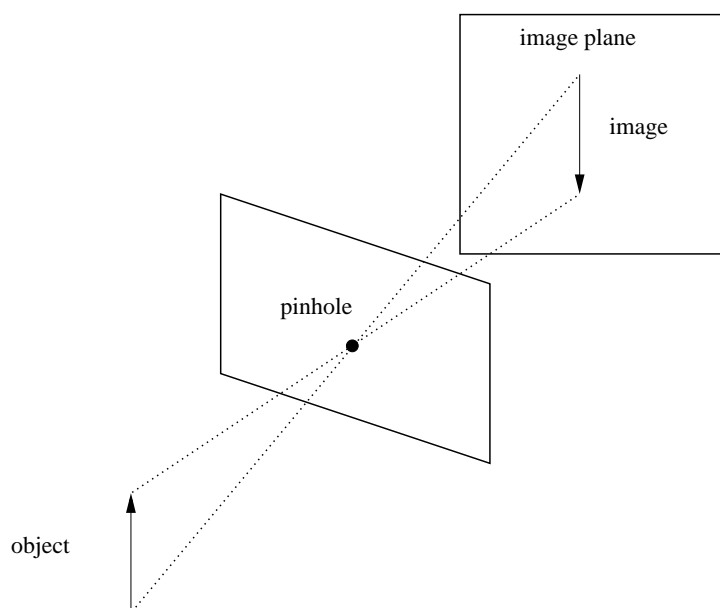
Figure 4.3: Pinhole camera model.

parameters are not related to position and geometry but to camera and lens system specifics. It transforms the sensor coordinate system to the image coordinate system (the 'user' coordinates). This is discussed for the pinhole model in section 4.2.3 (see also Faugers [1993]).

4.2 A simple camera model

Looking from the geometric point of view, the simplest model is the pinhole camera model. Figure 4.3 shows the setup; the first screen has been punched with a small hole where the rays of the emitted or reflected light passes.

The pinhole camera model represents an ideal camera, free from any distortions and other artifacts. The model is a rigid body transformation and a projective transformation applied afterwards. The pinhole camera is explained in section 4.2.2. The model can be described in a matrix style applying the homogeneous coordinate system which is shown in the next section.

4.2.1 Homogeneous coordinate system

The perspective projection P maps the camera coordinate system $\overrightarrow{X}$ to the image coordinate system $\overrightarrow{x}$ ($P : \{\overrightarrow{X} \in \mathbb{R}^3\} \longmapsto \{\overrightarrow{x} \in \mathbb{R}^2\}$). Therefore, the relation between the object coordinate $\overrightarrow{X} = (X, Y, Z)^T$ and the image coordinate $\overrightarrow{x} = (x, y)^T$ is:

$$\begin{pmatrix} x \\ y \end{pmatrix} = -\frac{f}{Z} \begin{pmatrix} X \\ Y \end{pmatrix} \tag{4.1}$$

$\Leftrightarrow$

$$-\frac{f}{Z} = \frac{x}{X}$$
$$-\frac{f}{Z} = \frac{y}{Y} \tag{4.2}$$

The *homogeneous space* is introduced to be able to write equation (4.1) in a matrix form in the same way as the rotation and translation can be written in a matrix from. This allows to express the transformations in terms of the linear algebra and offers a way to deal with the methods and rules of linear algebra. The homogeneous space is an embedding of the *n*-dimensional physical space into the $(n+1)$-dimensional space by introducing a scaling factor t: $\vec{x} : \{(x_1, x_2, \ldots, x_n)^T \in \mathbb{R}^n\} \longmapsto \widetilde{\vec{x}} : \{t \cdot (x_1, x_2, \ldots, x_n, 1)^T \in \mathbb{R}^{n+1}\}$ where $\widetilde{\vec{x}}$ are called *homogeneous coordinates*. For example considering a plane $((x,y)^T \in \mathbb{R}^2)$, this plane is in the homogeneous space $((x,y,t)^T \in \mathbb{R}^3$ determined up to a translation on a straight line (in the direction perpendicular to the plane) by the scaling factor t. The physical space is obtained from the homogeneous space for $t = 1$.

The physical space $\vec{X} : \{(X,Y,Z)^T \in \mathbb{R}^3\}$ is embedded into the four dimensional homogeneous space by $\widetilde{\vec{X}} : \{t \cdot (X,Y,Z,1)^T \in \mathbb{R}^4, t \in \mathbb{R}\}$.

The projective transformation P (equation (4.1)) expressed in homogeneous coordinates ($P : \{\widetilde{\vec{X}} \in \mathbb{R}^4\} \longmapsto \{\widetilde{\vec{x}} \in \mathbb{R}^3\}$) is written as:

$$\begin{pmatrix} \widetilde{x} \\ \widetilde{y} \\ s \end{pmatrix} = \underbrace{\begin{pmatrix} -f & 0 & 0 & 0 \\ 0 & -f & 0 & 0 \\ 0 & 0 & 1 & 0 \end{pmatrix}}_{P} t \cdot \begin{pmatrix} X \\ Y \\ Z \\ 1 \end{pmatrix} \tag{4.3}$$

where $\widetilde{x} = x \cdot s, \widetilde{y} = y \cdot s$. The physical coordinate system refers to the homogeneous coordinate system for $t = 1$.

The matrix form (4.3) is written as

$$\widetilde{\vec{x}} = P \widetilde{\vec{X}}. \tag{4.4}$$

4.2.2   Pinhole camera model

The transformation equation describing the pinhole camera model is

$$\widetilde{\vec{x}} = P \cdot R \cdot T \cdot \widetilde{\vec{X}} \tag{4.5}$$

where T represents the translational part, R the rotational part and P the perspective projection transformation coordinates.

The rotation in the physical space is

$$R_3 = \begin{bmatrix} c(\gamma) \cdot c(\beta) & -s(\gamma)c(\alpha) + s(\gamma)s(\beta)s(\alpha) & s(\gamma)s(\alpha) + c(\gamma)s(\beta)c(\alpha) \\ s(\gamma)c(\beta) & c(\gamma)c(\alpha) + s(\gamma)s(\beta)s(\alpha) & -c(\gamma)s(\alpha) + s(\gamma)c(\alpha)s(\beta) \\ -s(\beta) & c(\beta)s(\alpha) & c(\beta)c(\alpha) \end{bmatrix}$$

where α, β, γ are the Euler angles, $c(\ldots)$ stands for $\cos(\ldots)$ and $s(\ldots)$ for $\sin(\ldots)$. In the homogeneous space the rotation is

$$R = \begin{bmatrix} R_3 & 0 \\ 0^T & 1 \end{bmatrix}$$

with $0 = (0,0,0)$.

The translation in the physical space is given by the vector $T_3 = -(x_o, y_o, z_o)^T$ and is written in homogeneous coordinates as

$$T = \begin{bmatrix} 1 & T_3^T \\ 0 & 1 \end{bmatrix}$$

with 1 the unit matrix in $\mathbb{R}^3$.

4.2.3 Pinhole camera model including intrinsic camera parameters

The transformation from the sensor coordinates $\widetilde{\vec{x}}$ to the image coordinates $\widetilde{\vec{u}}$ (usually the origin is the upper left corner of the image array) is described by the transformation matrix B. The intrinsic camera parameters include the (effective) focal length f, the image center ('principal point') (C_x, C_y) - which is defined as the intersection point of the optical axes of the lens system and the CCD sensor plane, and parameters related to the CCD sensor including

- N_x, N_y, the effective number of sensor elements in an image line (x-direction) and the effective number of lines (y-direction),

- S_x, S_y, the effective size of the sensor in x and y direction and

- α, a scaling factor which considers horizontal pixel sensor deviation due to synchronization of frame-grabber and CCD camera.

The transformation matrix for the internal parameters is given by

$$\widetilde{\vec{u}} = B \cdot \widetilde{\vec{x}}$$

where the 3×3 matrix B is

$$B = \begin{pmatrix} \alpha \frac{N_x}{S_x} & 0 & C_x \\ 0 & \frac{N_y}{S_y} & C_y \\ 0 & 0 & 1 \end{pmatrix}. \tag{4.6}$$

The model is then finally written as

$$\widetilde{\vec{u}} = F \cdot \widetilde{\vec{X}}$$

where F is the complete transform matrix ('fundamental matrix') with

$$F = B \cdot P \cdot R \cdot T. \tag{4.7}$$

4.2.4   The linear camera model

A linear camera model is obtained quite naturally when applying homogeneous coordinates. This model is described by the Direct Linear Transformation (DLT):

$$\widetilde{\vec{u}}_i = A \widetilde{\vec{U}}_i \tag{4.8}$$

where A is a 3×4 projective transformation matrix, projecting the vector $\widetilde{\vec{U}}_i = (\vec{U}_i, 1)^T$ (with world point $\vec{U}_i = (U_{1,i}, U_{2,i}, U_{3,i})^T$, to the image point $\vec{u}_i = (u_i, v_i)^T$ in homogeneous coordinates $\widetilde{\vec{u}}_i = t \cdot (\vec{u}_i, 1)^T$ (see equation (4.3)).

Equation (4.8) is in detail:

$$\begin{bmatrix} u_i t_i \\ v_i t_i \\ t_i \end{bmatrix} = \begin{bmatrix} a_{11} & a_{12} & a_{13} & a_{14} \\ a_{21} & a_{22} & a_{23} & a_{24} \\ a_{13} & a_{23} & a_{33} & a_{34} \end{bmatrix} \begin{bmatrix} U_{1,i} \\ U_{2,i} \\ U_{3,i} \\ 1 \end{bmatrix}.$$

The parameters $a_{11}, \ldots, a_{34}$ can be solved by eliminating t_i and solving the matrix equation

$$\mathbf{L}\mathbf{a} = 0$$

where

$$
L =
\begin{bmatrix}
U_{1,1} & y_1 & z_1 & 1 & 0 & 0 & 0 & 0 & -U_{1,1}u_1 & -U_{2,1}u_1 & -U_{3,1}u_1 & -u_1 \\
0 & 0 & 0 & 0 & U_{1,1} & U_{2,1} & U_{3,1} & 1 & -U_{1,1}v_1 & -U_{2,1}v_1 & -U_{3,1}v_1 & -v_1 \\
\vdots & \vdots & \vdots & \vdots & \vdots & \vdots & \vdots & \vdots & \vdots & \vdots & \vdots & \vdots \\
U_{1,i} & U_{2,i} & U_{3,i} & 1 & 0 & 0 & 0 & 0 & -U_{1,i}u_i & -U_{2,i}u_i & -U_{3,i}u_i & -u_i \\
0 & 0 & 0 & 0 & U_{1,i} & U_{2,i} & U_{3,i} & 1 & -U_{1,i}v_i & -U_{2,i}v_i & -U_{3,i}v_i & -v_i \\
\vdots & \vdots & \vdots & \vdots & \vdots & \vdots & \vdots & \vdots & \vdots & \vdots & \vdots & \vdots \\
U_{1,N} & U_{2,N} & U_{1,N} & 1 & 0 & 0 & 0 & 0 & -U_{1,N}u_N & -U_{2,N}u_N & -U_{3,N}u_N & -u_N \\
0 & 0 & 0 & 0 & U_{1,N} & U_{2,N} & U_{3,N} & 1 & -U_{1,N}v_N & -U_{2,N}v_N & -U_{3,N}v_N & -v_N
\end{bmatrix}
$$

and

$$
a = \begin{bmatrix} a_{11} & a_{12} & a_{13} & a_{21} & a_{22} & a_{23} & a_{13} & a_{23} & a_{33} \end{bmatrix}.
$$

The parameters $a_{11}, \ldots, a_{34}$ do not have any physical meaning. Physical parameters can be extracted by a method based on RQ decomposition proposed by Melen [1993]:

The transformation describes an extension of the pinhole model, including additionally the

1. correction of the measured image coordinates in the principal point (image center) $\overrightarrow{u} = (u_o, v_o)^T$

2. and difference in scale and lack of orthogonality between the image axes by (small) compensation coefficients b_1 and b_2:

$$
\begin{bmatrix} u_i' \\ v_i' \end{bmatrix} = \underbrace{\begin{bmatrix} 1+b_1 & b_2 \\ b_2 & 1-b_1 \end{bmatrix}}_{=:B} \left(\begin{bmatrix} u_i \\ v_i \end{bmatrix} - \begin{bmatrix} u_o \\ v_o \end{bmatrix} \right)
$$

or

$$
\overrightarrow{u}' = B \cdot (\overrightarrow{u} - \overrightarrow{u}_o)
$$

In homogeneous coordinates this can be equivalently expressed by

$$
\begin{bmatrix} u_i' \\ v_i' \\ 1 \end{bmatrix} = \begin{bmatrix} 1+b_1 & b_2 & 0 \\ b_2 & 1-b_1 & 0 \\ 0 & 0 & 1 \end{bmatrix} \cdot \underbrace{\begin{bmatrix} 1 & 0 & -u_o \\ 0 & 1 & -v_o \\ 0 & 0 & 1 \end{bmatrix}}_{=:V} \begin{bmatrix} u_i \\ v_i \\ 0 \end{bmatrix}
$$

or

$$
\widetilde{\overrightarrow{u}}' = B \cdot V \cdot \widetilde{\overrightarrow{u}}
$$

The inverse transformation, from $\widetilde{\overrightarrow{u}} \to \widetilde{\overrightarrow{u}}{}'$, is needed, where B^{-1} and V^{-1} has to exist.

$$B^{-1} = \frac{1}{1 - b_1^2 - b_2^2} \begin{bmatrix} b_1 - 1 & -b_2 & 0 \\ -b_2 & 1 + b_1 & 0 \\ 0 & 0 & 1 \end{bmatrix}$$

$$V^{-1} = \begin{bmatrix} 1 & 0 & u_o \\ 0 & 1 & v_o \\ 0 & 0 & 1 \end{bmatrix}$$

The matrix A (equation (4.8)) can therefore be written as

$$A = \lambda \cdot V^{-1} \cdot B^{-1} \cdot F \cdot M \cdot T \tag{4.9}$$

(scaling factor $\lambda \neq 0$, affects only t from homogeneous coordinates, equation (4.3)).

Altogether the physical model[1] has eleven degrees of freedom - eighteen minus six parameters from the orthogonality constraint of M and minus the scaling factor λ transforming to the physical space). The DLT matrix A can be computed by equation (4.9) provided the eleven physical camera parameters are given. The opposite problem, the extraction of the eleven physical camera parameters and the scaling factor λ from a given DLT matrix was solved by Shih and Faig [1987] and Faugeras and Toscani [1987] who developed complete and exact decomposition methods. Melen [1993] proposed an improved method based on the RQ decomposition method. If all object points are located on a flat plane, $z_i = 0$ can be chosen and the 4×4 DLT reduces to a 3×3 matrix.

4.2.5   Camera model including lens distortion

A significant distortion is the radial distortion of the lens and the decentering distortion. The effect on a regular grid is illustrated in figure 4.4 and figure 4.5.

The pinhole camera model is extended with a shift of the origin $\overrightarrow{u}'_i$ and a term $\overrightarrow{\delta}(\overrightarrow{q}'_i)$ which models the linear and the lens distortion (Fryer [1989]):

$$\overrightarrow{u}_i = \overrightarrow{v} + \overrightarrow{u}'_i + \overrightarrow{\delta}(\overrightarrow{u}'_i)$$

---

[1]The physical model is obtained by the projection of homogeneous coordinates to the physical space.
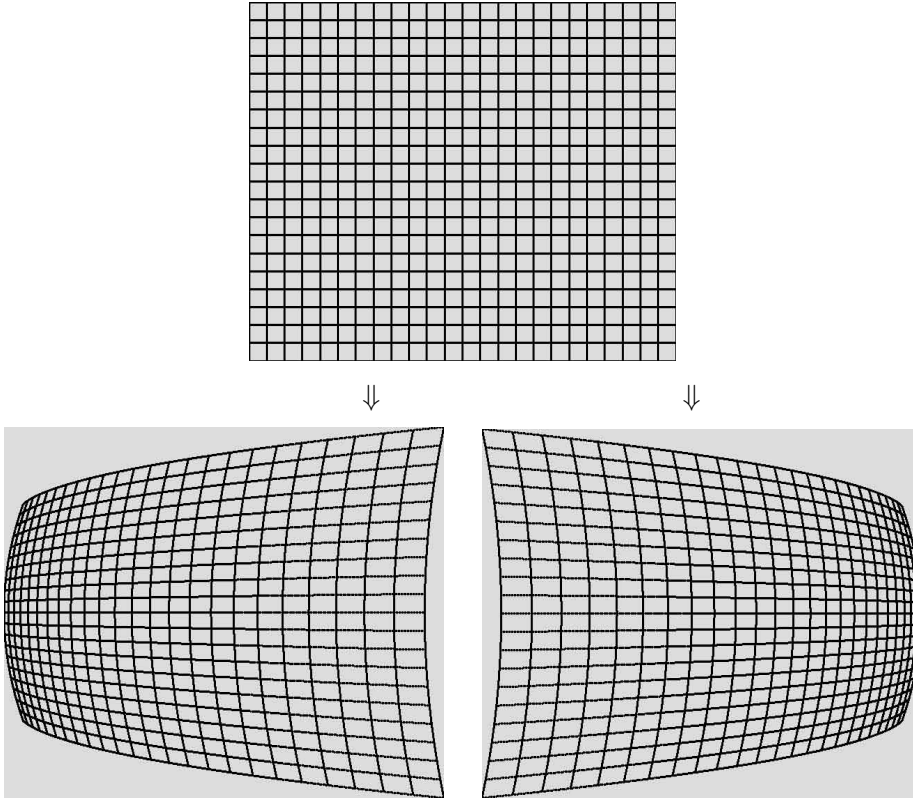
Figure 4.4: Lens decentering distortion (x-direction).

where $\vec{u}'_i$ are the undistorted coordinates from equation (4.4). The most widespread term for $\vec{\delta}$ in close range photogrammetry is

$$
\begin{bmatrix} \delta_u \\ \delta_v(u'_i v'_i) \end{bmatrix} = \underbrace{\begin{bmatrix} b_1 u'_i + b_2 v'_i \\ -b_1 v'_i + b_2 u'_i \end{bmatrix}}_{\text{linear}} + \underbrace{\begin{bmatrix} b_3 u'_i r_i^2 + b_4 u'_i r_i^4 + b_5 u'_i r_i^6 \\ b_3 v'_i r_i^2 + b_4 v'_i r_i^4 + b_5 v'_i r_i^6 \end{bmatrix}}_{\text{radial}} + \underbrace{\begin{bmatrix} 2b_6 u'_i v'_i + b_7 (r_i^2 + 2u'^2_i) \\ b_6 (r_i^2 + 2v'^2_i) + 2b_7 u'_i v'_i \end{bmatrix}}_{\text{tangential}}
$$

where $r_i^2 = u'^2_i + v'^2_i$. The linear distortion is described by b_1 and b_2, the radial distortion by b_3 to b_5 and the tangential distortion by b_6 and b_7. Depending on the amount of distortion and the required accuracy the number of coefficients for the radial distortion may be reduced or increased. In this work the first two (b_3 and b_4) were used. Thus four parameters modeling lens distortion are included into this extended camera model.

The parameters of this non linear camera model can not be determined analytically in contrast to the DLT discussed previously. Instead, a numerical method to minimize the camera transform F has to applied

$$
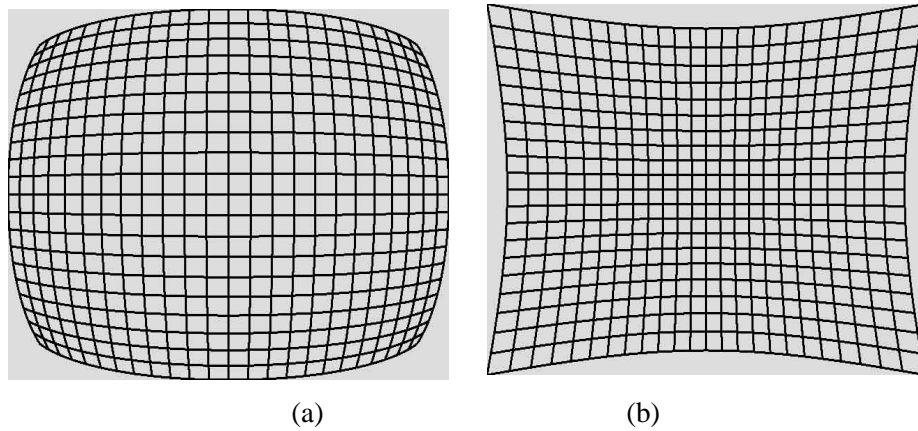\text{Res} = \sum_i (F(X_i) - x_i)^2 \rightarrow \text{minimum}
$$

Figure 4.5: Radial lens distortion barrel (a) and pincushion type (b).

where X_i are the world coordinates given by the calibration points of the calibration target (such as seen in figure 3.10), the x_i are determined in the 2D calibration procedure (section 5.1) and $F(X_i)$ is the projection to the image coordinates. The parameters are determined by a Least-Square optimization such as the gradient based Marquardt-Levenberg method. Start values are obtained from the DLT method. They guarantee vicinity to the global minimum and thus a high probability not to reach a local minimum.

4.2.6   Camera model and the Scheimpflug condition

For the Scheimpflug method the three planes - image plane, lens plane and object plane - are not parallel and intersect in a point (section 3.3.3.1). The geometry of the Scheimpflug method is shown in figure 4.6. The object plane with coordinate system (x,y) encloses an angle α with the optical axis and the image plane an angel θ.

For the Scheimpflug method the following relations can be derived from the geometry:

On the object side the following equations are valid:

$$o = d_o - \Delta o$$

$$\Delta o = x \cdot \cos(\alpha) \tag{4.10}$$

$$O = x \cdot \sin(\alpha)$$

Figure 4.6: Geometry of the Scheimpflug projection. The y-axis is perpendicular to the view, d_i is the image distance and d_o the object distance. Further explanations are found in the text.

and for the image side:

$$i = d_i + \Delta i$$

$$\Delta i = x \cdot \cos(\theta)$$

$$I = x \cdot \sin(\theta). \tag{4.11}$$

Taking the known projection equation

$$\frac{O}{I} = \frac{o}{i}$$

and substituting equations (4.10) and (4.11), the Scheimpflug transformation relation of the image coordinates (x', y') and the object coordinates (x, y) are found:

$$x' = \underbrace{\frac{d_i \cdot \sin(\alpha)}{d_o \cdot \sin(\theta) - x \cdot \sin(\alpha + \theta)}}_{transformation\ factor} x \tag{4.12}$$
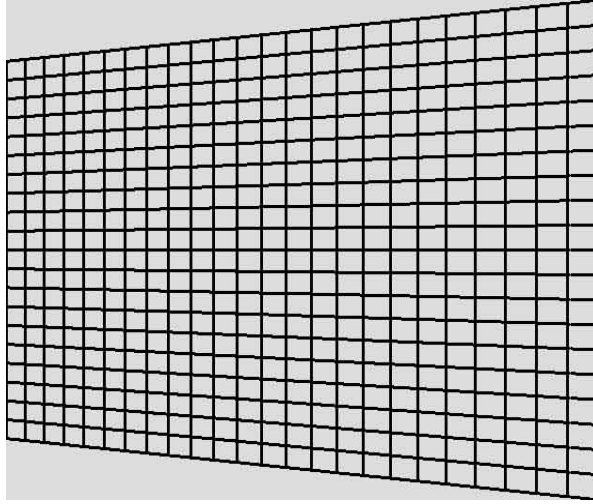
Figure 4.7: Effect of the Scheimpflug transformation (equations (4.12) and (4.13)) on a regular grid pattern.

$$y' = \frac{d_i \cdot \sin(\alpha)}{d_o \cdot \sin(\theta) - x \cdot \sin(\alpha + \theta)} y \qquad (4.13)$$

The transformation factor (equation (4.12)) is a function which depends on x only. The same transformation factor is also applied for the transformation[2] in y, equation (4.13).

This transformation includes four parameters d_i, d_o, α and θ. The parameters have to be included into the calibration procedure. The object distance d_i and the angle to the object θ were already included in the camera model. Thus the two parameters of the image distance d_o and the angle α to the image plane have to be determined additionally. Altogether the camera model has 17 parameters (15 from the camera model with lens distortion and from the Scheimpflug condition another two).

The result of this transformation (4.12) and (4.13) on a regular grid is shown in figure 4.7.

4.3 Multiple media geometry

If different media are involved in the optical setup then the optical geometry has to be taken into account. Three different media were used here: water, glass or perspex (window) and air. The larger the refraction angles, the larger the deviation $\overrightarrow{\Delta R}$, which is the distance from the projected image point $\overrightarrow{\tilde{x}}'$ from the image point

---

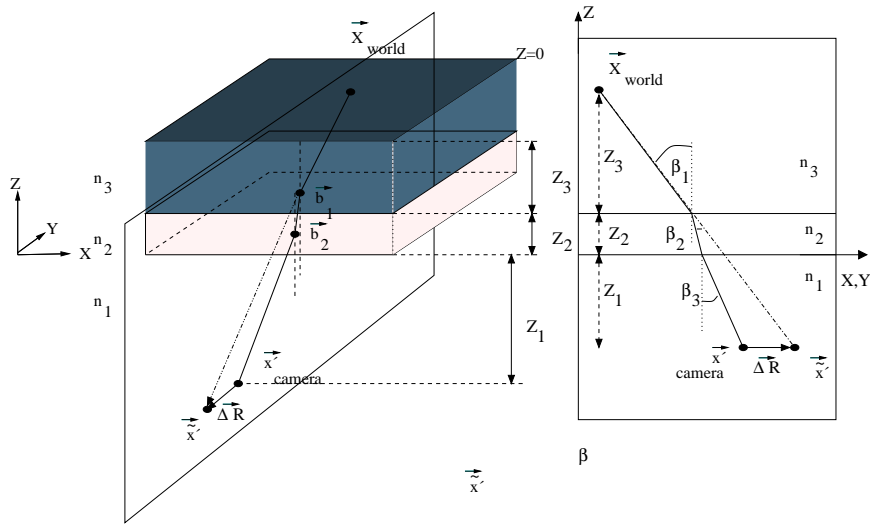[2]The independence of the transformation factor is due to the parallel invariance in the y-direction.

Figure 4.8: Multiple media geometry. A cross section through the volume in X, Z-plane is shown on the right side.

without different media $\overrightarrow{x}'$ (shown in figure 4.8). From the geometry of figure 4.8 the following equation is valid:

$$R = Z_1 \cdot \tan\beta_1 + Z_2 \cdot \tan\beta_2 + Z_3 \cdot \tan\beta_3 , \quad \overline{R} = (Z_1 + Z_2 + Z_3) \cdot \tan\beta_1$$

and for the refraction (Snell´s law)

$$n_1 \cdot \sin\beta_1 = n_2 \cdot \sin\beta_2 = n_3 \cdot \sin\beta_3.$$

This equation system has to be solved numerically[3] in order to obtain the coordinate $\overrightarrow{x}'$.

Dispersion is another significant effect which has to be considered if a non-monochromatic light source is used (such as the glow-discharge lamp used in this work). The dispersion for visible light varies significantly stronger in water (1.4%) as compared to air (0.008%), see Höhle [1971]. Light of shorter wavelength (blue) is refracted more strongly than light of longer wavelength (red). This effect leads to a color hem at the object projected on the image plane. If the sensitivity of the sensor is not constant, as is true for the CCD sensor where the sensitivity for red is larger than for blue, the center of mass of the projected object is moved. This effect can be reduced either by avoiding large refraction angles (such as liquid prisms do,

---

[3]For example in Maas [1992]; start value is $\overline{R}_o = \left| \overrightarrow{X} - \overrightarrow{x}' \right|$, then $\beta_{1,2,3}$ and ΔR are calculated. The iteration is done with $\overline{R}_{n+1} = \overline{R}_n + \Delta R$.
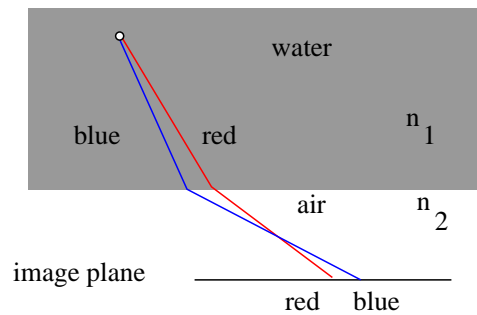
Figure 4.9: Dispersion of light in water for multiple media geometry and the effect of refraction at the water-air-water interface. The refraction index of water is $n_1 = 1.33$ and of air $n_2 = 1$.

applied in the stereo setup in the AEOLOTRON) or by reducing the bandwidth of the light source by a color filter (applied in the Heidelberg wind-wave facility).

Further deviations can be caused by inhomogeneities of the media in respect to the refraction index (due to temperature or pressure) or due to glass windows being not exactly plane. All of them are of minor importance for the setup as used in this work.

In fact, if the multiple media deviations were included into the calibration procedure, the convergence rate and residue for the parameter estimation (section 4.2.5) of the camera model (applied for the Heidelberg wind/wave facility, see Engelmann et al. [1998]) became worse. Because a real camera position in world coordinates is not required, the camera location is virtual.

Chapter 5

Image sequence analysis for stereo PTV

The main parts of the stereo-particle tracking velocimetry (stereo-PTV) method is shown in figure 5.1. For an overview of the different PTV methods see Engelmann et al. [1999b]. After the optical visualization of the flow field the two camera setups supply two image sequences for each camera perspective. These sequences are then processed separately. First the segmentation of particles - which are imaged as streak lines - is performed, as discussed in section 5.2.1. Next the particle tracking velocimetry method is applied (section 5.2). Finally the stereo correlation algorithm (section 5.3) is applied for the two processed image sequences and provides the trajectories in three-dimensional space (section 5.3.5).

To obtain quantitative results in image processing the calibration procedure is an essential part. The calibration procedure is discussed in detail in the next section.

5.1 Calibration

The aim of the stereo calibration procedure is to obtain the parameter set of the camera model 4.2. This is required to apply the stereo correlation algorithm and to reconstruct the three-dimensional coordinates of the particle trajectories (sections 5.3 and 5.3.5).

The camera calibration procedure consists of two basic steps which are discussed in the following sections:

- The 2D calibration procedure and
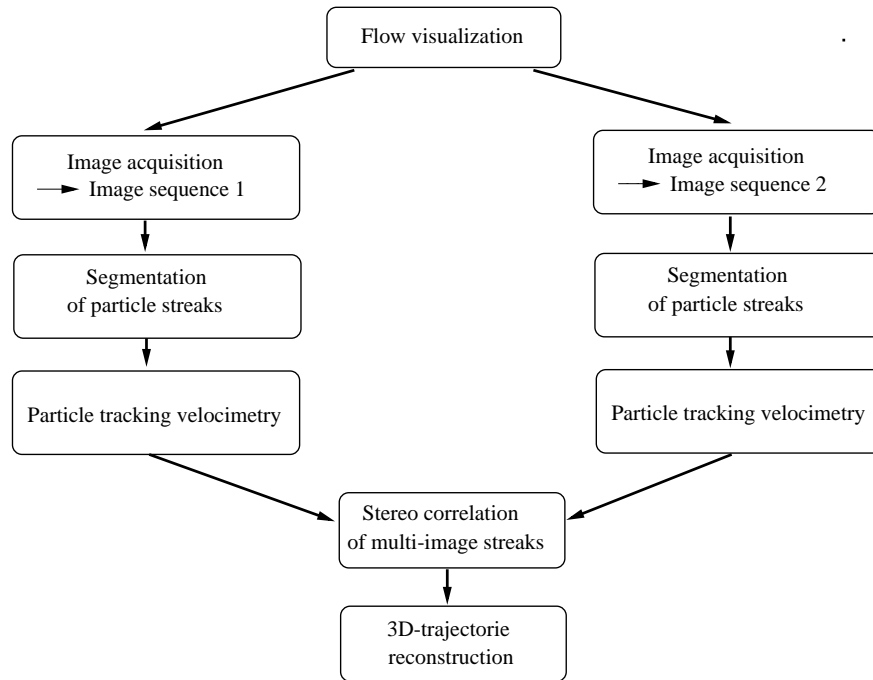
- the parameter estimation of the 3D camera model.

Figure 5.1: Overview of the stereo particle tracking velocimetry.

5.1.1 The choice of the calibration target

Investigations where performed at the Heidelberg wind-wave facility and the large Heidelberg wind-wave facility. According to the different properties such as geometry and accessibility, the mounting and calibration target was appropriately chosen. In both cases a grid pattern was used as a calibration target. The calibration procedure requires calibration marks not only in one plane, but at least in two different planes to solve the equations of the camera model. The quality of the calibration target is essential for the resolution obtained by the calibration procedure.

The experimental setup of the Heidelberg wind-wave facility was described in section 3.3.2.1. The calibration target is a quartz glass plate with grid lines imprinted.

The grid lines where imprinted onto the glass by a *Lift-Off* technique: The glass surface is coated with a photographic layer and this layer is exposed to light through a photographic mask (grid pattern). The light exposed part (the grid lines) is then removed and a metallic layer (60-80 nm thick aluminum or chromium) is put onto the surface. Removing the photographic layer results in a grid pattern of the metal layer. The precision of the grid lines depends mainly on the used mask. The mask was produced by a photographic printer (Linotype) which avoids thermic deformation of the substrate which usually appears if Laser printers are used. The resolution of the mask and the grid is 100 nm.

The calibration grid (a size of $5 \times 5\,cm^2$) was mounted on a linear shifting table and moved in z-direction, perpendicular to the flat water surface. A light source (glow-discharge lamp, Cermax) was mounted on the top. The light was guided through a collimator lens and a red filter was used to reduce the chromatic dispersion effects due to the refraction at the water surface. Images of the grid were taken in several distances from the water surface at $z = 0$ to a depth of $z = 5\,cm$ for both cameras.

In the case of the AEOLOTRON wind-wave facility (section 3.3.2.2) the shifting device could not be used. Similar to the calibration target used for the Heidelberg wind-wave facility a grid was used as a calibration target (see figure 3.10). The device consists of two grid planes separated in a given distance in z-direction ($30 - 60\,mm$). A foil with a grid pattern of a size of $20 \times 20\,cm^2$ was used. The Lift-Off technique could not be used because of its size limitations. As a light source the same glow-discharge lamp was used, but a color filter was not necessary due to the liquid prism construction (which minimizes chromatic dispersion effects at the air-window-liquid interface).

The two layer calibration grid requires an extended calibration procedure, as compared to the single grid plane moved by the shifting device. The next section explains this 2D-calibration procedure. In principal the procedure is the same in the case of the shifting device calibration, but the grid plane separation is skipped.

5.1.2   The calibration procedure

The aim of this 2D calibration was to identify the image coordinates with the world coordinates of the object, where the object is the 2D grid pattern. For the 3D calibration procedure two grid planes are required. There are two possibilities:

1. One plane which is moved in z-direction - at least two positions - where at each position a (temporally averaged) image is taken.

2. Two planes in fixed position and (z-) distance (figure 3.10), where the image includes both image planes.

The first method requires a precise moving facility such as a stepper of micrometer precision. There is no separation of the two planes necessary as in case 2. For the calibration target used in the large wind-wave facility method 2 was applied. The advantage of this method is the simpler setup. Furthermore it requires less physical space for mounting the calibration target. Here the cross line patterns of two grid planes are projected into the single camera image. Therefore a procedure is required which separates the two planes.

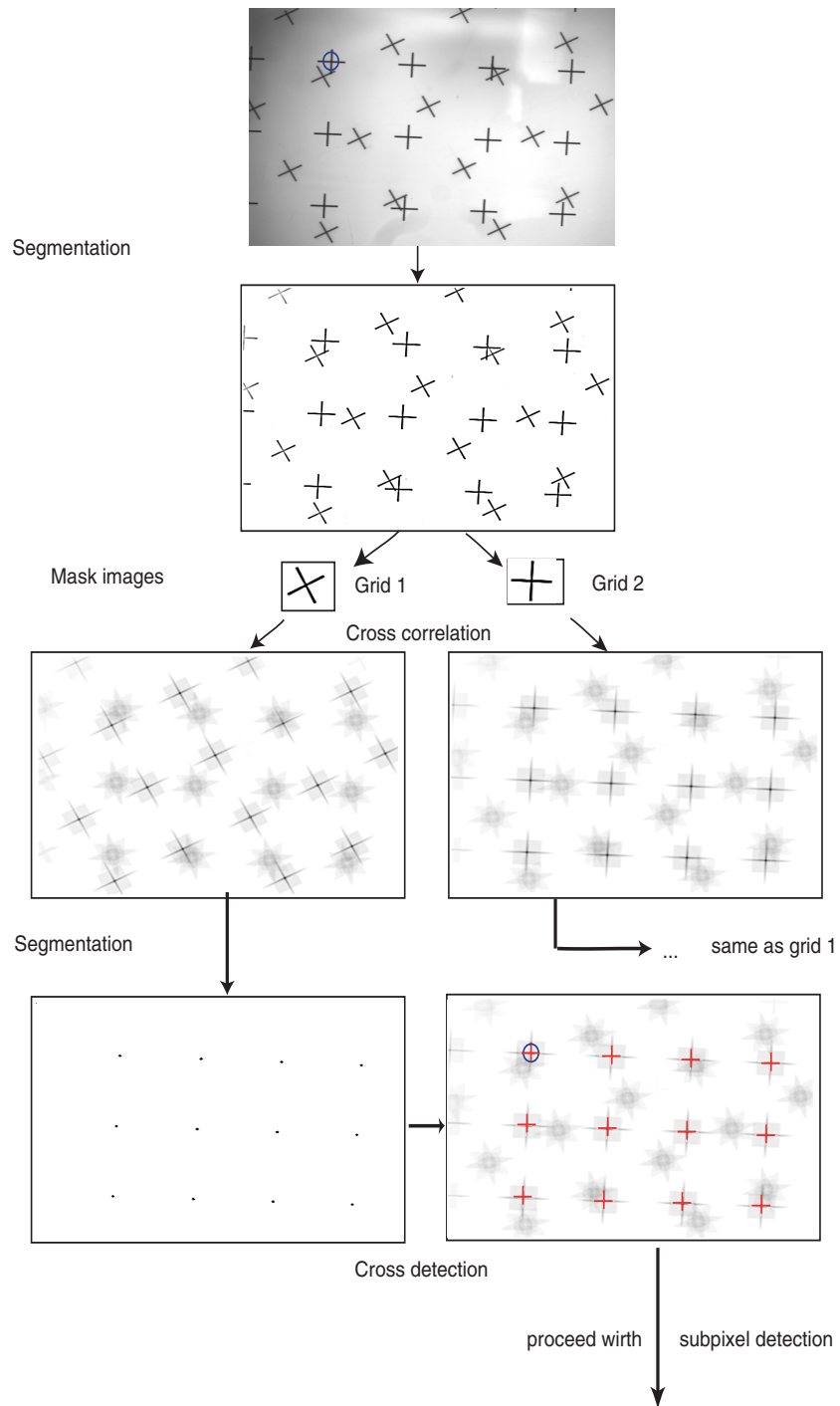The following procedure was used to find the center of the intersecting lines (figure 5.2):

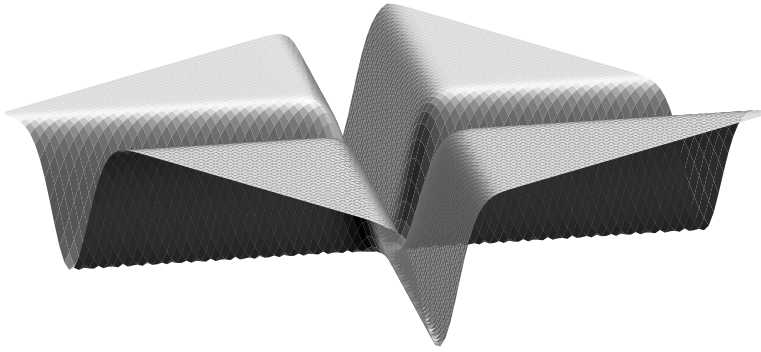Figure 5.2: Separation of two grid planes and localization of the intersecting lines.

Figure 5.3: The cross function equation (5.1) with parameters $w_1 = w_2 = 0.2$, $o_1 = o_2 = 0$, $h_o = 100$, $h_1 = 80$, $\theta_1 = -60^o$, $\theta_2 = 40^o$.

The first step is the background segmentation. It takes the inhomogeneous illumination into account.

The basic idea is to use the two cross types (for instance rotated by 45°) as template masks and to perform a cross correlation between the image and the two masks. As the second step the cross type is matched with the image and yields the two cross planes separately (second step in figure 5.2). The two cross types are now clearly visible and the cross correlation shows a maximum at the line intersection of the crosses. After background separation, the third step is a local maximum search[1] which yields the line intersections (bottom left in figure 5.2).

Taking the maximum from step three, the center of mass is determined in step four and serves as a starting point for the center point of the intersecting lines from which the direction (angle) of the cross arms is found by a line matching method. In step five the matching is done in a certain circular region where the middle point is the previously determined center point (bottom right in figure 5.2, region marked with a circle). The line is rotated stepwise around the line intersections and matched to the image data. The maximum of this matching characterizes the line and therefore its angle.

The previous procedure supplies the start parameters for step six, where the center of the intersecting lines is determined with sub-pixel precision. This is done by a minimization routine (modified Marquart-Levenberg method) where the function to be minimized is:

$$f(x,y) = h_o + h_1 \cdot \left(1 - e^{-w_1((y-o_2) \cdot \cos\theta_1 - (x-o_1)\sin\theta_1)^2}\right)\left(1 - e^{-w_2((y-o_2) \cdot \cos\theta_2 - (x-o_1)\sin\theta_2)^2}\right)$$

(5.1)

and the cross is shown in figure 5.3. The parameters are $h_o + h_1$ for the background (plateau), h_o being the height (or 'depth') of the intersecting lines, the intersec-

---

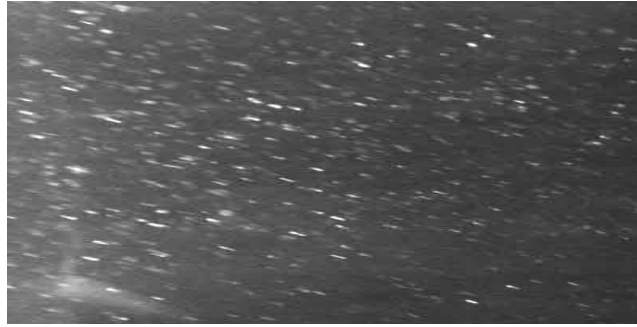[1]The maximum in a certain region, where the region size is in the order of the cross distance.

Figure 5.4: Streak image of particles. Due to the time of exposure Δt, spherical particles are not imaged as circular objects but 'smeared' over the time interval Δt and therefore imaged as streaks.

tion point (o_1, o_2) and the two angles θ_1 and θ_2 of the two intersecting lines with thickness w_1 and w_2 respectively.

With the knowledge of the cross distance and the z-distance of the two planes the world coordinates and the corresponding coordinates for the image plane are obtained. This list of image plane coordinates and world coordinates are the input for the 3D calibration procedure discussed in section 4.1 and the parameter estimation for the stereo camera model is done as shown in section 4.2.5.

5.2   The particle tracking velocimetry (PTV) algorithm

This section describes the two dimensional (classical) particle tracking velocimetry (PTV) algorithm which is a part of the image sequence analysis shown if figure 5.1. The purpose of the PTV is to trace each individual particle in an image over a sequence of images. The particles themselves are imaged as streaks[2] (figure 5.4). These streaks have to be identified in the images. First the streaks have to be found in the images which involves a segmentation procedure (discussed in section 5.2.1). This separates the pixels belonging to the streaks from the background. The segmented streaks are identified by a labeling procedure which marks each pixel belonging to a particle-streak uniquely. Finally the identified streaks have to be traced to the following images by solving the correspondence problem.

The steps of the PTV algorithm are shown in figure 5.5 and discussed in the subsequent sections.

---

[2]If the particles grey-value distribution at location $\vec{x}$ is $g(\vec{x})$ the streak is integrated over the time of exposure: $G(\vec{x}(t)) = \int_{t=t_o}^{t_o+\Delta t} g(\vec{x}'(t')) \, dt'$.
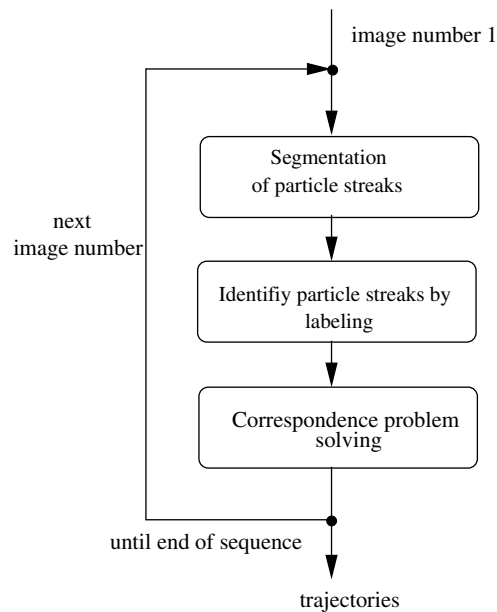
Figure 5.5: Overview of the PTV-Algorithm.

5.2.1   Segmentation

The separation of the object from its background is called *segmentation*. For a pixel at location (x, y) in the original image g the segmented image g_s is given by the following operation:

$$g_s(x, y) = \left\{ \begin{array}{lcl} 1 & : & g(x, y) \in \text{object (streak)} \\ 0 & : & g(x, y) \in \text{background} \end{array} \right.$$

Segmentation is the most critical step. The more streaks found, the better the segmentation works. Not segmented streaks are lost for further processing.

The segmentation should consider the following points for PTV:

- Variable size range of particles: The size distribution of the particles can vary up to a factor of 4 - typically the particles show, due to manufacturing processes, a normal distribution; i.e. for polycrystalline Optimage seeding particles ($30\mu m$ average diameter) it is about $\pm 20\%$ FWHM. Likewise, the size of the hydrogen bubbles can vary as shown in figure 6.8.

- Ignore light reflections: The walls and the water surface can be the cause for light reflections which are imaged as large 'objects'. A size criterion

(upper threshold for the number of pixels of a streak) for the object avoids this problem.

- Inhomogeneous illumination: This is caused by a non-ideal homogeneous light source and by light reflections. If the illumination is from above the water surface the illumination becomes inhomogeneous inside the water bulk due to refraction at the water surface. This occurs if the water surface turns wavy and the refraction angle changes - the main reason for inhomogeneity. If the time scale of the wave frequency is in the range of the frame rate of the camera, this inhomogeneity avoids taking the continuity of flow (section 5.2.3.1) as a criterion.

- Dynamic grey-value range: The grey-value of a streak depends - beside the illumination intensity - on the speed of the particle. Moving particles are imaged as streaks due to the time of exposure (chosen as maximally). If the velocity is higher, the streak length is larger and due to the continuity of the optical flow the grey-value intensity is therefore lower (see section 5.2.3.1)

Global segmentation methods are not well suited for the PTV. Local properties of the particles/streaks have to be taken into account.

Two methods are introduced in the following part, *region oriented* methods and *model based* methods. In this work the region growing method was used because of lower computational costs and therefore lower processing time.

5.2.1.1   Region oriented segmentation

Region growing method

This segmentation method looks for regions of similar characteristics in an image and fuses them together. By Matas and Kittler [1995] this method was proposed and applied by Wierzimok and Hering [1993]. The principle is illustrated in figure 5.6:

- The $n \times n$, $n = 1, 2 \ldots N$ square surrounding of a central pixel is enlarged gradually until no other pixel of the object (streak) is found. If the square intersects with another object in its 8-neighborhood, the two objects are considered as connected.

- The extent of the object (streak) is determined by a significance level (threshold) g of the grey-value.
  Local properties of the segmented streaks are extracted (see figure 5.7): The absolute   height g_{max},   the   minimum   of   the   height   difference
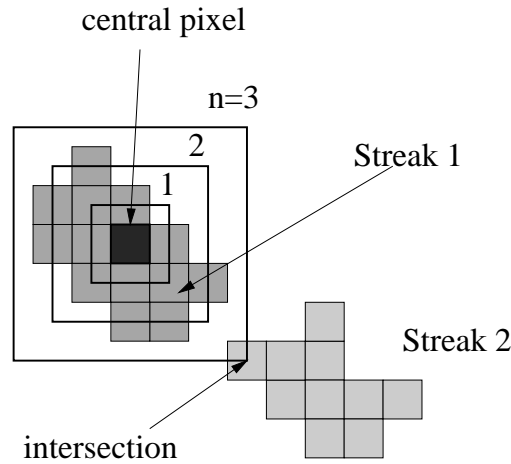
Figure 5.6: Principle of the region growing method.

$\Delta g = min_i(g_{max} - g_{min,i})$ where $g_{min,i}$, $i = 1 \ldots 4$, are the minima (in horizontal and vertical direction). An interpolation of the grey-value threshold $g_{i,j}$ is done by an ellipse (figure 5.7 (b))

$$g_{x,y} = \sqrt{g_i^2 \frac{\Delta y^2}{\Delta y^2 + \Delta x^2} + g_j^2 \frac{\Delta x^2}{\Delta x^2 + \Delta y^2}}$$

where the threshold height in horizontal and vertical direction is given by $g_i = g_{min,i} + s\Delta g$, $i = 1 \ldots 4$ (where s is the relative threshold level). A pixel is considered as belonging to a streak if its grey-value exceeds the threshold g_i and the width w does not exceed a given threshold.

Adaptive threshold segmentation

This method is quite similar to the previously described region growing method. The *background image* is calculated by a smoothing operation (for example a Gaussian kernel) which levels out small objects such as the particles. The size of the objects which are filtered by the smoothing operation depends on the smoothing operation (size of the filter mask). This background image is subtracted from the original image and a threshold is applied to remove objects (streaks) of very low intensity. This procedure is a high-pass filtering of the image which enforces the local grey-value contrast. The size of the filtering mask must be substantially larger than the object size. The object size is typically in the range of 3×3 to 15×15 pixels which requires a filter size of about 20×20 to 35×35. The resulting image
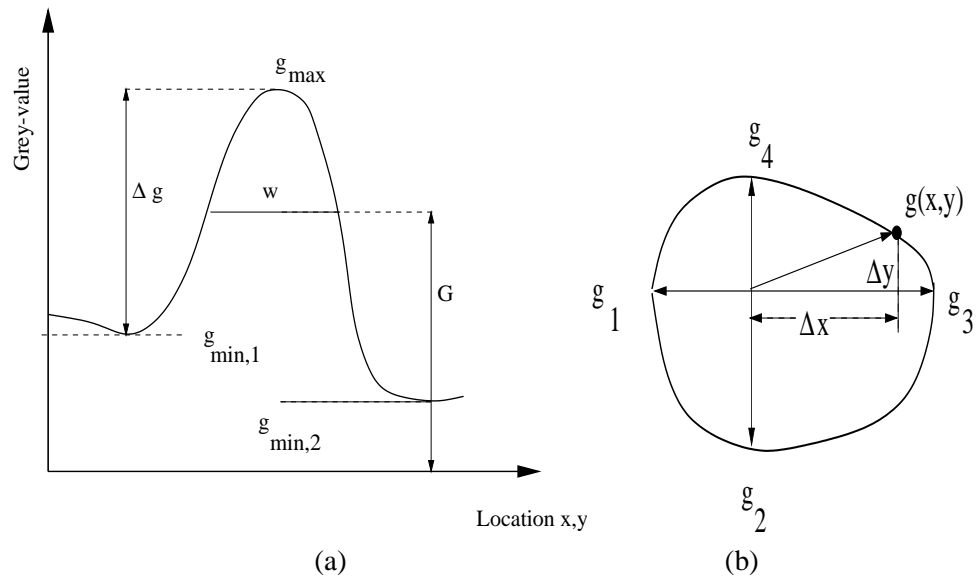
Figure 5.7: Characteristic properties used for region growing. (a): Grey-value of a streak depending on the location x, y on the image plane. (b): Interpolation of the grey-value threshold $g(x,y)$ on elliptic segments.

is binarized and a morphological dilation operation[3] enlarges the object. The result is a mask image[4] which is multiplied with the original image and therefore contains all segmented particles (figure 5.8). This method was applied for flow field measurements at the AEOLOTRON wind/wave facility. This method could also be applied for a very simple but efficient image compression. The ratio of the number of pixels belonging to a streak N_s to the number of pixels of the image N is small and the compression rate is a factor of N_s/N (usually about 100-200). To avoid a loss of data which is relevant for the determination of the streak after compression, the streak area should be enlarged in its neighborhood (i.e. by dilation).

The *local orientation* method (see Jähne [1997] chapter 15.5 for details) is another segmentation method which considers local properties of the objects region. This method yields a certain angle of the grey-value and the associated coherency measure within a given window size[5] from the second order momentum tensor. For the angle and the coherency measure a threshold can be applied - if the calculated value exceeds this threshold, then the associated pixel belongs to the object. This method was used for example as a pre-segmentation procedure for a model-based segmentation described in the next section. The disadvantage of this method is the

---

[3]Definition of *morphological dilation* operation: Input set X and result set Y, and K a structural element (mask). K is shifted over all elements $y \in Y$, and called K_y for each y. The dilation operation $\oplus$ is defined as: $Y = X \oplus K = \{y|K_y \bigcap X \neq 0\}$ (unification of mask K_y and image X, X not empty).

[4]If a pixel is set, it belongs to the object/streak.
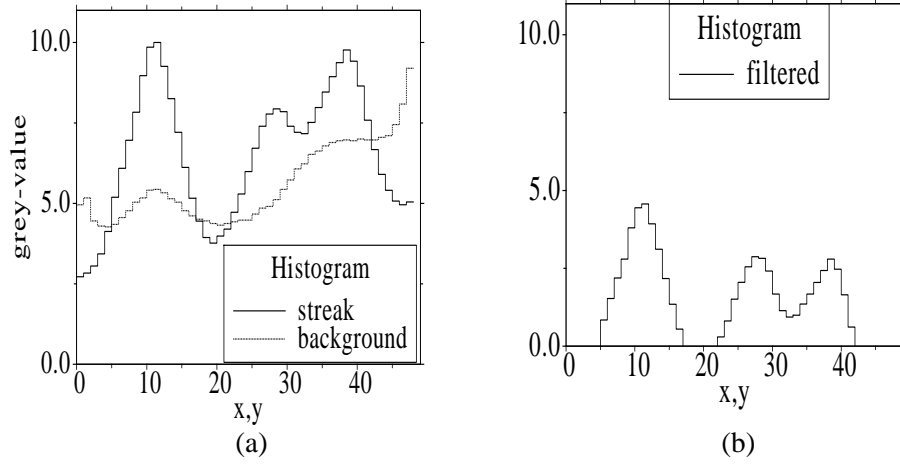
[5]The window size is determined by the filter size.

Figure 5.8: (a) Grey-value histogram of the original image and the background, subtraction results in (b) where two streaks are found.

large sensitivity on background signals such as defocused particles which are out of the volume of observation or light reflections from the wall.

5.2.1.2 Model-based method

This method considers the structure of the streak. The grey-value distribution is modeled by a particle moving in time. The particle grey-value (intensity $I(\overrightarrow{x}, \overrightarrow{x}_o)$) can be approximated by a Gauss function[6] (according to Hering et al. [1998]) of width σ

$$I(\overrightarrow{x}, \overrightarrow{x}_o) = \frac{1}{\sqrt{2\pi}\sigma} e^{-\left(\frac{(\overrightarrow{x} - \overrightarrow{x}_o)^2}{4\sigma^2}\right)}$$

where the particle starts at location $\overrightarrow{x}_o$ at time t_o. If the particle moves with a (constant) velocity $\overrightarrow{v}$ to location $\overrightarrow{x}(t)$ the streak is then approximated by the integral

$$g_s(\overrightarrow{x}) = \frac{1}{t_1 - t_o} \int_{t_o}^{t_1} I(\overrightarrow{x} - \overrightarrow{v} \cdot t, \overrightarrow{x}_o)\, dt \qquad (5.2)$$

This distribution can be split into a time dependent and a location dependent part due to separability and rotational symmetry of the Gaussian function I[7]:

---

[6]On condition that the particles are rotational symmetric: $I(\overrightarrow{x}) = I(|\overrightarrow{x}|)$

[7]Because of rotational symmetry and separability: $I(|\overrightarrow{x} - \overrightarrow{v} \cdot t|) = I\left(\sqrt{\frac{\overrightarrow{x}^2 \overrightarrow{v}^2 - (\overrightarrow{x} \overrightarrow{v})^2}{\overrightarrow{v}^2}}\right) \cdot$
$I\left(|\overrightarrow{v}| \left| t - \frac{\overrightarrow{x} \overrightarrow{v}}{\overrightarrow{v}^2} \right|\right)$. Separability: $I(x,y) = I(x) \cdot I(y)$.

$\implies$

$$g_s(\overrightarrow{x}) = I\left(\sqrt{\overrightarrow{x}^2 - (\overrightarrow{x}\,\overrightarrow{n})^2}\right) \frac{1}{2d} \int\limits_{\frac{d \cdot t_o}{t_1 - t_o} - \overrightarrow{x}_o \overrightarrow{n}}^{\frac{d \cdot t_1}{t_1 - t_o} - \overrightarrow{x}(t_1)\overrightarrow{n}} I(\tau)\,d\tau \qquad (5.3)$$

where the distance between the endpoints is $\overrightarrow{d} = \overrightarrow{x}(t_1) - \overrightarrow{x}(t_o)$ and
$\overrightarrow{n} = \dfrac{\overrightarrow{d}}{\left|\overrightarrow{d}\right|}$.

Applying a gradient based minimization method (such as the Marquardt-Levenberg method) for equation (5.3) on the streak pixels yields the parameters for the function. A pre-segmentation step is necessary to obtain start values for the minimization. The method of local orientation was used by Leue [1996].

Compared to the region growing method this model-based method yields very precise results for the end points of the streak. Its disadvantage is the large computational effort necessary to find start values and to obtain the model parameters by a minimization method. Usually the finding of the endpoints is not very critical because the correspondence solving (section 5.2.3) does not need a (sub-pixel) precise endpoint.

5.2.2   Labeling and position determination of a particle

The unique identification and marking of each streak is necessary for the following image processing steps. The method called *labeling* marks all pixels belonging to one streak with a unique number. The background is marked with a zero. The number of pixels with the same number is the area of a streak. This immediately allows to apply an area size criterion to get rid of objects which can not belong to a streak. An upper limit for the number of pixels thresholds the size of the streaks and reflections and other effects resulting in large objects are therefore filtered.

The moving (symmetric) tracer particles are imaged as streak lines due to the time of exposure[8] $\Delta t = t_1 - t_o$. This grey-value distribution is expressed with equation (5.2).

To determine the position of a streak, the center of mass is a good measure (Hering et al. [1998]). The center of mass $\overrightarrow{x}_s$ of the streaks grey-value is

$$\overrightarrow{x}_s = \frac{\int\limits_{-\infty}^{\infty} \overrightarrow{x}'\, g_s(\overrightarrow{x}')\, d\overrightarrow{x}'}{\int\limits_{-\infty}^{\infty} g_s(\overrightarrow{x}')\, d\overrightarrow{x}'}. \qquad (5.4)$$

---

[8]Chosen as maximum which is the inverse of the frame rate of the camera.

Substituting equation (5.2) into equation (5.4) and exchanging the integral over t and $\vec{x}$ results in

$$\vec{x}_s = \frac{\int\limits_{t_o}^{t_1} \int\limits_{-\infty}^{\infty} \vec{x}' I(\vec{x}', \vec{x}_o(t'))\, d\vec{x}'}{\int\limits_{t_o}^{t_1} \int\limits_{-\infty}^{\infty} g I(\vec{x}', \vec{x}_o(t'))\, d\vec{x}'} \tag{5.5}$$

The center of mass of the grey-value distribution $\vec{x}_o$ is defined as

$$\vec{x}_o = \frac{\int\limits_{-\infty}^{\infty} \vec{x}' I(\vec{x}', \vec{x}_o(t'))\, d\vec{x}'}{\int\limits_{-\infty}^{\infty} I(\vec{x}', \vec{x}_o(t'))\, d\vec{x}'} = \frac{1}{I_o} \int\limits_{-\infty}^{\infty} \vec{x}' I(\vec{x}', \vec{x}_o(t'))\, d\vec{x}'$$

and this $\vec{x}_o$ substituted into equation (5.5), results in

$$\vec{x}_s = \frac{I_o \int\limits_{t_o}^{t_1} \vec{x}_o(t')\, dt'}{I_o \int\limits_{t_o}^{t_1} dt'} = \frac{1}{\Delta t} \underbrace{\int_{t_o}^{t_1} \vec{x}_o(t')\, dt}_{<\vec{x}_o>} \tag{5.6}$$

Equation (5.6) shows that the center of mass over the pixel grey-values of a streak is equivalent to the expectation value $<\vec{x}_o>$ of a particle moving during the time of exposure Δt. $\vec{x}_s$ can therefore be taken as the (sub-pixel precise) position for each streak. This procedure is done for each streak of an image through the whole image sequence. To identify the particle (streak) in time uniquely the correspondence problem (in time) has to be solved. This is discussed in the next section.

5.2.3 Correspondence solving

The purpose of the PTV method is to obtain the trajectory $\vec{x}_i$ for each particle i. The particles are imaged as streak-lines in each image. After segmentation, the *correspondence problem* of identifying the same streak/particle in the consecutive image frames has to be solved.

The particles and therefore also the streaks are almost indistinguishable, the characteristics are only the grey-value, size (number of pixels per streak) and the orientation (length and width). Even the grey-value is a very poor criterion if the light intensity changes during the time of exposure Δt - which is the case in the experimental setups for the wind/wave facility AEOLOTRON and the small Heidelberg wind/wave facility (section 3.3.2.2).
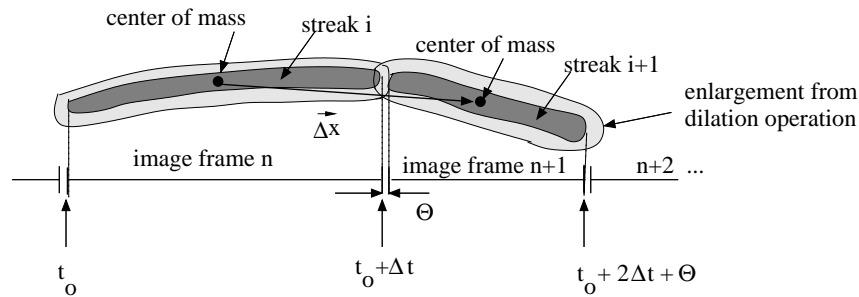
Figure 5.9: Corresponding streaks. The particles are imaged as streaks during the time of exposure Δt with their center of mass as the (average) position of the particle. Θ is the vertical synchronization time between two consecutive image frames. From a morphological dilation operation the pixel expansion of the streaks is enlarged (outer shaded area of the streaks).

The principle of the correspondence matching is shown in figure 5.9. The dark grey symbolizes the pixels of the streaks i imaged during the time interval t_o to $t_o + \Delta t$ and the subsequent streak $i + 1$ imaged during the time interval $t_o + \Delta t + \Theta$ to $t_o + 2\Delta t + \Theta$, where Δt is the time of exposure and Θ the vertical synchronization time of the video signal. The expansion of the streak is enlarged by a morphological dilation operation (light grey).

The two consecutive streaks i and $i + 1$ are marked as corresponding[9] if the dilated streaks (light grey) do overlap (this is equivalent to a logical and operation). The direction of the vector $\overrightarrow{\Delta x}$ is given by the known temporal order of the image frames and the (pixel grey-value) center of mass of the streak. The velocity is therefore $\overrightarrow{v} = \frac{\overrightarrow{\Delta x}}{\Delta t}$. This procedure is done for the whole image sequence. The consecutive overlapping streaks and their corresponding grey-value center of mass constitute the particles trajectories $\overrightarrow{x}_i(t)$.

To avoid unnecessary clustering of the streaks the dilation is not calculated simultaneously for all objects in an image but for each object individually.

5.2.3.1   Particle characteristics

The dilation operation is a sufficient criterion for the correspondence match if the particle concentration (number of particles per image) does not exceed about 100 particles (streaks) per image. If the concentration exceeds this limit, the probability for ambiguities in the correspondence match increases. If no correspondence is found or an ambiguity of correspondences occurs, further properties of the particles/streaks have to be taken as correspondence criteria. The characteristic properties are then taken to calculate a confidence measure. A confidence measure

---

[9]'caused by the same particle'

was implemented by F. Hering with usage of *Fuzzy-set* theory (details in Hering [1996]). Five characteristic properties (μ_i, $i = 1\ldots5$) are taken as fuzzy variables: 1) The distance of the current streak from the streak in the previous image, 2) the distance from the current streak from the estimated position in the next image, 3) the difference of the current velocity of the streak from the velocity in the previous image, 4) the grey-value difference of the streak in the current image from the previous and 5) the difference of the streak area in the current image from the previous. These five values are then linked by Fuzzy-logic lookup tables (in all combinations of μ_i) with the confidence measure $Conf(\mu_i)$ and the resulting confidence measure is $K = \frac{\sum_{i=1}^{5} Conf(\mu_i)}{\sum_{i=1}^{5} \mu_i}$. The candidate of the largest K is taken as corresponding.

The characteristic properties of the particles are discussed in the following part of this section.

Area and grey-value sum of a streak

The number of pixels constituting a streak can be taken as a characteristic of a streak. The particles are solids and can be assumed as rotational symmetric - and therefore they do not change their shape. But the projection of the particle on the image plane of the camera changes the particle image according to the point spread function. If the particle gets more defocused, the size of the image increases. This case is typical for the stereo-PTV measurements where the experimental setup is done in such a way that the range of the focal depth of field is large (to increase the intersecting volume of observation of both cameras, see section 3.3.2.3) compared to the classical PTV technique where a thin light sheet is used and the focal depth is in the range of the light sheet thickness.

Continuity of the optical flow

For moving particles with a velocity $\vec{u}$ and a given time of exposure of the CCD sensor Δt the grey-value g of the imaged particle is not a constant but a function $g(\vec{u}, t)$. If the grey-value g is *only* a function of location $\vec{x}$ and time t then the total differential equation for the optical flow is written as

$$dg(\vec{x}, t) = \sum_i \frac{\partial g}{\partial x_i} dx_i + \frac{\partial g}{\partial t} dt = 0$$

$\Leftrightarrow$

$$\frac{\partial g}{\partial t} + \vec{u} \cdot \nabla g = 0 \qquad (5.7)$$
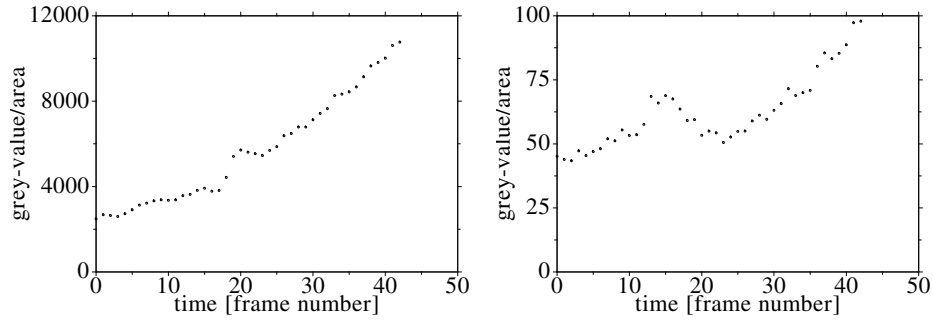
where $\vec{u} = \frac{d\vec{x}}{dt}$.

Figure 5.10: Grey-value sum of a streak over time (left) and the grey-value sum per area of the streak (right) for stereo PTV setup.

The well known continuity equation of hydrodynamics (conservation of mass with density of mass ρ instead of g) is $\frac{\partial \rho}{\partial t} + \nabla(\rho \cdot \overrightarrow{u}) = 0$, which is the same as equation (5.7) if $\nabla \cdot \overrightarrow{u} = 0$. Integrating the grey-value over the area Ω of a streak and applying the Gauß-integral[10] $\int_{\Omega} \frac{\partial g}{\partial t} dx dy + \overrightarrow{u} \underbrace{\oint_{\partial \Omega} g \, ds(x,y)}_{=0} = 0$ leads to a constant grey value for the streak

$$G = \int_{\Omega} g \, dx \, dy = const.$$

The sum of all pixel grey-values is therefore constant; the required assumptions are a homogeneity of the illumination over time and space, a boundary of the particle where the grey-value is zero and the particle shape is constant in time.

In figure 5.10 the grey-value sum and the grey-value sum per area over time of a streak is shown. This illustrates the typical case for the stereo PTV setup where a particle becomes defocused, the illumination intensity changes and therefore the grey-value is not constant (left part of figure 5.10). As defocusing enlarges the streak, the grey-value per area should be constant in the first order[11] (see Geissler and Scholz [1999]) if the illumination is constant. The grey-value per area is not constant as seen in the right part of figure 5.10 and therefore the illumination is not constant either. If the variation of the grey-value and the area of a streak is smooth or shows small changes from one image to the next, a threshold for the variation can be set as a criterion of correspondence.

---

[10]

$$\int \int_{\Omega} \nabla g \, dx \, dy = \int_{\partial \Omega} g \, ds(x,y)$$

On the boundary of the particle $g|_{\partial \Omega} = 0$

[11]In a simple single lens system and a first order approximation the blurring radius ε of an object moved out of the focal plane by the distance Δd is linear: $\varepsilon \sim \Delta d$.

5.2.3.2 Velocity estimation

If further ambiguities of corresponding streaks exist, a velocity estimation can be a good criterion for solving the correspondence search. The available information at time t_N is the streak position (section 5.2.2) $\vec{x}(t_N)$ and all the previous positions $\vec{x}(t_i)$, $i = 0, \ldots, N$ at time t_i. This information is used to estimate the position at time t_{N+1} and a χ^2-test is used to obtain the most probable corresponding candidate (see Hering et al. [1996]).

The choice of the model for the velocity estimation depends in particular on the velocity range of the particles. The simplest models are linear, such as

$$\vec{x}(t_{N+1}) = \vec{x}(t_N) + \vec{u}(t)\Delta t$$
$$= 2\vec{x}(t_N) - \vec{x}(t_{N-1})$$

where $\vec{u}(t_N) = \frac{\left(\vec{x}(t_N) - \vec{x}(t_{N-1})\right)}{\Delta t}$ and $\Delta t = 1$

or if acceleration is taken into account

$$\vec{x}(t_{N+1}) = \vec{x}(t_N) + \vec{u}(t)\Delta t + \frac{1}{2}\vec{a}(t)\Delta t^2$$
$$= \frac{1}{2}\left(5\vec{x}(t_N) - 4\vec{x}(t_{N-1}) + \vec{x}(t_{N-2})\right)$$

where $\vec{a}(t_N) = \frac{\left(\vec{u}(t_N) - \vec{u}(t_{N-1})\right)}{\Delta t}$.

If the velocity changes are high then a more sophisticated velocity estimator is required. The Kalman-filter is a recursive linear optimal estimator (Jähne [1997]) which can be used.

The simple estimators are sufficient in most cases. Further improvements, of less computational costs a Kalman-filter would cause, can be obtained with an improved stereoscopic correspondence match (see section 7).

5.2.3.3 PTV post processing

The list of streaks constituting a particles trajectory is already constructed. The final step is to remove 'outlier' streaks from a trajectory. The 'outlier' elements of the trajectory are defined by a smoothness criterion for the trajectory using an interpolation technique. A streak element of a trajectory is considered as an outlier, if the velocity vector of the streaks exceed a certain threshold value from an interpolated value. The PTV algorithm in this work uses an adaptive Gauß-windowing technique[12] proposed by Agüí and Jiminéz [1987] and implemented by Hering

---

[12]Interpolated velocity $\vec{v}(\vec{x}_i)$ for streak number i at location $\vec{x}_i$ and σ the with of the Gauß-Kernel:

$$\vec{v}(\vec{x}_i) = \frac{\sum\limits_{j=1}^{n} \vec{u_j}(\vec{x}_j)\exp\left(-\frac{|\vec{x}_i - \vec{x}_j|}{\sigma^2}\right)}{\sum\limits_{j=1}^{n} \exp\left(-\frac{|\vec{x}_i - \vec{x}_j|}{\sigma^2}\right)}$$

Geometric constraints
location of epipolar lines
geometric similarity
uniqueness
Object properties
compatibility of object features
continuity of disparities
figural continuity
coherence principle
disparity limit
local disparity limit
disparity gradient
spatial order of objects or pixel
temporal order of objects
connectivity of borders

Table 5.1: Stereoscopic constraints.

[1996], or simply polynomial interpolation. A spline interpolation method was described by Spedding and Rignot [1990] which is a more elaborate technique, but without significant enhancement. In addition, the AGW interpolation technique is used for interpolation of the vector flow field on a regular grid.

5.3   Stereo correspondence solving

The problem to be solved for the stereoscopic imaging system is to identify an object uniquely in the stereoscopic views. This is done by solving the *stereo correspondence problem*. Usually the stereoscopic correspondence problem is solved for images of two (or more) different views in a static scene where the objects are not changing. In this work image sequences over a time interval were considered. The 'objects' are trajectories which consist of a list of temporal subsequent ordered streaks.

There is no general method to solve this correspondence problem uniquely. Each method takes a certain amount of constraining assumptions concerning the setup of the cameras and the properties of the observed object such as geometry or movement. The constraints which are relevant to stereo PTV will be discussed in the next sections. Table 5.1 lists some stereoscopic constraints.
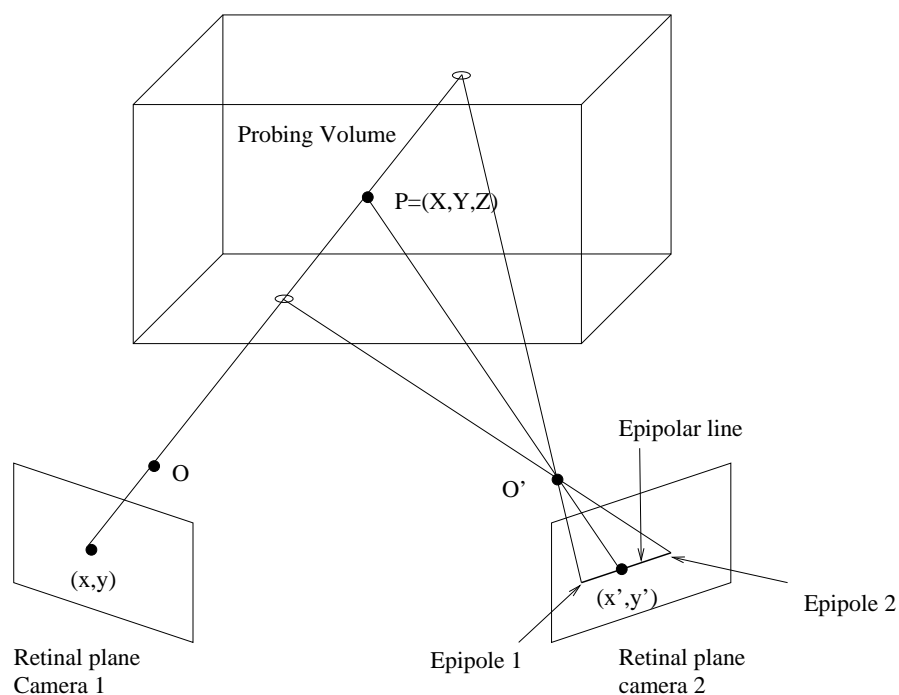
Figure 5.11: Construction of an epipolar line in the retinal plane of camera 2 from an image point (x,y) on the retinal plane of camera 1.

5.3.1 Geometric constraints

The epipolar constraint

The knowledge of the camera arrangement and the geometry of the object - the stereoscopic geometric setup of the system - allows to reduce the correspondence possibilities considerably. The epipolar constraint is derived from the stereoscopic geometry and is one of the strongest constraints which reduces the computational effort significantly.

Figure 5.11 shows the geometry which constitutes the *epipolar line*. The object (point) is located at the world coordinate $P = (X, Y, Z)$ and imaged through the center of the lens O onto the retinal plane of camera 1 to the camera coordinate (x, y). The box marks (symbolically[13]) the probing volume, where this volume is defined as the intersecting common volume of observation for the two cameras and the finite depth range. To find the corresponding point in the retinal plane of camera 2 the geometry states that the point P has to be found on the outgoing ray $\overline{OP}$ of camera 1. This ray is depicted by the camera 2 and called *epipolar line*. The endpoints of the line are called *epipoles* and are the projections of limits of the

---

[13]The real probing volume is constructed from two intersecting cylinders. The cylinders have an angle of the opening of the lens system of each camera.
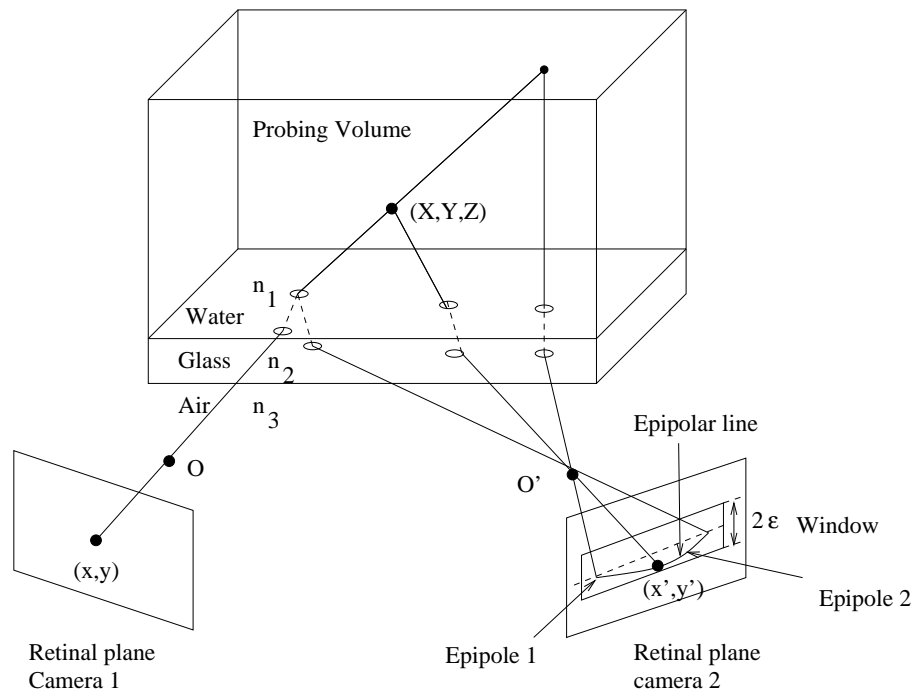
Figure 5.12: Epipolar constraint including multiple media.

probing volume. The *epipolar plane* is given by the plane through the center of the lenses O, O' and object point P - the intersection of the plane with the retinal planes results in the epipolar lines in retinal plane 1 and 2, respectively.

The search of the projected point P in the retinal plane of camera 2 (x', y') is therefore reduced to a single line. In the special case where the optical axes of the cameras are parallel, the epipolar lines match the scan-lines of the cameras. In this case no explicit calculation of the epipolar lines has to be performed and is called *standard-stereo geometry*.

The relevance for the stereoscopic correspondence search is summarized:

- A pixel in the image of retinal plane of camera 1 has to correspond to exactly one pixel in the image of the second camera plane, where the pixel must be found on the epipolar line.

- For a given image point the correspondence search is reduced from a two-dimensional to a one-dimensional problem.

In reality this is not a straight line but curved. This is due to deviations in the optical system and small errors in the camera parameters. Therefore a narrow window of width 2ε takes these deviations into account.

For multiple media geometry the epipolar line is slightly bent as shown in figure 5.12. In practice this deviation from a line and the lens distortions proved to be small enough to be accounted for by the tolerance window of size 2ε, which means the search of point (x', y') on a line is replaced by a search inside an epipolar 'window'.

The reduction of the computational effort can be easily shown by the number of comparisons which have to be performed for each trajectory to find the corresponding trajectory. If the epipolar search area is $A = 2\varepsilon \cdot l$, given by its width 2ε and length l, and the entire area of the image is A_o, the number of possible matches is $n \cdot \frac{A}{A_o}$ where n is the number of correspondence candidates. The number of comparisons which have to be performed for each trajectory is therefore

$$N_1 = K \cdot n \cdot \frac{A}{A_o} + 1$$

where K is a threshold factor (K is the ratio of number of correlating to number of non correlating elements of a trajectory, $K = 4$ as shown in section 5.3.4.2) and one match has to be done in any case with the corresponding trajectories (presupposing no overlap of trajectories). The number of total comparisons is

$$N = n \cdot N_1 = K \cdot \frac{A}{A_o} \cdot n^2 + n \qquad (5.8)$$

which is significantly lower if performing comparisons for all trajectories ($n!$ comparisons).

The geometric similarity constraint

The images of the object in the two retinal planes of the cameras have to be similar. For instance lines need to have a similar orientation and a similar length in both images (considering the geometry of the cameras).

5.3.2 Object properties constraints

Uniqueness constraint

One pixel of image 1 has to correspond to exactly one pixel in the second image - this constraint was already shown for the epipolar constraint.

This is not always given for all the pixels: If two points lie on the same visible ray of camera 1 they are seen as separate points for camera 2. This shows that the *similarity constraint* can suffer from this - a line in image plane 1 can be divided into parts in the second image. Thus the length as contrasted to the orientation of the lines is not a good criterion without special consideration.

Compatibility constraint

Characteristics in the two stereo images correspondent to each other only if they have the same physical cause based in the object of the 3D-world. Characteristics which depend on the viewpoint are rejected. One of this characteristics of an object could be for instance a border line of the object and its orientation or the intensity (grey-value) variation due to illumination. A counterexample is the reflection on the surface of the object, which depends on the point of view and is therefore not a characteristic of the object.

Continuity constraint

The surface of an opaque object is assumed to be continuous almost everywhere - where 'almost everywhere' means excluding the border lines. This implies that for visible points on the surface of the object the distance from a point to the observer and the intensity (grey value) varies continuously.

Figural continuity constraint

This is more strict than the previous continuity constraint. It is not always guaranteed that a region in the stereo images can be identified with an object surface. Therefore the continuity can be restricted to contour lines of the object. The disparities of the object vary continuously along the contours of the object.

Coherence principle

If the shape (3D volume) and physical properties (opacity, transparency etc.) of the object are known, this information can be used to identify the object surfaces. The continuity constraint is a special case of the more general coherence constraint: Local discontinuities in disparity fields may result from a number of superimposed objects (continuous disparity fields) corresponding to a smooth surface. The coherence principle states, that neighboring discontinuities have to be similar in the stereo images if they belong to the same (3D-) object.

Disparity limit

The continuity principle is not very precise in respect to the term *continuity*. Due to discretization and disturbances in the optical system the characteristics do not differ continuously but rather up to a certain threshold value. This threshold value is accounted for by the *disparity limit* which states that the characteristics do not exceed a certain threshold. An example is the grey value (intensity) of an object which can differ in the two images up to a certain threshold. As another example
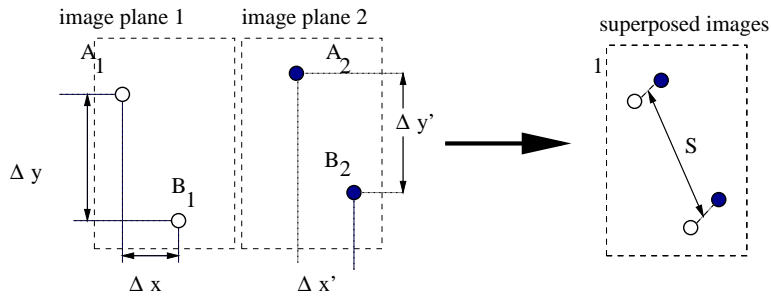
Figure 5.13: Disparity gradient. A_1, B_1 and A_2, B_2 are corresponding points in image plane 1 and 2. The superimposed stereo image is on the right side.

the precision of the matching can differ up to certain limit, if a block matching method is used.

Local disparity limit

The previous *disparity limit* is a global threshold. A more specific threshold is the l*ocal disparity limit* where the threshold is determined in the local vicinity of a pixel point. This means a specific threshold (maximum disparity value) is given for the characteristics of an object.

Disparity gradient limit

The *disparity gradient* is defined by the difference in disparity of neighboring points.

Two neighboring points in image plane 1 and image plane 2 correspond to each other if the *disparity gradient* does not exceed a certain value. The disparity gradient Γ_d is defined as the distance S between the central points on the line of the corresponding points on the superposed image by

$$S = \sqrt{((\Delta x + \Delta x')/2)^2 + ((\Delta y + \Delta y')/2)^2}$$

with

$$\Gamma_d = \left[\begin{array}{c} \Delta x - \Delta x' \\ \Delta y - \Delta y' \end{array} \right] / S$$

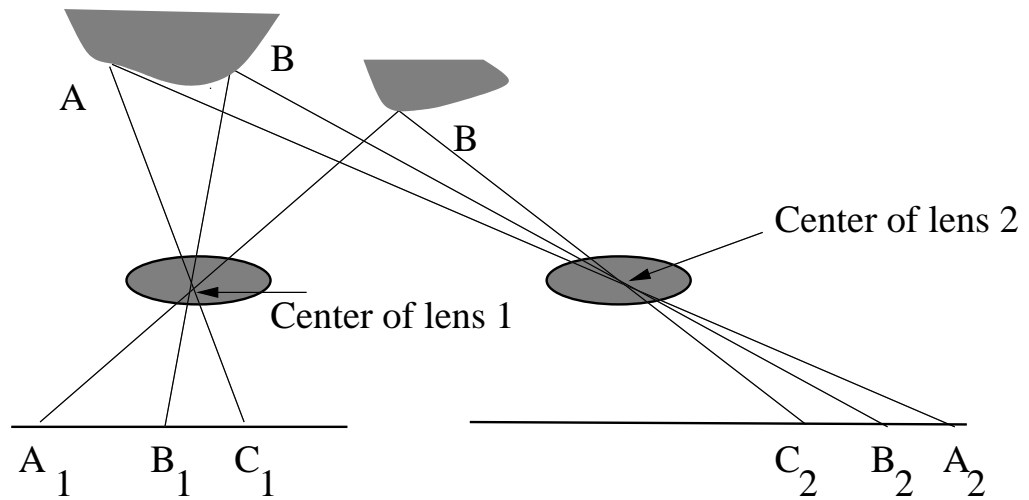The constraint is not satisfied, if $|\Gamma_d|$ exceeds a certain threshold value.

Figure 5.14: Order of the points A, B, C on the epipolar line of image plane 1 is sustained in the corresponding epipolar line on image plane 2.

Ordering constraint

This is a very strong and therefore important constraint which can reduce the computing effort enormously. This constraint has a spatial and a temporal aspect:

- Pixel points located on a epipolar line of the first image plane have to be found on the corresponding epipolar line in the second image plane in *exactly the same order*. If occlusions occur in one of the image planes, the corresponding point is missing in the other plane - but still the order is sustained.

- If there is a temporal information attached to the object, this temporal order has to be sustained in both stereo images (or image sequences).

Connectivity constraint

An object which can be described through connected elements (such as the border of an object described by connected lines or pixels) in the image plane has to be connected in the second image plane. This is often not the case because parts of an object can be hidden in one camera view and visible in the second, or another hidden object can be visible in the second camera view - therefore the *connectivity constraint* is broken.

5.3.3   Applied constraints for 3D PTV

The stereo PTV is based on the classical 2D-PTV. The available information from the 2D-PTV is the following:

- A list of all trajectories,

- where a trajectory consists of a list of streaks which are sorted in chronological order

- and each streak is characterized by

    - a number of the image where it was detected,

    - the area (size in pixels) of the segmented streak

    - and an average grey value in this area.

    - The (sub-pixel precise) position of the streak is determined by the center of mass calculated from the grey-value of the pixels on the detected area of the streak.

From the list of stereoscopic constraints listed in table 5.1, some constraints proved to be important for the 3D-PTV stereo correlation.

In a first step a list of possibly corresponding candidates is constructed. The following constraints are applied to build the correspondence list (index 1 stands for image sequence of camera one, 2 for image sequence of camera two):

- *Ordering constraint: Temporal order*.
  Because each trajectory consists of a list of subsequent, timely ordered streaks, this constraint requires the correspondence of all streaks of a trajectory T_1 of image sequence one with trajectory T_2 of the image sequence two. If only parts of the trajectories correspondent ('holes' in the trajectory), it results in a splitting up in two or more trajectories.

- *Geometric constraint: Epipolar constraint*.
  The corresponding trajectory T_2 to trajectory T_1 was found within the epipolar window of width ε.

- *Object property constraint* (section 5.3.4.2):

    - If the relation of correlating to non correlating streaks of trajectories T_1 and T_2 exceeds a threshold, the trajectory is considered as not corresponding.

– If the two trajectories T_1 and T_2 correspond to each other, the distance d between the streaks varies solely within the epipolar window of size ε and is roughly the same for all streaks. If T_1 and T_2 move relative to each other, d is proportional to this relative motion and T_1 and T_2 therefore do not correspond.

The ordering (temporal) and the geometric (epipolar) constraints are the strongest constraints. Depending on particle densities these two constraints may suffice to allow a unique solution of the correspondence problem. This may not always be the case as high particle densities are beneficial for high spatial resolutions in visualizing flows.

5.3.4   Stereo correlation algorithm

The purpose of the stereo correlation is to find corresponding trajectories in the two image sequences ($1 \, and \, 2$). A list of correlating trajectories (from 2D-PTV) is constructed and from this list the 3D (world-) coordinates can be readily calculated (see section 5.9).

The two strongest constraints are considered at the begin. The first step is to find the correspondence from the geometric (i.e. epipolar) constraint. The next step is to apply the ordering constraint in the time domain (section 5.3.4.1). If the correspondence is not resolved, further constraints are applied (section 5.3.4.2).

5.3.4.1   Application of the geometric and ordering constraint

There are four possible outcomes of the correspondence search:

1. *No correspondence*:
   This is the trivial case where to a trajectory T_1 in the retinal plane of camera one no corresponding trajectory in the retinal plane of camera two was found.

2. *One-to-one correspondence* (figure 5.15):
   Exactly one trajectory T_2 was found as correlating to trajectory T_1.

3. *One-to-many correspondence* (figure 5.16 a and 5.16 b):
   For the trajectory T_1 two or more trajectories $T_{2,i}$ ($i = 1 \ldots n$, a number of n trajectories) were found which in turn correspond to trajectory T_1.

4. *Many-to-many correspondence* (figure 5.17):
   A multiple of trajectories $T_{2,i}$ were found for trajectory $T_{1,1}$ whereby $T_{2,i}$ corresponds to multiple trajectories $T_{1,i}$.
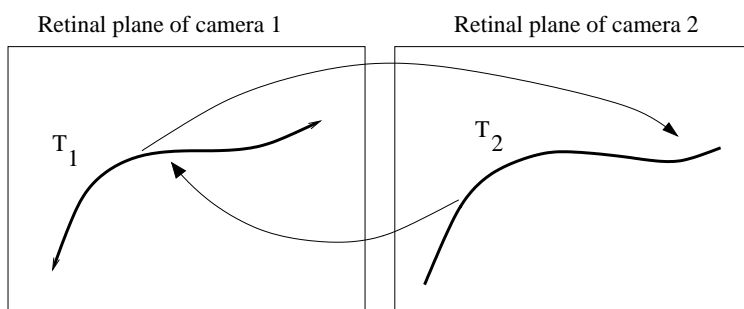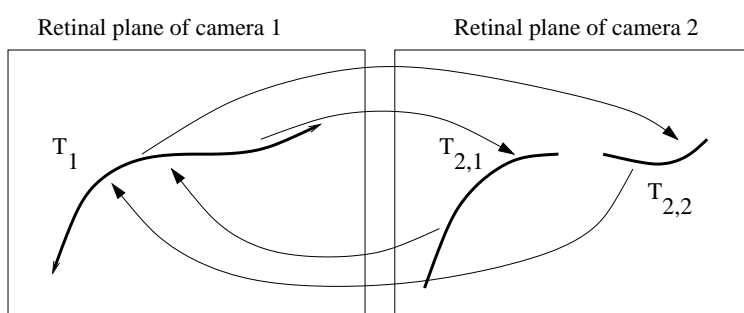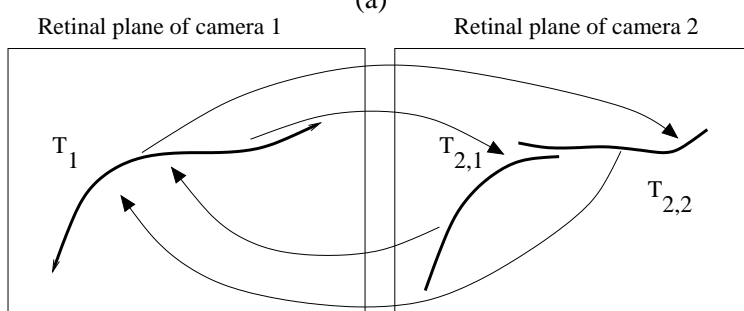
Figure 5.15: One-to-one correlation.

(a)

(b)

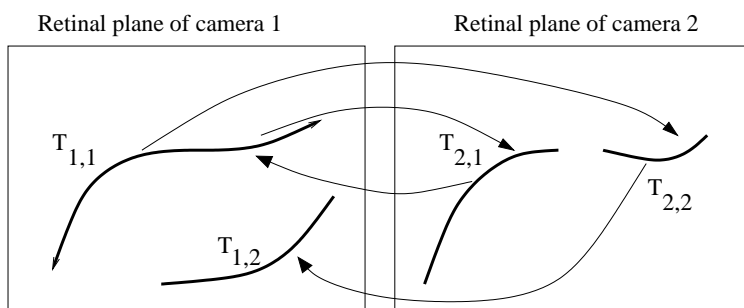Figure 5.16: One-to-many correlation (a), (b) with temporal overlap.

Figure 5.17: Many-to-many correlation.

A reason for non corresponding trajectories (case 1) could be if a particle trajectory is imaged by one camera only and if it is out of the image plane of the second camera. To minimize this occurrence, the intersecting volume (volume of observation) of the two cameras has to be maximized. Furthermore an imprecise calibration (especially in the outer regions of the image) might fail the correspondence match. Another reason could be an incorrect segmentation of a trajectory. This can be caused by grey-value of the streaks being to small due to restricted illumination or if the particle (streak) is out of focus.

Therefore a homogeneous illumination, a maximum of the observation volume and of the depth of field, and a good calibration are crucial for obtaining a high number of correspondence matches.

For case 2 (figure 5.15) a unique correspondence is found and the world coordinates can be reconstructed.

With increasing particle density the probability of crossing trajectories and therefore failing correspondences increases. In this case *the one-to-many* and the *many-to-many* correspondence search increases the number of corresponding trajectories.

For case 3 (figure 5.16) two distinct outcomes occur:

The first (figure 5.16 a) one occurs if the trajectory T_1 has a multiple of corresponding trajectories $T_{2,i}$ which do not overlap in time. This may happen if streaks were not segmented correctly over the whole time interval of T_1. The resulting trajectory $T_{2,i}$ is thus generated by the same particle and it corresponds therefore to T_1.

The second outcome (figure 5.16 b) occurs if there is a temporal overlap of $T_{2,i}$ which are found as corresponding to T_1 from the geometric constraint. This violates the boundary condition that trajectories (and the streaks) have to be unique. Therefore they must belong to n different particles and their related trajectories: $T_{2,i} \longrightarrow T_2, T_3 \ldots T_n$.

For case 4 (figure 5.17) multiple trajectories $T_{2,i}$ were found for T_1, where $T_{2,i}$ in turn correspond to different trajectories $T_{1,j}$. In this case further criteria for resolving these ambiguities are required.

5.3.4.2 Object property constraint

A strong constraint in resolving the remaining ambiguities is the uniqueness constraint. This constraint states that an object point viewed in the first image should not match more than one image point in the other view. This constraint does not hold for transparent objects exceeding a certain size. A bubble or hollow glass sphere (in water) can be viewed as a single image point in one view and, due to reflections, as two image points in the second view. Therefore the shape has to be modeled in order to resolve the ambiguities.

In flow visualization small and rotationally symmetric particles are frequently used (10 to $500\,\mu m$). The particles may thus be viewed as point objects and the uniqueness constraint can be applied. Two criteria are applied for the 3D-PTV:

- The trajectory T_k is constructed from the streaks $S_{k,i}$. Even if not all streaks of the first image sequence $S_{1,i}$ of trajectory T_1 correlate to streaks $S_{2,j}$ of trajectory T_2 from the second image sequence, they may nevertheless be corresponding. This is accounted for by a heuristic threshold value K that is determined by the ratio of the number of correlated streaks k to the non correlated streaks n. If the trajectory T_1 consists of streaks $S_{1,i}$, $i = 1 \ldots I$, and the corresponding trajectory T_2 consists of streaks $S_{2,j}$, $j = 1 \ldots J$, then the number of correlated streaks k are given by $k = min(I, J)$. Therefore the threshold K is written as

$$K = \frac{min(I,J)}{|I - J|}$$

- Even if the streaks of trajectories T_1 and T_2 are found within the epipolar windows (of size ε), T_1 and T_2 do not correspond if the particle streaks are moving relative to each other. Thus a criterion to resolve this ambiguity is of a statistical nature taking the distance between each other as a matching criterion (figure 5.18). The standard deviation σ_d is a criterion to distinguish between crossing and non crossing trajectories; in the case of crossing trajectories σ_d is larger than in the case of non crossing ones. The standard deviation is written as:

$$\sigma_d = \sqrt{\frac{\sum \Delta \vec{x}_i - \left(\sum \overrightarrow{\Delta x_i} \right)^2}{N(N-1)}}$$

where $\overrightarrow{\Delta x_i}$ is the distance between the trajectories (perpendicular lines in figure 5.18), $i = 1 \ldots N$ for N the number of points (streaks). A threshold value of $\sigma_d = 0.5$ pixels was found to be suitable (Netsch [1995]). If the threshold value σ_d is exceeded, the trajectories show a relative motion towards each other and do thus not correspond.

5.3.5 Stereo coordinate reconstruction

The stereo reconstruction requires at least two perspective views different from each other or a model of the scene. The reconstruction methods of a stereoscopic object from two-dimensional images of the object is called *triangulation*[14]. There are several common stereo triangulation methods available (Schwarte et al. [1999]):

---

[14]Definition *triangulation*: Determination of an unknown visual point (in world coordinates) within a triangle of the optical basis (O, O') and the related lateral angle pointing to the unknown point.
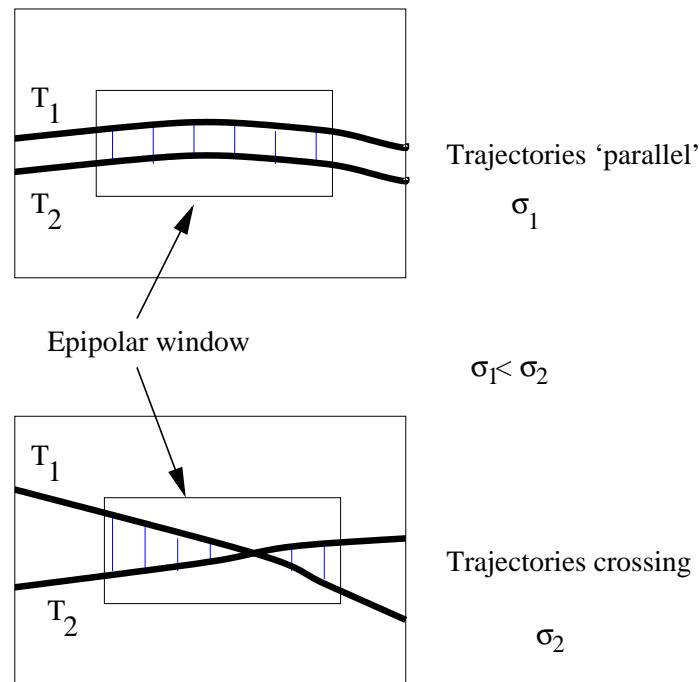
Figure 5.18: Rejecting 'false' correspondences of two crossing trajectories T_1 and T_2.

- *Shape from shading:*
  This method requires the knowledge of the light source (light intensity distribution) and the reflectance properties of the object surface but needs only one image to reconstruct the object. The local steepness of the object surface is taken to reconstruct the surface shape. The steepness is determined by the intensity (grey-value) of each pixel.

- Focus techniques:

  - Confocal microscopy: The CCD-sensor detects only illuminated points at the focal (X,Y) plane. The third dimension is obtained by scanning the depth (Z)

  - Depth from focus: A single, two dimensional image is taken from the object. The center of the object (X,Y) is taken from the grey-value center (multiplied by the magnification of the optics). The depth distance (Z) of the object can be inferred from the defocus.

- Active triangulation: The light source projects a light intensity structure (by a light beam scanner, a light sheet or a mask with a certain structure) onto the object. With the knowledge of the angle of the light projecting optics, the projected intensity pattern and the angle of the receiving optics of the

CCD, the depth map of the object can readily be calculated. A light intensity which varies in time and space according to a certain pattern can increase the resolution (Wolf [1996]).

- Passive triangulation: Contrary to the active triangulation method this method does not consider the geometrical arrangement of the illumination. Different views of the object are required to determine its 3D position. This can be achieved either by using multiple cameras (*static stereo analysis*), by using a moving camera and taking images in several positions or by tracking a moving object (*structure from motion*). The positions of the cameras have to be known (calibrated) or self-calibrating methods have to be used.

The purpose of the stereo coordinate reconstruction is to obtain the real, physical location of the object in the world coordinates $\overrightarrow{X}$, the so called *triangulation*. The simplest triangulation method in static stereo analysis (figure 5.19, for details see Klette et al. [1996]) considers only the projective transform P (equation (4.1)). The *disparity* of the correlating object points is given by the distance between the correlating object points $\overrightarrow{d}$ in the superimposed images of the two cameras (figure 5.19). The image coordinates $\overrightarrow{x}$ and $\overrightarrow{x}'$ in the retinal planes of camera 1 and camera 2 are known.

The disparity is defined as

$$\overrightarrow{d} = \overrightarrow{x} - \overrightarrow{x}'$$

with

$$\overrightarrow{d} = \begin{pmatrix} d_1 \\ d_2 \end{pmatrix}, \quad \overrightarrow{x} = \begin{pmatrix} x_1 \\ x_2 \end{pmatrix}, \quad \overrightarrow{x}' = \begin{pmatrix} x_1' \\ x_2' \end{pmatrix}.$$

Using the projective transform P :

$$\overrightarrow{x} = \begin{pmatrix} x_1 \\ x_2 \end{pmatrix} = -\frac{f}{X_3} \begin{pmatrix} X_1 \\ X_2 \end{pmatrix} \tag{5.9}$$

where f is the camera constant (for both cameras).

The baseline distance ($\overline{OO'}$) $\overrightarrow{b} = \begin{pmatrix} b_1 \\ b_2 \\ b_3 \end{pmatrix}$ is given by the distance of the center of the lenses.

The equation system (5.9) can be solved:

$$X_3 = f\frac{X_1}{x_1} = f\frac{(X_1 + b_1)}{x_1'}$$

$\Leftrightarrow$

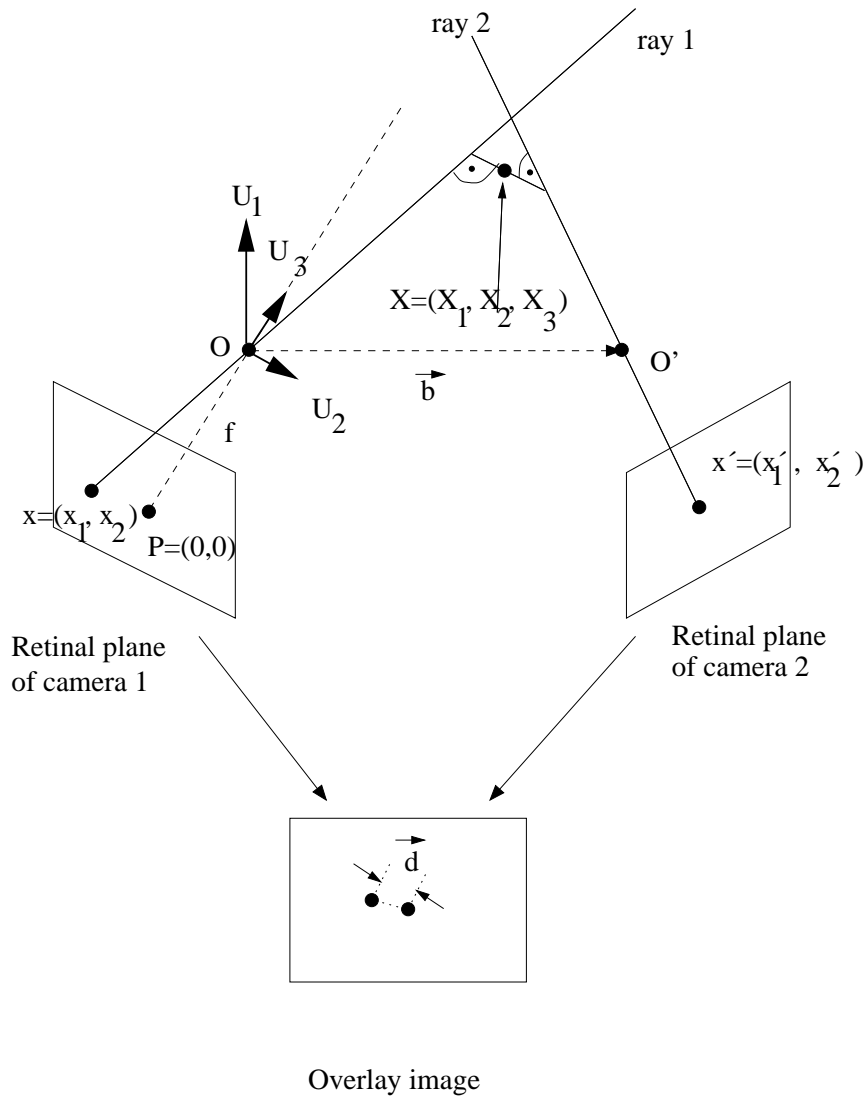$$X_1\left(\frac{1}{x_1} - \frac{1}{x_1'}\right) = \frac{b_1}{x_1'}$$

Overlay image

Figure 5.19: Stereo reconstruction. The disparity $\vec{d}$ is illustrated in the bottom of the figure.

$\Leftrightarrow$

$$X_1 = \frac{x_1}{(x_1' - x_1)} b_1$$

$\Leftrightarrow$

$$X_1 = \frac{x_1}{d_1} b_1$$

and the same with

$$X_2 = \frac{x_2}{d_2} b_2$$

$$X_3 = \frac{f}{d_1} b_1.$$

If the world point $\overrightarrow{X}$ is close to the cameras the disparity $\overrightarrow{d}$ is large and the camera coordinates can be determined relatively precise compared to the case where $\overrightarrow{X}$ is further away from the cameras.

A more sophisticated and more precise method uses the complete camera model.

If the camera parameters are known (section 4.1) and the stereo correlation problem is solved (section 5.3), the 3D world coordinates can be determined. For this purpose the camera model has to be inverted. In the case of the pinhole camera transform $F = B \cdot R \cdot T$ (equation (4.7)) the inverse transform is

$$U = F^{-1} u = T^{-1} R^{-1} B^{-1} u.$$

The function to be minimized is:

$$|u - F(U)|_{Z=Z_o} \to \min \tag{5.10}$$

where U is the coordinate of the object in homogeneous coordinates ($U \in \mathbb{R}^4$), u the image coordinate in homogeneous coordinates and F the transform matrix of the camera model. As the function to be minimized is convex[15], a method based on conjugate gradient minimization, the *Powell's method* (Vetterling et al. [1992]) which rapidly converges, is used.

The solution is not unique in the physical space because the equation is written in homogeneous coordinates which are determined up to a scaling factor λ (section 4.2.1)

$$F^{\cdot -1} : \{U = (U_1, U_2, U_3, 1)^T \varepsilon \mathbb{R}^4\} \to \{u = (u_1, u_2, 1)^T \varepsilon \mathbb{R}^4\}.$$

---

[15]No local minima exist.

This means, the solution in the physical space is an optical ray. This procedure is applied to the coordinate points of the first and second camera image plane. Ideally the two rays intersect and the intersection point is the world point U sought-after. In praxis the two rays do not intersect due to noise and deviations in the camera parameters. The simplest way is to take the middle of the distance of the two rays. If the distance between the two rays is small compared to the distance between the image plane and the object plane this method is sufficiently precise. For uncalibrated cameras there are several methods better suited to find the best match for the object point U (see Schwarte et al. [1999]).

Chapter 6

Analysis of data and discussion of results

Results of the stereo particle tracking velocimetry (stereo PTV) are shown and discussed in section 6.3. It contains experimental investigations of flow fields in a gas-liquid reactor and investigations of flow field visualization and analysis in wind-wave flumes. The main interest of this work is the influence of wind induced waves on the liquid flow field. Since the large AEOLOTRON wind-wave facility was in the scope of this work newly constructed, the investigations served to validate the conditions and to test the new experimental and analysis methods.

For quantitative results the quality of the calibration and the accuracy and resolution of the used methods is essential and discussed in section 6.1. Since the stereo correlation method is a fundamental part of the stereo PTV, the limits and capabilities of the stereo correlation are summarized in section 6.2.

6.1 Calibration and resolution

To obtain quantitative results in digital image processing the calibration procedure is an essential part of the measuring procedure and evaluation. It consist of several parts: The 2D calibration as described in section 5.1 and the camera calibration for the stereo setup as discussed in section 4.2.5. The calibration data obtained from the 2D calibration are required for the camera calibration. Therefore the precision of the 2D calibration is crucial.

The 2D calibration procedure finds the line crossings with a precision of 1/10 up to 1/100 of a pixel, depending on the manufacturing precision of the calibration target and the distortions due to the lens system and CCD sensor. Extensive studies on the dependency of noise added to the calibration points on the camera parameters have been reported in a diploma thesis of Garbe [1998]. If the nonlinear distortion
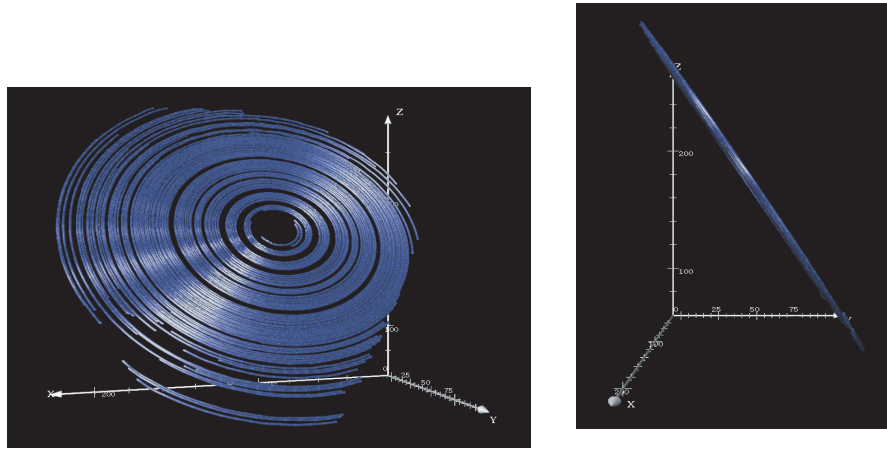
Figure 6.1: A rotating grid as a calibration target to validate the calibration algorithm, measured by Garbe [1998]. The display software was developed by Bentele [1998]. The 'missing area' of the rotating disc is caused by the limited volume of intersection of the two cameras.

parameters are small (in the order of 10^{-5}), the deviation of the camera parameters increases linearly with noise level (normal distribution) added to the calibration points. The linear behavior is a consequence of the camera model of small linear distortions. The error also decreases with $\sqrt{n}$ where n is the number of calibration points.

Furthermore the dependency of the deviation of reconstructed 3D world coordinates $X = (x_1, x_2, x_3)$ on the deviation of the calibration points is of interest. The grid points lie in the x_1, x_2-plane. The deviation of the x_3 component of the world point is found to be about three times larger than the deviation of the x_1 and x_2 component. The dependency of the deviation of the world coordinates on the deviation of the calibration points is linear. The same linear dependency is found for the deviation in the internal and external camera parameters. However, its dependency on the internal parameters is by a factor of the order 10^8 larger than the dependency on the external parameters. The precise determination of the internal parameters is therefore much more important than the precision of the external camera parameters.

For the validation of the stereo PTV algorithm a rotating grid (with an inclination angle of $27.8°$ toward the z-axis) was used. Figure 6.1 shows qualitatively the result - all the trajectories are within a plane and the movement of the grid points is circular. Taking the given radial velocity the deviation of the measured velocity can be determined and was found to be less than 5%. The average displacement error of the grid points is calculated from the standard deviation of each trajectory and amounts to 3%.

If a Scheimpflug camera setup is chosen, the optimal angle for the best suited depth
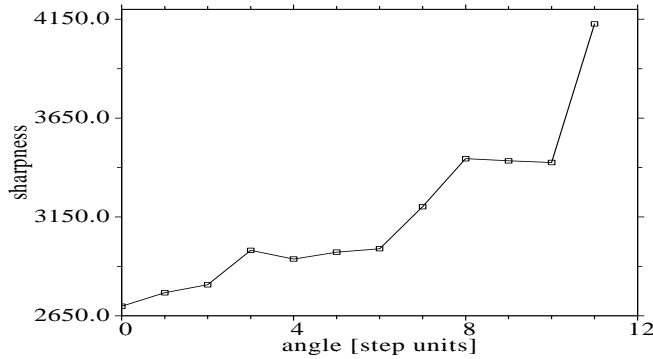
Figure 6.2: The sharpness measure is defined as the variance over the whole image area for each adjusted angle (for details see text).

of field (see section C) has to be found. This is accomplished by shifting the angle stepwise and determining for each step a sharpness measure (calculated from the global variance of the image). The used lens system included three degrees of freedom (distance between lens). It turned out that a one degree of freedom lens system would be much better for calibration. The dependency of the depth of field (as determined by the sharpness measure) is shown in figure 6.2.

6.2   Stereo correspondence

The resolution of ambiguities in the correspondence search proved to be a critical point in respect to the particle density. For low particle density (<200 particles) most ambiguities can be resolved. The number of unresolvable ambiguities increases with the density of particles. It is therefore not possible just to increase the spatial resolution by increasing the density of particles. The same argument applies for the 2D-particle tracking velocimetry (PTV). Because the stereo correspondence is based on the 2D-PTV, it is important to know the range of particle density where the 2D-PTV fails.

To test the stereo correspondence search the system can be simulated. The model should be simple but close to real conditions. As the physical model the linearized wave theory was taken (see section B).

The two dimensional velocity field $\vec{u} = \begin{pmatrix} u \\ w \end{pmatrix}$ of a surface water wave in the linearized wave theory is written in two dimensions as

$$
\begin{aligned}
u(t,z) &= A\,\omega e^{kz}\cos(kx - \omega t) + u_o(z) \\
w(t,z) &= A\,\omega e^{kz}\sin(kx - \omega t)
\end{aligned}
\tag{6.1}
$$

where A is the amplitude, ω the frequency and k the wave number. This model

ideal PTV		
ε	S_k	$K = S_n/S_k$
8	1100	0.5
4	1500	0.4
2	>1900	0.13
real PTV		
8	800	1.0
4	1200	0.7
2	>1750	0.3

Table 6.1: Stereo correlation simulation according to Netsch [1995]. Ratio of corresponding trajectories S_k to the number of multiple corresponding (unresolved ambiguities) trajectories S_n as a function of the epipolar window size ε and S_k for 'ideal' and 'real' PTV (see text for details). For $\varepsilon=2$ the limit of the algorithm is not yet achieved.

describes orbital particle paths (equation (B.8)) of frequency ω decaying exponentially in amplitude with depth z ($z = 0$ at the surface, z becoming negative with increase in water depth). A surface drift velocity $u_o(z)$ is added as a linear component to the horizontal velocity u.

The simulation is done in the following way: The particles are randomly placed in the volume of observation and moving according to equation (6.1). At each time step (time of exposure) the particle (of a Gauß function shape) movement is projected on the two image planes and stored. The particle is imaged as a streak and its grey-value obeys the continuity of optical flow (slow movement means a large grey-value and a small streak, fast movement a small grey-value and a large streak). If the streaks overlap in the image plane, the trajectory is divided into different parts. Therefore the number of trajectories in the 2D-plane is larger than the number of actual trajectories.

Extensive simulation studies using the described model have been done by Netsch [1995] and are summarized in the following. The applied camera model is the pinhole camera (section 4.2.3) where the translational method camera setup was used (figure 3.13(a)).

The *efficiency* of the stereo correlation algorithm is determined by the *ratio* $K = S_n/S_k$ of the number of corresponding trajectories S_k to the number of multiple corresponding (unresolved ambiguities) trajectories S_n, and by the *computational costs* given by the number of trajectory comparisons. The simulation is a sequence of 40 images and the depth range z is 5cm. Two cases are considered, first the *ideal PTV* where the 2D-trajectories have the same length as the generated trajectories and second the *real PTV* where the 2D-trajectories are interrupted (by a probability of 36%). The results are shown in table 6.1.

With a decreasing epipolar window size ε the ratio K is decreasing (more cor-

respondences found) for a given S_k. In the case of the real PTV ratio K is significantly lower as compared to the ideal PTV. This is due to the devision of the trajectories in real PTV and the reduced average length of the trajectories because of interruptions.

The computational costs are decreasing with a reduction of the epipolar window size ε (this is a consequence of equation (5.8)). The number of comparisons does not depend on ε.

Increasing the depth z (volume) improves K due to a smaller density of particles, but for the same density of particles K does not differ significantly.

The quality of the 2D-PTV and the choice of the epipolar window size ε turned out to be important for the quality of the stereo correlation algorithm.
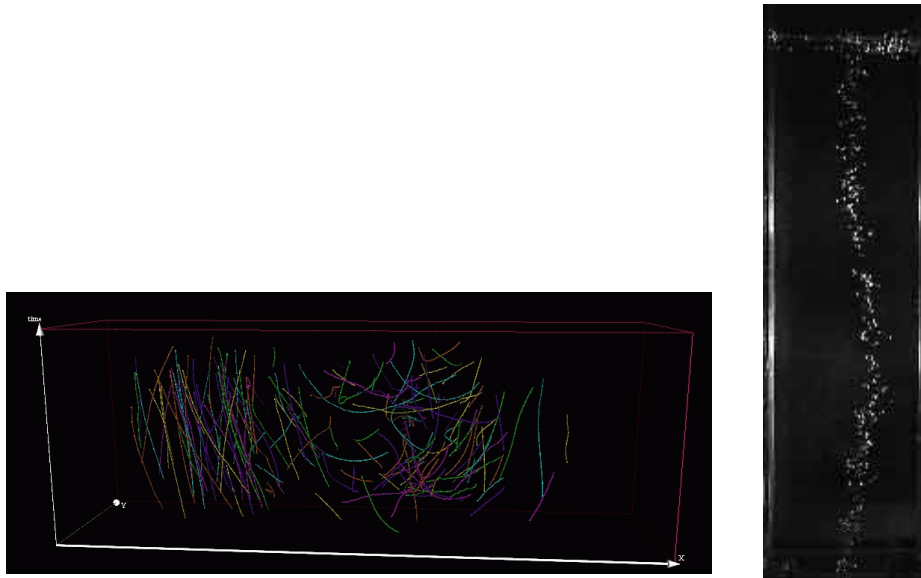
Figure 6.3: The stereo PTV algorithm applied for a gas-liquid reactor (bubble column) at the BASF AG (from diploma thesis of Stöhr [1998]). Left: Fluid trajectories of seeding particles with aeration on the right side. Right: Aeration of the bubble column with ascending bubbles in the liquid.

6.3   Stereo particle tracking velocimetry

The stereo PTV was developed and optimized to operate for flow field measurements. It was applied for investigations in a gas-liquid reactor bubble column where the movement of the ascending bubbles was obtained as their trajectories. Here the main interest was flow field investigations in wind-wave flumes. The stereo PTV was applied in the Heidelberg wind-wave facility for the first time (Engelmann et al. [1998], Engelmann et al. [1999a]). This facility is now dismantled and replaced by a roughly three times larger wind-wave facility (AEOLOTRON) at the Institute of environmental Physics, Heidelberg. Preliminary measurements have been performed in the new facility. Experiences from the previous facility have lead to several improvements for the camera setup (section 3.3.3) for the visualization techniques (illumination and seeding particles/hydrogen bubbles, see sections 3.2.2 and 3.2.1) and for the experimental arrangement. These improvements were included into the new setup. Data processing methods have been developed and applied for the PTV by several authors (see for instance Hering [1996]) and are well established. Since the stereo PTV is a new method, it has been extended to three dimensions, but further techniques concerning the 3D data processing can be applied for image processing of the stereo flow field evaluations.
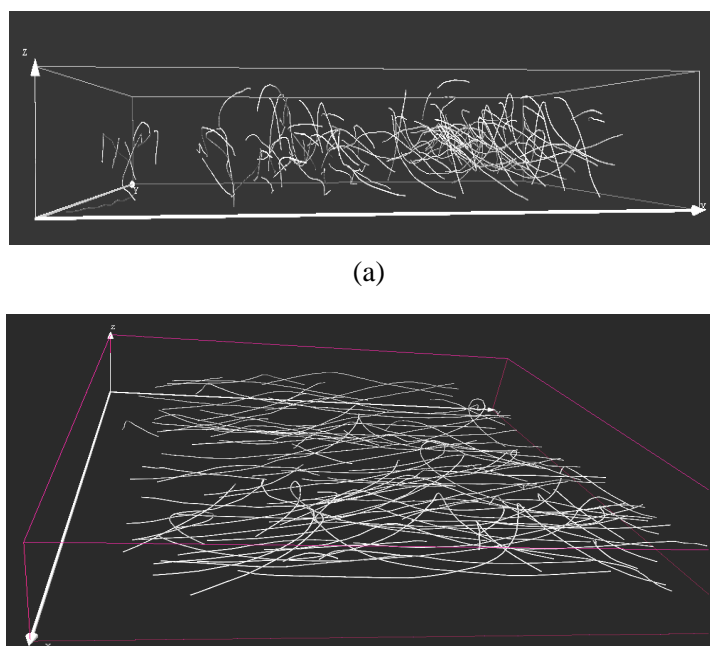
(a)

Figure 6.4: Three dimensional trajectories visualizing the flow as measured at the Heidelberg wind/wave facility in two different perspectives: (a) Perpendicular to the water surface (top) and parallel to the main direction of the flow (left, horizontal); (b) perpendicular to the main direction of flow and in a slight angle to the water surface.

The stereo PTV algorithm applied for investigations in a gas-liquid reactor (bubble column) at the BASF AG is shown in figure 6.3 (Stöhr [1998]). Flow properties in different aeration states were examined. The trajectories of air bubbles and the trajectories of seeding particles (representing the liquid flow) were obtained separately by using different color spectra of seeding particles and air bubbles. The air bubbles in 6.3 ascend in the liquid tank. If the aeration is on the left side of the tank, the liquid flow is rather uniform in the z-direction on the left side and more turbulent on the opposite side in descending z-direction. The results were in good agreement with LDA and ultrasonic flow measurements.

First stereo PTV investigations have been performed at the Heidelberg wind-wave facility. Figure 6.4 shows the 3D trajectory of seeding particles ($(30 \pm 15)\,\mu$m diameter) representing the Lagrange flow field beneath a free wind-driven wavy water surface. The sequence of 500 images covers a time interval of 8.3s. The spirally shaped trajectories show the orbital motion of 'fluid elements' where the waves amplitude was less than 5mm and of little steepness (<5%).

After the Heidelberg wind/wave facility was dismantled and substituted by the large Heidelberg wind/wave facility (AEOLOTRON), first stereo PTV measure-
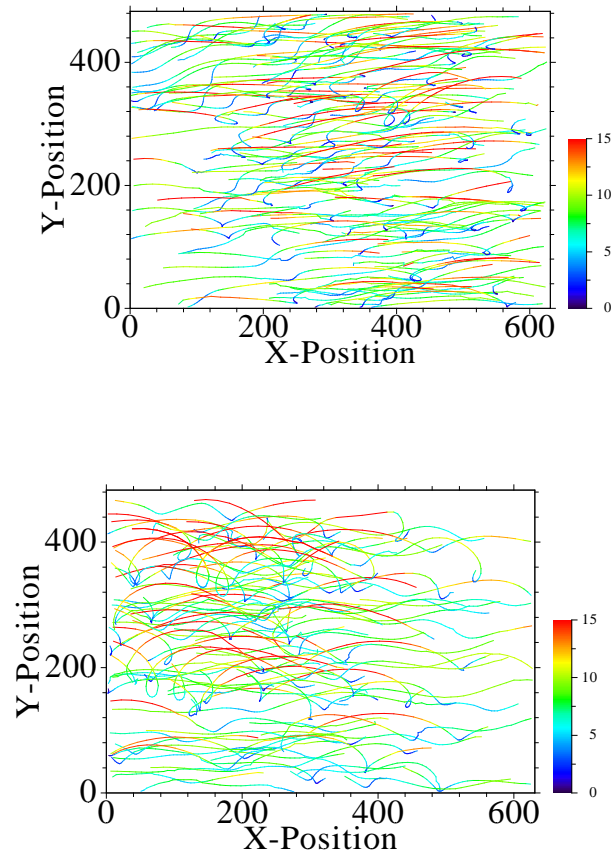
Figure 6.5: Trajectory image of camera one (top) and two (bottom). The velocity is coded in colors from 0-15 pixels/Δt, where the frame rate Δt is 1/60s.

ments were carried out with the experimental setup described in section 3.3.2.2. The results are shown and discussed in the following.

A sample of trajectories from the image sequence of camera one and camera two is shown in figure 6.5. The arrangement of the cameras is according to figure 3.7 and 3.8 in an angle of about $27°$ from the inner (camera one) and the outer (camera two) side from the walls towards the top of the water surface. The trajectory image differs from the classical two dimensional PTV: Here an extended volume of about $80 \times 80 \times 50\,mm^3$ (X,Y and Z coordinates where Z is perpendicular to the -still- water surface) was used instead of a light sheet of about $10\,mm$ thickness (X-direction).

As tracer 'particles' hydrogen and oxygen bubbles were used (section 3.2.2) which implies the buoyancy velocity as the upward velocity of the bubbles (section 3.2.1.2). The buoyancy velocity $u_{p\infty}$ and the associated time constant τ is related to the

Medium	H_2O	
Tracer	H_2	O_2
$\rho(20°C)$	$8.99 \cdot 10^{-2}$ kg/m^3	1.4289 kg/m^3
$u_{p\infty}/d^2$	$5.5174 \cdot 10^4$ 1/sm	$5.5100 \cdot 10^4$ 1/sm
τ/d^2	$2.759 \cdot 10^4$ s/m^2	$2.767 \cdot 10^4$ s/m^2

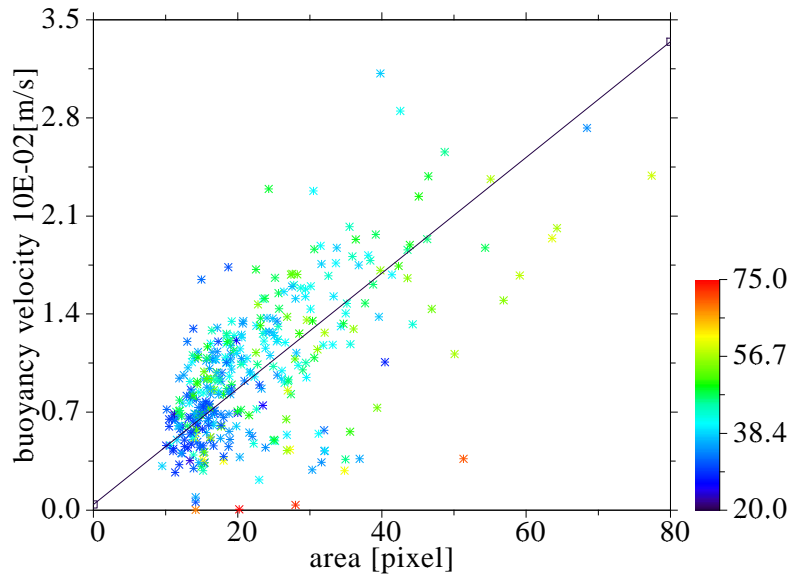Table 6.2: Buoyancy velocity and time constant for hydrogen bubbles in water.

Figure 6.6: Buoyancy velocity as a function of size (area in pixel). The color represents the grey value. Some 'outliers' or other moving particles (dirt) can be identified (and neglected) by the grey value (red marks).

square diameter d^2, listed in table 6.2 and is determined by equations (3.16) and (3.14). The time constant is determined from the velocity $u_p = u_{p\infty}(1 - e^{-t/\tau})$ at $t = \tau$, which is less then $3\,ms$ for an upper limit diameter of $100\,\mu m$. This means, velocity $u_{p\infty}$ is almost immediately achieved (within millimeters of movement).

The buoyancy velocity $u_{p\infty}$ is, according to equation (3.16), a function of the diameter d with $u_{p\infty} \sim d^2$, where d^2 is the size of the particle which is imaged on the CCD as an area of pixels. Figure 6.6 shows the dependency and the solid line is the linear regression of equation (3.16). The area of the imaged bubbles depends on their velocities and is generally not imaged as a circular object but as a streak (figure 5.4). Because of the small buoyancy velocity range of the bubbles (figure 6.6) the streak form can be neglected. The dependency of the buoyancy velocity on the size (imaged area in pixels) is shown in figure 6.6. The mean velocity (z-velocity component) is 0.013 m/s $\pm 50\%$. The mean area is 23$\pm$50% pixels, but the imaged area is much larger than the actual size of the bubbles. Some size calibration would
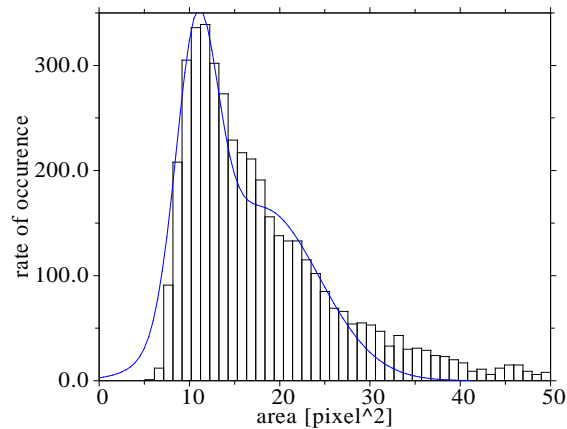
Figure 6.7: Size distribution of bubbles. The solid line is the sum of two normal distributions, representing the H_2 and the O_2 bubbles.

be necessary to determine the real size, but this is not of much interest here. Taking the buoyancy velocity $u_{p\infty}/d^2$ from table 6.2, the (mean) diameter of the bubbles is $50\,\mu$m. This is a quite reasonable size according to Oertel and Oertel [1989], who reported a size range one to two times the size of the diameter of the used wire.

The size distribution from figure 6.6 is shown in figure 6.7. The mean size is $23\pm50\%$ where the distribution shows two peaks at 12.5 and 21.9 pixels. This distribution is approximated by two superposed normal distributions (blue, solid line in figure 6.7) and can be associated with the two bubble types (H_2 and O_2) which show a different rate of occurrence, where O_2 has a larger mean bubble size.

The size distribution in the AEOLOTRON wind-wave flume is shown in figure 6.8. The small inset in this figure shows the 'pollution' with dirt which appears in the images as 'particles'. The behavior of this 'pollution' is different from the bubbles as can be seen in the deviation of bubbles (see tables in section A).

The conditions for the stereo PTV flow measurements are listed in section A. At this time, only qualitative conditions could be adjusted. Devices such as the wind velocity measuring devices were not yet installed. Basically two conditions were of interest: A wave field with wind stress and a wave field without wind stress, where in both cases the wave amplitudes are less than 1 cm. The wave field without wind stress was obtained from the decaying wave field from the previously generated wind waves. The volume of observation was about 30 mm in z-direction and had an extend of 100×100 mm^2 in the x,y-plane.

Figure 6.9 shows 3D-trajectories of a wave field without wind stress. The velocity is represented in colors from 0.3 m/s to 1.2 m/s. The same view as in figure 6.9 is shown in figure 6.10, but now the time is represented in color. In this way the character of the trajectories changing with time can easily be distinguished.
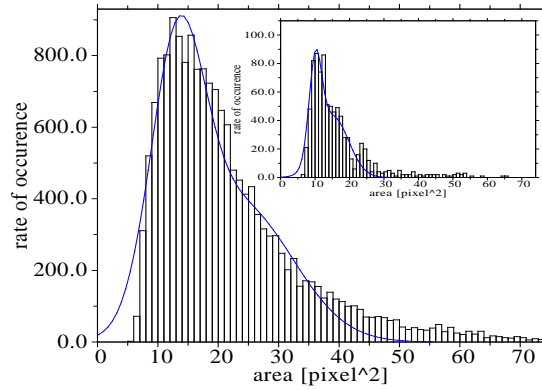
Figure 6.8: Bubble size distribution from the AEOLOTRON wind-wave flume. Partly H_2 and O_2 bubbles, partly pollution by 'dirt' (inset).

The analysis of the velocity components in x,y and z- direction is shown in figure 6.11. The dominating frequency in all velocity components is $(1.4 \pm 0.1)\,\text{Hz}$ where a superposed frequency is $(0.25 \pm 0.05)\,\text{Hz}$. In section A the properties of different series of measurements are tabulated. The low frequency component $(0.25 \pm 0.05)\,\text{Hz}$ is found in the same range for all series (with and without wind stress), and are most probably related to a resonant frequency due to the circular shape of the channel. If the decay of the wave field is progressing and therefore the average wave amplitude decreasing (wind generation off), the frequency is slightly increasing (qualitatively from 1.4 Hz to 1.8 Hz). In all conditions with wind stress the main frequency (for all velocity components) is in the range from 2.1 Hz to 2.5 Hz and is roughly 3/2 higher than without wind stress.

Due to the buoyancy the z-component w is slightly positive and the component in the wind direction (along wind) is the main flow component u (x-direction). It shifts the oscillation to the negative mean velocity. The w-component (cross wind direction) is significantly smaller and oscillates around zero. The phase shift of u and w are nearly 90 degrees - which is a characteristic orbital (circular) movement of fluid 'elements' and the velocity components v and w are almost in phase. It will be discussed in more detail later.

The particle tracking velocimetry allows to obtain the trajectories (paths) of the particles $\vec{x} = \vec{x}(\vec{x}_o, t - t_o)$ and the velocity $\vec{u}(\vec{x}_o, t - t_o)$ (section 2.1). The Lagrange-representation can be transformed to the Euler-representation of the flow field (equation (2.3)), but the Lagrange-representation can generally not be calculated from the Euler-vector field. This is one of the advantages of the PTV method. An example is the orbital movement of 'fluid elements' which can be analyzed only from the trajectories of the seeding particles or bubbles. Properties such as the penetration depth of gravitational waves, determined by the curvature K_{x_i, x_j} (or
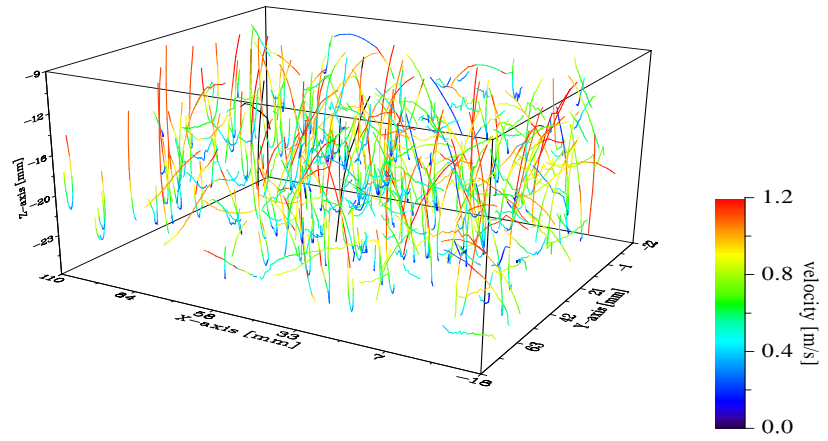
(a)
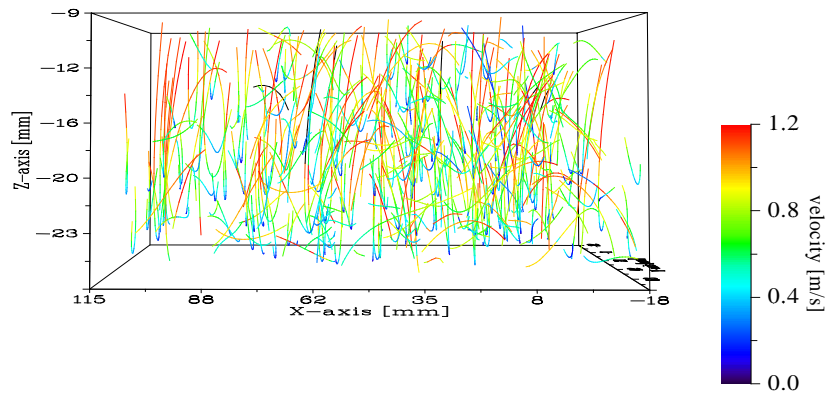
(b)

Figure 6.9: Stereo trajectories of a 'wavy surface' state from lateral view (a) and the 'classical' 2-D PTV view in the x,z-plane (flow direction is x). The view from the upper top is show in (b). The wave amplitude is partly higher than the volume of observation (3cm height).
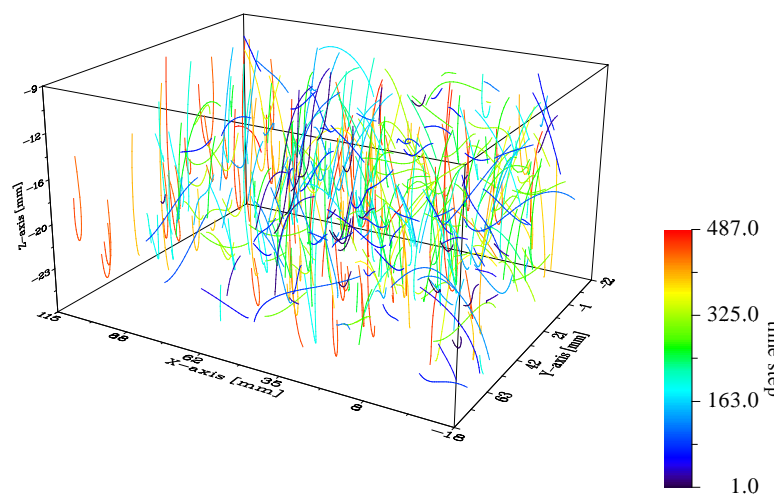
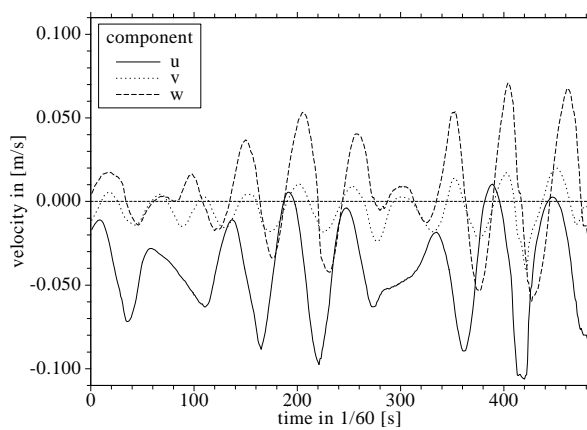Figure 6.10: Trajectories of figure 6.9 coded in time with color (time step in 1/60 s).

Figure 6.11: Velocity components as a function of time. All components are averaged over a time of 10 frames (0.17 s).

the curvature radius $R_{x_i,x_j} = 1/K_{x_i,x_j}$, where $x_i, x_j = \{(x,y),(y,z),(z,x)\}$ provide the plane of the 3D-Cartesian coordinate system) of orbital trajectories

$$K_{x_i,x_j,} = \frac{\dot{x}_i\ddot{x}_j - \dot{x}_i\ddot{x}_i}{(\dot{x}_i^2 + \dot{x}_j^2)^{3/2}} \tag{6.2}$$

can be calculated (which can not be obtained from the Euler-velocity field). For the 2D-PTV this was done by Hering [1996]. For the stereo PTV data this was not possible up to now due to a still to small amount of trajectories (less than 300 trajectories per image).

A consequence of the Lagrange-representation concerns the distribution of particles at a certain time $t_1 > t_o$ which determines the density of the velocity vectors in a given volume. This density of vectors can vary within the volume and time of observation. The Euler-representation of the flow field is a 'snapshot' of the flow. To determine the vector field the 'snapshot' is ideally an instant of time where in the real case a time interval is required to determine the vector field. The Euler-velocity field needs the vector from (at least) two subsequent image frames. If the density of velocity vectors is too low, it can be increased by increasing the time interval (more than two image frames) and by averaging over the time.

Many other measurement techniques such as LDA or PIV (section 3.1) obtain Euler-vector fields and for comparison of the results the Euler-velocity vector field must be calculated. The kinetic energy or the vorticity of the flow field are examples where the calculation of the Euler-velocity field is also required. For further processing of the data an interpolation of this velocity field $\vec{u} = \vec{u}(\vec{x},t_1)$ at time t_1 - which is the Euler-representation, equation (2.1) - on a regular grid is of advantage.

A frequently applied interpolation is the *adaptive Gaussian windowing* technique, introduced in the flow field visualization by Agüí and Jiminéz [1987]. The interpolated velocity field v_i is written as

$$v_i(\vec{x}_i) = \frac{\sum_{j=0}^{n-1} \vec{u}_j(\vec{x}_j) e^{\left(-\frac{\|\vec{x}_i - \vec{x}_j\|}{\sigma^2}\right)}}{\sum_{j=0}^{n-1} e^{\left(-\frac{\|\vec{x}_i - \vec{x}_j\|}{\sigma^2}\right)}} \tag{6.3}$$

where n is the number of particles and σ the width of the convolution kernel which was found by Agüí and Jiminéz [1987] to be proportional to the mean distance of the particles δ by the constant $c = 1.24$:

$$\sigma = c \cdot \delta$$

where in two dimensions $\delta = \sqrt{\frac{A}{\pi n}}$, A is the area of observation. In three dimensions the mean distance is $\delta = \left(\frac{3V}{4\pi n}\right)^{\frac{1}{3}}$ where V is the volume containing the particles.

This adaptive Gaussian windowing is a special case of the more general *normalized convolution* technique (see Knutsson and Westin [1993]). The generalized form of convolution is defined as

$$U(\overrightarrow{\xi}) = \sum_{\overrightarrow{x}} a(\overrightarrow{x}) B(\overrightarrow{x}) \odot c(\overrightarrow{\xi} - \overrightarrow{x}) T(\overrightarrow{\xi} - \overrightarrow{x}) \tag{6.4}$$

or in short from

$$U = \{aB \odot cT\} \tag{6.5}$$

where $\odot$ denotes some multi-linear operation (in standard convolution this is the scalar multiplication), $\overrightarrow{\xi}$ is the global spatial coordinate, $\overrightarrow{x}$ the local spatial coordinate, $T(\overrightarrow{\xi})$ is a tensor representing the input signal, $c(\overrightarrow{\xi})$ is a scalar function representing the certainty of $T(\overrightarrow{\xi})$, $B(\overrightarrow{x})$ is a tensor representing the operator filter basis and $a(\overrightarrow{x})$ is a positive scalar function representing the applicability of $B(\overrightarrow{x})$ (equivalent to the certainty).

The normalization factor for $U(\overrightarrow{\xi})$ is

$$N(\overrightarrow{\xi}) = \sum_{\overrightarrow{x}} a(\overrightarrow{x}) B(\overrightarrow{x}) \odot B^*(\overrightarrow{x}) c(\overrightarrow{\xi} - \overrightarrow{x}) \tag{6.6}$$

and the normalized convolution follows from equation (6.4) as

$$U_N = \frac{U(\overrightarrow{\xi})}{N(\overrightarrow{\xi})}. \tag{6.7}$$

The adaptive Gaussian windowing is obtained if the following operators are chosen:
The operator filter basis consists of only one positive invariant basis function with $B = 1$, the certainty is the delta function $c(\overrightarrow{\xi} - \overrightarrow{x}) = \delta(\overrightarrow{\xi} - \overrightarrow{x})$, the input signal is the velocity $T(\overrightarrow{\xi} - \overrightarrow{x}) = \overrightarrow{u}(\overrightarrow{\xi})$, and the applicability function is $a(\overrightarrow{x}) = e^{-\frac{\left\| \overrightarrow{x} - \overrightarrow{\xi} \right\|}{\sigma^2}}$.

This interpolation method is applied for a 'strong' wind-wave field shown in figure 6.12 (top). Because the density of trajectories is too low to determine the velocity field within a single time step (two subsequent image frames), the interpolation is extended over a time interval of 20 frames (0.3 s). The velocity as a function of time is shown in figure 6.12 (bottom). The case without wind stress is shown in figure 6.13. The wave amplitude (of gravitational waves) was approximately the same as
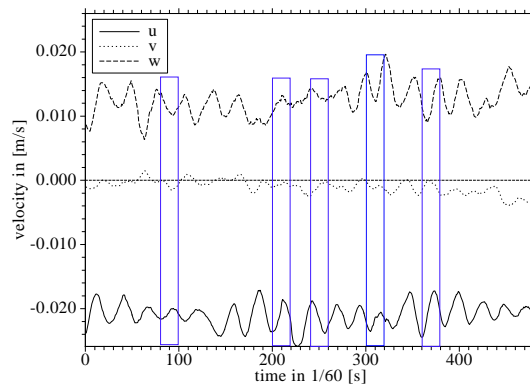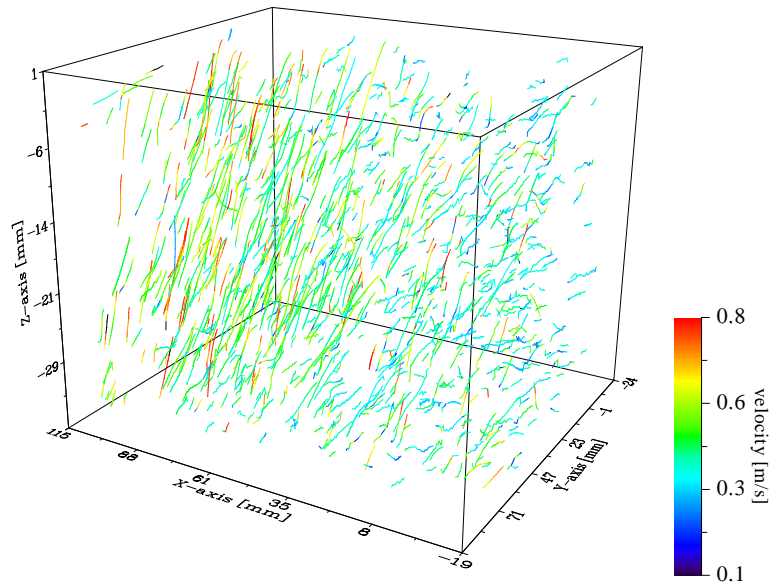
Figure 6.12: Top: Stereo trajectories of a 'strong wind-wave' field. Bottom: The velocity components as a function of time. The velocity is averaged over 10 frames (0.17 s). Euler-velocity fields are calculated for the marked (with boxes) time intervals (20 frames) and shown in figure 6.14.
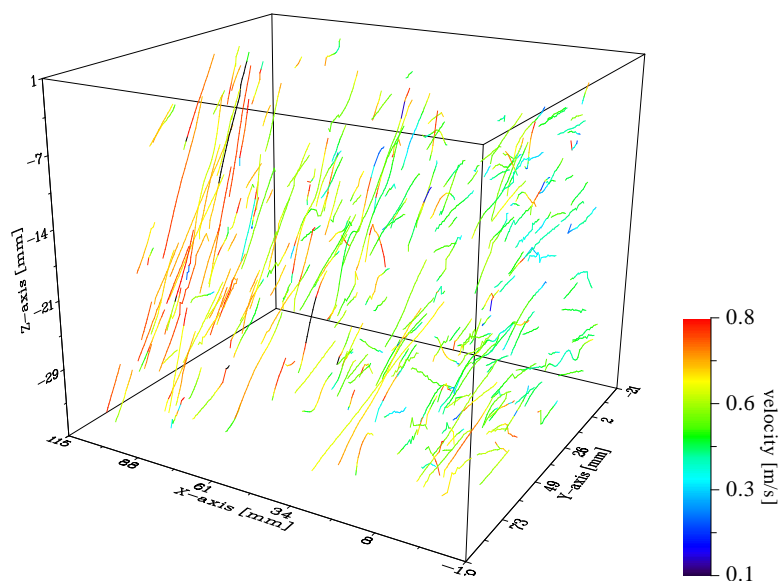
Figure 6.13: 'Wavy surface': Without wind generation and with decaying wave field from a series shown in figure 6.12, but same state as before.

in figure 6.12, as this wave field was obtained right after switching off the wind stress and decaying. Even if the number of obtained trajectories was lower in the case without wind stress as compared to the case with wind stress, the trajectories length is larger and the trajectory 'character' is rather straight as compared to the shorter, highly varying trajectories in figure 6.12. This is discussed quantitatively in the following.

The interpolated velocity field is shown in figure 6.14 for several time intervals marked in figure 6.12 (bottom) where the mean velocity component in x- and z-direction was subtracted. Interpretations for this velocity have to be done with care because of the temporal averaging which is around the period length of the main frequency component. But nevertheless some orbital movement can be noticed as a circular structure in the z,x-plane.

To characterize the flow field of the measuring series listed in section A over the whole time domain, the temporal averaged velocity components (table A.1) and the deviation from the mean velocity (table A.2) were calculated. The deviation from the mean velocity represents the mean turbulent[1] energy ('velocity fluctuations') in direction of the velocity components $E_d(dV) = \sqrt{\sum_i (u_{i,d} - \overline{u}_{i,d})^2}$ where the sum covers all velocity components in direction $d = x, y, z$ in the volume dV. The volume dV is divided according to figure 6.15 into stripes in the horizontal

---

[1] 'turbulent' in the sense of the deviation from the mean.
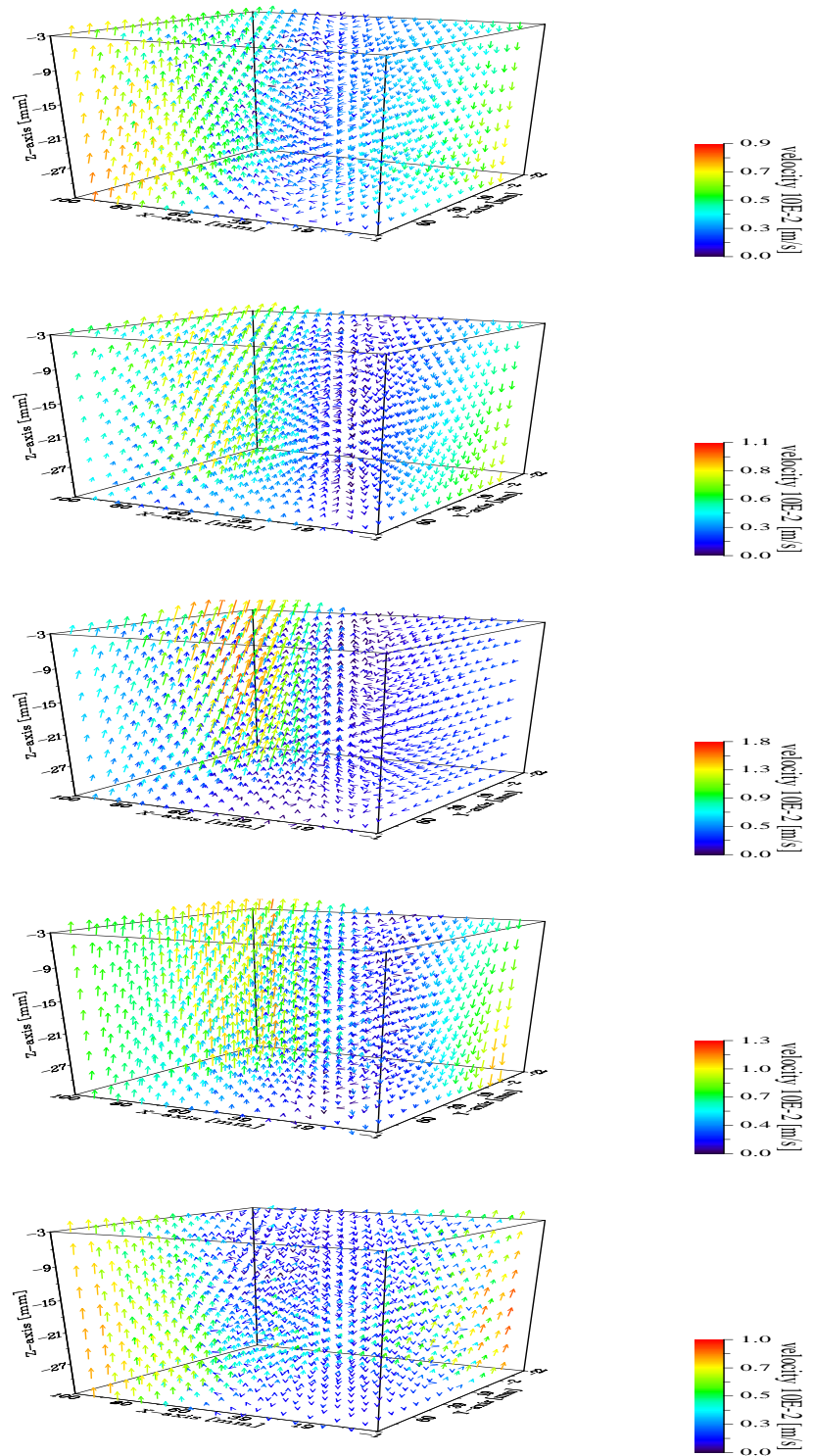
Figure 6.14: Interpolated velocity field (mean velocity subtracted) from trajectories of figure 6.12 (top) for the time intervals marked in 6.12 (bottom). The velocity is represented by the arrow length and for a better view also by the color.
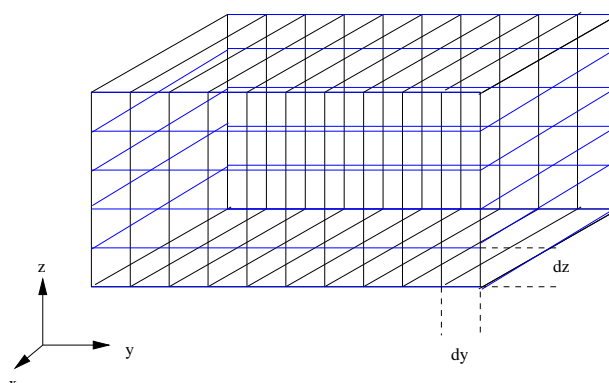
Figure 6.15: Volume of observation divided into 'boxes' from a grid. The volume is divided into slices along the z-axis (blue) and into stripes along the y-axis (black).

direction (division of the volume along the z-axis) and into slices along the y-axis (division of the volume along the y-axis). The averaging due to the wave amplitude has to be taken into account; while the volume division is constant, the wave height changes during the time of measurement. Therefore the averaging is done over the wave amplitude which was about 0.5 to 1.0 cm.

The results of table A.1 and table A.2 are summarized:

- The x-velocity component is decreasing with z (see figure 6.16 (1a) and (1b)),

- the z-velocity component is approximately the buoyancy velocity in the case of the wind generation being on,

- without wind stress on the water surface the z-velocity component is reduced by about 50 %, which means there must effectively be a downward flow.

- For the y-velocity component there are no significant differences. The main component is of course the one in the wind direction (x-direction). The main components related to the wave movement are in z- and x-direction. This can be seen if the velocity fluctuations are considered (figure 6.16 (2a) and (2b)). In y-direction the fluctuations are roughly 10 times smaller than in z-direction. Velocity fluctuations in x-direction are decreasing with depth in the case of wind stress, otherwise no tendency is observed.

Even if these results are obtained from preliminary measurements only, the effect of wind shear stress is clearly observed: There is a velocity gradient of the x-velocity component. If the surface would have been within the volume of observation and the position of the surface would have been known, the friction velocity u_* (section 2.2) could be determined. Furthermore a gradient of the velocity fluctuations $E_x(z)$
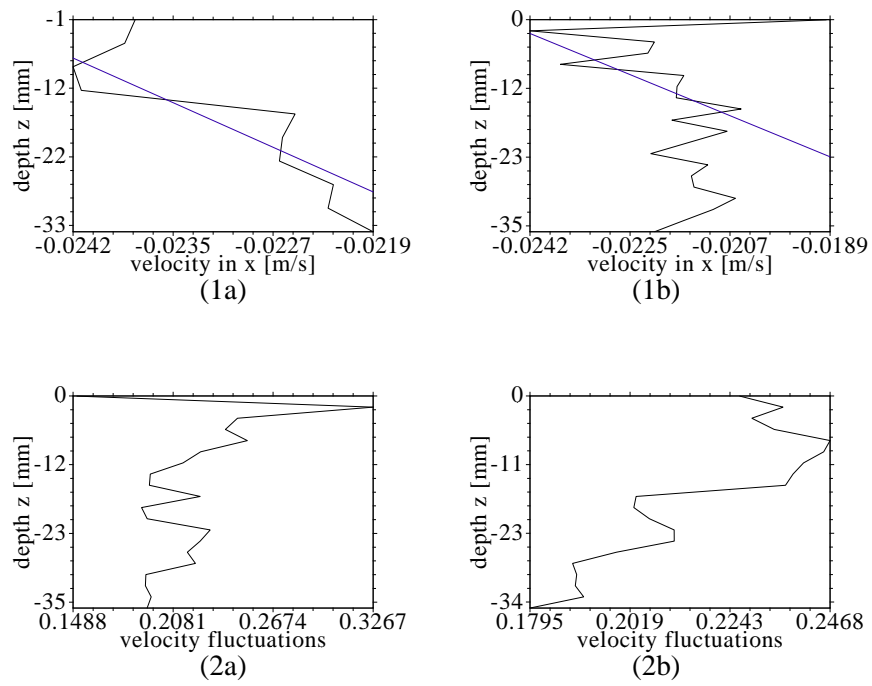
Figure 6.16: (1a), (1b): Dependency of velocity in x-direction on depth z (samples, number 4 and 5 of table A.1), (2a), (2b): Dependency of the velocity fluctuations E_x on z.

gives evidence for enhanced velocity fluctuations closer to the water surface for a wind induced wave field (with shear stress). The difference in the dominating frequency of the velocity between the two states with and without wind shear stress can not be explained simply by a higher mean velocity in the x-direction (along-wind component) causing the increased frequency. In a range within 10% there is no difference in the mean velocity in x-direction.

The influence of wind shear stress on the velocity field is qualitatively demonstrated. The next step is obviously an investigation aiming at quantitative results. Furthermore the combination of different techniques to obtain different physical properties in the same volume of observation and the same time is another step which will now be possible to take. Thus, the determination of the water surface shape (topology) is of importance for the stereo-PTV in the case of wave fields. The imaging slope gauge technique (ISG, see Balschbach [2000]) obtains this surface shape by the steepness of the surface. This combined measurement was already carried out in the predecessor of the newly constructed wind-wave flume for the 2D-PTV and should be extended to the third spatial dimension.

The stereo Particle Tracking Velocimetry was proven to be a valuable method for the three-dimensional flow visualization which allows to obtain a high spatial resolution of a Lagrange-velocity flow field. The fundamental techniques of stereo-PTV in wind-wave flumes have been evaluated and allow in the close future to increase the number and density of trajectories which is one of the most crucial aims.

Chapter 7

Outlook

A major task is to increase the trajectory density (number and length of trajectories). As this technique is new, improvements can be achieved almost in all parts such as experimental setup (in particular the illumination setup), the calibration procedure (in particular the Scheimpflug correction), the particle tracking procedure and the post processing of stereoscopic trajectories to obtain stereoscopic flow fields.

First measurements were performed at the AEOLOTRON wind/wave facility by applying new techniques such as the Scheimpflug stereo setup. The used Scheimpflug lens system lacked precise adjustment possibilities, thus complicating the search for an optimal depth of field range and also for the calibration procedure. A better lens system will be applied in the future.

Due to light refraction at the water surface (in the case of illumination from the top) the intensity of light in the volume of observation can vary depending on the curvature of the surface. Steep water waves, such as capillary waves, induce therefore a large variation in light intensity. If a color CCD camera would be used, a colored light source could improve the stereo correspondence search. The volume of observation would then be structured by the colors and particles could be matched in the correspondence search algorithm also by the color.

The calibration procedure is sub-pixel precise but depends on a calibration target with known position of world coordinates (world coordinates of landmarks such as cross middle points). A calibration procedure which does not require the knowledge of the world coordinates would simplify the procedure. Techniques such as described by Sturm and Maybank [1999] and Zhang [1998] requires the camera to observe a planar pattern shown at a few (at least two) different orientations.

A main improvement can be achieved with the extension of the stereo correlation procedure to the streaks. The stereo correlation of single streaks yields another very powerful criterion for the particle tracking algorithm. Streaks which are hidden by another particle for camera one can be visible separately for camera two and

therefore the trajectories can be reconstructed for camera one. This method is especially well suited if multiple cameras are applied. Ambiguities due to hidden streaks can thus be resolved.

For flow-field measurements close to the water surface it is necessary to determine the position of the surface boundary layer. The position of the particles can be obtained by the stereo-PTV, but if there are not enough particles visible in the surface boundary layer the position can not be determined. This is especially critical under the conditions of a wavy water surface. The position of the water surface could be obtained by imaging slope gauge techniques (Balschbach [2000]) or in a simpler setup by a capacity-wire method.

Finally the amount of data transfered from the frame grabber to the computer and to the hard disc storage is enormous for high frame rates and two cameras (120 Hz frame rate and a resolution, 512×512 pixels per image $\doteq 62$ MByte per second). An online compression using an FPGA (Free Programmable Gate Array) frame grabber can be applied to reduce the data by a factor of 100-200 (depending on the density of particles/streaks). This would allow to observe the flow field through a longer time interval.

Appendix A

Data tables

Several series of measurements have been taken. The analysis was done for the mean velocities ($\overrightarrow{u} = \begin{bmatrix} u & v & w \end{bmatrix}^T$ in x,y,z-components) and its deviation and tendency (inclining or declining with water depth) and are listed in table A.1. Furthermore the deviation from the mean velocity have been determined and are listed in table A.2. It represents the mean 'turbulent' energy in direction of the velocity components $E_d(dV) = \sqrt{\sum_i (u_{i,d} - \overline{u}_{i,d})^2}$ where the sum is over all velocity components in direction $d = x, y, z$ in the volume dV. The volume dV is divided according to figure 6.15 into stripes in the horizontal direction (division of the volume along the z-axis) and into slices along the y-axis (division of the volume along the y-axis).

In table A.1 the number of the measuring series and the direction of the column division (z,y) is found in the first row. The second row tells the wind state: 'on' means wind generator on (3-5m/s) and 'on+' a higher velocity (4-8m/s), 'on-' is the lowest wind velocity (2-4 m/s). In the third to the fifth row the velocity components and the deviations are listed. The tendency of the velocity is given only qualitatively: '- -' decreasing with depth z, '-' decreasing slightly, '++' increasing, '+' slightly increasing (samples are shown in figure 6.16).

Table A.2 lists only the variability and the tendency (same convention as A.1) of $E_d(dV)$ where $d = x, y, z$ and $dV = dz, dy$.

Comments:

- From series 1 to 5 the wind generation was turned on and slightly increased from 1 to 5.

- In series 6 the wind generation was turned off and the wave field decaying (from series 5).

- Series 7 was a test measurement without hydrogen bubbles to determine the behavior of 'pollution' (particles of different size).

series number/ direction dV	wind state	u in 10^{-2}[m/s]			v in 10^{-2}[m/s]			w 10^{-2}[m/s]		
		$\overline{u}$	$\Delta\overline{u}$		$\overline{v}$	$\Delta\overline{v}$		$\overline{w}$	$\Delta\overline{w}$	
1 / z	on	-0.82	-1.0/-0.6		-0.07	-0.1/-0.0		1.11	0.8/1.3	++
1 / y			-1.0/-0.2	- -		-0.1/-0.0			1.0/1.3	
2 / z	on	-1.75	-1.9/-1.7	- -	-0.15	-0.2/-0.1		1.06	0.8/1.2	
2 / y			-1.8/-1.6	-		-0.2/-0.1			0.5/1.1	
3 / z	on	-2.25	-2.3/-2.2		-0.17	-0.2/-0.1		1.06	0.8/1.3	
3 / y			-2.5/-2.1	-		-0.3/-0.1	+		0.7/1.4	++
4 / z	on -	-2.28	-2.4/-2.2	- -	-0.12	-0.1/0.1		1.37	1.2/1.5	
4 / y			-2.5/-2.1			-0.2/-0.1			0.6/1.7	++
5 / z	on	-2.16	-2.3/-2.0	- -	-0.10	-0.2/-0.1		1.24	1.0/1.4	
5 / y			-2.4/-2.0	- -		-0.2/-0.0			0.6/1.3	
6 / z	off	-2.86	-3.0/-2.7		-0.10	-0.2/-0.0	+	1.67	1.3/1.9	
6 / y			-3.0/-2.7			-0.2/-0.0			0.5/2.0	++
7 / z	on +	-1.00	-1.1/-0.8		0.35	0.1/0.4		0.48	0.4/0.6	
7 / y			-1.0/-0.8			0.2/0.6			0.1/0.8	
8 / z	off	-2.5	-4.8/-1.8	- -	-0.20	-0.5/-0.1		0.71	0.4/1.0	
8 / y			-3.0/-2.0			-0.6/0.1			0.1/1.0	
9 / z	off	-2.8	-2.9/-2.8		-0.27	-0.3/-0.2		0.56	0.5/0.6	
9 / y			-2.9/-2.8			-0.4/-0.1	+		0.3/0.6	
10 / z	off	-2.02	-2.1/-1.9		-0.02	-0.1/0.0		0.28	0.2/0.3	
10 / y			-2.1/-1.9			-0.1/0.0			0.2/0.3	
11 / z	off	-2.16	-2.2/-2.1		-0.11	-0.2/-0.1		0.36	0.3/0.4	
11 / y			-2.3/-2.1			-0.3/-0.0	+		0.1/0.5	+

Table A.1: Average velocity of in y and z direction and its variation. The averaging is done according to figure 6.15.

series number/ direction dV	E_x [m/s]		E_y [m/s]		E_z [m/s]		E_{sum} [m/s]	
1 / z	0.03/0.07		0.003/0.08		0.04/0.06		0.07/0.14	
1 / y	0.01/0.04	++	0.003/0.007		0.04/0.07		0.07/0.11	+
2 / z	0.07/0.11	++	0.04/0.07		0.05/0.06		0.12/0.17	+
2 / y	0.07/0.22	++	0.004/0.007		0.03/0.06		0.12/0.27	+
3 / z	0.12/0.16	+	0.002/0.008		0.03/0.06		0.17/0.20	
3 / y	0.12/0.17	++	0.004/0.007		0.03/0.06		0.16/0.23	++
4 / z	0.13/0.18	++	0.003/0.007		0.06/0.08		0.18/0.3	++
4 / y	0.12/0.3	++	0.003/0.006		0.03/0.09	++	0.16/0.4	+
5 / z	0.12/0.19	++	0.007/0.013		0.06/0.09		0.19/0.27	++
5 / y	0.18/0.46	++	0.007/0.01		0.05/0.16	++	0.27/0.63	+
6 / z	0.19/0.26		0.008/0.01		0.08/0.14		0.30/0.39	
6 / y	0.18/0.46	++	0.007/0.012		0.05/0.16	++	0.27/0.63	+
7 / z	0.03/0.05		0.015/0.027		0.04/0.08		0.10/0.14	
7 / y	0.30/0.46		0.012/0.026		0.04/0.08		0.09/0.13	
8 / z	0.23/0.78	++	0.04/0.06		0.10/0.35	++	0.37/1.00	++
8 / y	0.22/0.43		0.04/0.06	-	0.18/0.33	++	0.60/0.80	
9 / z	0.20/0.21		0.007/0.01		0.03/0.04		0.23/0.25	
9 / y	0.19/0.21		0.006/0.011		0.02/0.04		0.23/0.25	
10 / z	0.11/0.12		0.008/0.014		0.03/0.06		0.16/0.18	
10 / y	0.11/0.13		0.008/0.012		0.02/0.05		0.16/0.18	
11 / z	0.11/0.13		0.004/ 0.006		0.01/0.03	++	0.14/0.16	
11 / y	0.11/0.13		0.003/0.005		0.01/0.02	-	0.13/0.16	

Table A.2: Velocity and fluctuations in 'boxed' volume according to figure 6.15.

- Series 8 to 9 was a decaying wave field (wind state off) from series 7.

Appendix B

Linearized wave equation

A simple case of fluid flow should be discussed. The three dimensional case is already far from being simple and therefore the two dimensional case is considered.

If an irrotational flow of velocity $\vec{u} = [u(x,y,t),\, v(x,y,t)]$ is considered ($\nabla \times \vec{u} = 0$ $\Leftrightarrow \frac{\partial v}{\partial x} - \frac{\partial u}{\partial y} = 0$), there exists a *velocity potential*

$$\vec{u} = \nabla \phi.$$

By virtue of the incompressibility condition $\nabla \cdot \vec{u} = 0$ the velocity potential satisfy the Laplace's equation

$$\Delta \phi = 0. \tag{B.1}$$

The velocity potential is constant along the *streamline* ψ ($(\vec{u} \cdot \nabla)\psi = 0$), where the velocity can be expressed with the Cauchy-Riemann equations (of complex variable theory) as

$$u = \frac{\partial \phi}{\partial x} = \frac{\partial \psi}{\partial y}, \quad v = \frac{\partial \phi}{\partial y} = -\frac{\partial \psi}{\partial x}. \tag{B.2}$$

A further simplification is the assumption of *small-amplitude* waves where the water surface displacement $y = \eta(x,t)$ and the associated fluid velocity u, v are small[1]. The kinematic boundary condition[2] at the free surface $\frac{\partial \eta}{\partial t} + u \frac{\partial \eta}{\partial x} = v$ then simplifies to

$$v(x,t) = \frac{\partial \eta(x,t)}{\partial t}. \tag{B.3}$$

Applying a Taylor expansion of v around $\eta = 0$ yields $v(x,0,t) = \partial \eta / \partial t$. The same linearization is applied to the dynamic boundary condition[3] and simplifies

---

[1] $u \frac{\partial \eta}{\partial x}$ is small compared to v (as in the kinematic boundary condition) and $u^2 + v^2$ small compared to $g\eta$ (as in the dynamic boundary condition).

[2] Fluid 'elements' at the surface must remain on the surface.

[3] 'pressure condition': if the fluid is inviscid, the pressure p is equal to the atmospheric pressure at $y = \eta(x,t)$.

$\frac{\partial \phi}{\partial t} + \frac{1}{2}(u^2 + v^2) + g\eta = 0$ to

$$\frac{\partial \phi}{\partial t} + g\eta = 0 \; on \; y = 0 \tag{B.4}$$

(where g is the gravitational force).

A sinusoidal traveling wave at the surface is

$$\eta(x,t) = A\cos(kx - \omega t) \tag{B.5}$$

where A is the amplitude of the surface displacement, k the wave number and ω the frequency.

The velocity potential

$$\phi = f(y)\sin(kx - \omega t)$$

is consistent with the boundary conditions B.3 and B.4. It has to satisfy the Laplace equation (B.1) which leads to

$$\frac{\partial^2 f}{\partial y^2} - k^2 f = 0$$

and its solution

$$f = Ce^{ky} + De^{-ky}.$$

If the water is of infinite depth it must be chosen $D = 0$ and it follows $\phi = Ce^{ky}\sin(kx - \omega t)$. The constant C can be obtained by substituting ϕ and η (equation. B.5) into the boundary conditions B.3 and B.4 and the result is

$$\phi = \frac{A\omega}{k}e^{ky}\cos(kx - \omega t) \tag{B.6}$$

with the dispersion relation $\omega^2 = gk$.

The *particle paths* can be obtained from equations (B.2) and (B.6)

$$u = A\omega e^{ky}\cos(kx - \omega t), \;\; v = A\omega e^{ky}\sin(kx - \omega t). \tag{B.7}$$

Assuming a small depart (x', y') of the particle from its mean position $(\bar{x}, \bar{y})$ the velocity can be approximated by

$$\frac{dx'}{dt} = A\omega e^{k\bar{y}}\cos(k\bar{x} - \omega t), \;\; \frac{dy'}{dt} = A\omega e^{k\bar{y}}\sin(k\bar{x} - \omega t)$$

and results in

$$x' = -Ae^{k\bar{y}}\cos(k\bar{x} - \omega t), \;\; y' = Ae^{k\bar{y}}\sin(k\bar{x} - \omega t). \tag{B.8}$$

The particles describe circular paths and the radius decreases exponentially with depth y. As the fluid velocity also decreases exponentially, the energy of the surface water wave is mainly contained within half a wavelength below the surface.

Appendix C

Depth of field, depth of focus

The equation for par-axial lenses of focal length f is

$$\frac{1}{f} = \frac{1}{d_o} + \frac{1}{d_i}$$

where d_o is the distance of the object and d_i the distance of the image from the lens plane. Only objects at location d_o are imaged focused on the image plane at distance d_i, if the object is moved from its location by Δd_o to location $d'_o = d_o + \Delta d_o$ the object is out of focus. In a zero order approximation this out of focus is described by a blurring circle of radius ε. The *f-number O* characterizes the depth of field through the ratio of focal length f to the diameter R of the lens, $O = f/2R$. From geometry the following relation is valid

$$\frac{\varepsilon}{R} = \frac{d_i}{d'_i} - 1 = \frac{d_i}{d_o} \frac{\Delta d_o}{d'_o} \tag{C.1}$$

where the magnification $M = d_i/d_o$ and $\frac{d'_i - d_i}{d'_i} = M \frac{d'_o - d_o}{d'_o}$.

The *depth of field* Δd_o is determined through an acceptable blur radius ε_c:

$$\Delta d_o = \frac{d_o}{\frac{Mf}{2O\varepsilon_c} - 1}.$$

If $2O\varepsilon_c \ll Mf$ then the depth of field is

$$\Delta d_o = \frac{2O\varepsilon_c}{Mf} d_o.$$

Moving the image plane instead of the object plane results also in defocusing. In the same way as for the depth of field, the *depth of focus* is determined through

an acceptable blur radius ε_c on the image plane. Taking equation (C.1) and if $2O\varepsilon_c \ll f$ the depth of focus is defined as

$$\Delta d_i = \frac{2O}{f} d_i \varepsilon_c.$$

The relation between the depth field of and the depth of focus is

$$\Delta d_o = M^2 \Delta d_i.$$

Appendix D

Basics of the finite element method

The finite element method (FEM) offers systematic rules to produce stable numerical schemes. This method is well suited to handle two- and three-dimensional structures even with complex structures and boundaries.

The starting point of the finite element method (FEM) is the *variational equation*[1] (see figure D.1):

Find $u \in V$ so that

$$a(u,v) = f(v) \qquad \forall v \in V$$

where V is a given function space.

A simple example is the heat conductivity equation

$$-\Delta T = q \qquad \text{in } \Omega$$
$$T = 0 \qquad \text{auf } \Gamma. \tag{D.1}$$

where T is the temperature and $\Gamma = \partial \Omega$. The body is restricted to the area Ω.

If the solution of equation (D.1) for T is u and $v \in V$ where V is a set of all differentiable functions in Ω, the integral equation can be written as

$$\int_\Omega \underbrace{(\Delta u)v d\Omega}_{a(u,v)} = \int_\Omega \underbrace{qv}_{f(v)} \, d\Omega$$

The boundary value problem is transformed into a symmetric bi-linear form, the variational equation[2]

$$a(u,v) = f(v) \qquad \forall v \in V \tag{D.2}$$

---

[1] Variational problem: $J(v) \rightarrow min! \, \forall v \in V$,
Ritz method: $J(v_h) \rightarrow min! \, \forall v_h \in V_h$,   Galerkin-Ritz: $a(u_h,v_h = f(v_h) \, \forall v_h \in V_h$.

[2] considering the boundary conditions on Γ and applying the Gauß integral theorem.
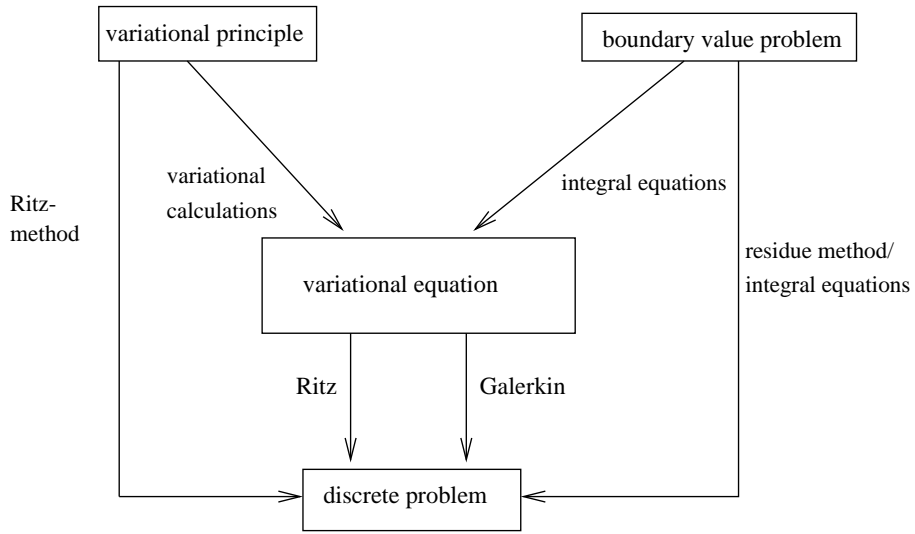
Figure D.1: Discretization methods. For the finite element method the variational equation is the starting point.

where $u \in V$ is searched for. This functional space V is discretized by the *Galerkin discretization*:

The functional space V is discretized in N-dimensional sub-spaces.

$$V_h \subset V$$

The approximate solution for $u_h \in V_h$ can be expressed as

$$u_h = \sum_{i=1}^{N} u_i w_i$$

with the base functions $w_i \in V$ for V_h and the constants u_i. The discrete problem of equation (D.2) is then written as the so called weak formulation

$$a(u_h, v_h) = f(v_h) \qquad \forall v_h \in V_h$$

with base function $w_{ij}(x_k, y_l) = \begin{cases} 1 & \text{for } i = k, \, j = l \\ 0 & \text{otherwise} \end{cases}$

The fundamentals of the finite element method are summarized as follows:

- Choose w_i with $i = 1 \ldots N$ which deviate from zero only inside Ω_i not equal to zero, and Ω_i, Ω_j with as few as possible common points.
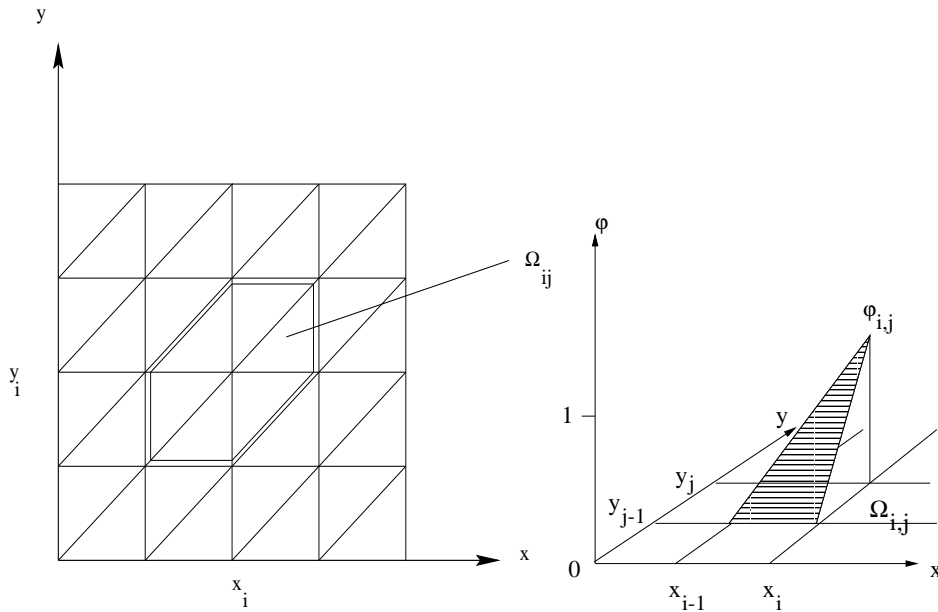
Figure D.2: Illustration of the construction of the base function. Left: Each square is divided into two triangles. The discretized space V_h is characterized by functions inside the triangle which are linear in x and y (right figure). Outside of Ω_{ij} the base functions $w_{ij}(x,y)$ are zero.

- Construct $a(w_i, w_j)$, f_j, and solve $\sum_{i=1}^{N} a(w_i, w_j) u_i = f_j$, $\qquad j = 1, \cdots, N$.

- Approximate the solution

$$u_h = \sum_{i=1}^{N} u_i w_i$$

The 'weak formulation' of the Navier-Stokes equation is formulated in the following:

Find velocity $u \in V$ and pressure $p \in Q$ so that

$$\begin{aligned}
\left(\frac{\partial u}{\partial t}, v\right) + (u \cdot \nabla u, v) - \nu (\nabla u, \nabla v) + (p, \nabla v) &= (f, v) & \forall v \in V, \\
(\nabla \cdot u, v) &= 0 & \forall q \in Q,
\end{aligned}$$

with $V = H_0^1(\Omega)$ and $Q = L_2(\Omega)$.

The Galerkin discretization step is then applied: $V_h \subset V$ and $Q_h \subset Q$ with grid parameter h.

To achieve a stable discretization, so called stabilization terms have to be added.

Functional space for FEM

The variability in the choice of the functional space entails the flexibility of the finite element method which is superior to other methods such as finite differences or finite volume methods. General properties of the discrete space V_h for FEM are summarized in the following:

The weighting functions w_{ij} are continuous, but not continuously differentiable (for example on the border of Ω_{ij} or on the sides of the triangles, see figure D.2). A concept of derivation operator is therefore introduced which allows to partly differentiate partly differentiable functions. Depending on the variational equation and the associated boundary conditions the functional space V is constructed. In the previous sample the functional space is $V = H_0^1(\Omega)$ with the boundary condition $u|_{\partial\Omega} = 0$ (Dirichlet) where $V = H^1(\Omega)$ is the *Sobolev-space* of first order, and the lower index of H_0^1 symbolizes that the Dirichlet boundary condition is applied[3].

Definition of Sobolev-space: A function v belongs to $H^1(\Omega)$, if it belongs to $L^2(\Omega)$ and the generalized derivative $(\frac{\partial v}{\partial x}, \frac{\partial v}{\partial y})$ does also belong to the $L^2(\Omega)$.

The space $H_0^1(\Omega)$ is of importance for solving elliptic differential equations of second order and Dirichlet boundary condition.

---

[3]The boundary conditions are partly enclosed in the functional space and partly enclosed in the variational equation, which is a characteristic of the FEM.

Acknowledgements

Bibliography

J. Agüí and J. Jiminéz. On the performance of particle tracking. *J. Fluid. Mech.*, 185:447–468, 1987.

G. Balschbach. *Untersuchung statistischer und geometrischer Eigenschaften von Windwellen und ihrer Wechselwirkungen mit der wasserseitigen Grenzschicht.* PhD thesis, University Heidelberg, Heidelberg, Germany, 2000.

R. Becker and M. Braack. *Numerical Linear Algebra with Applications (Special Issue)*, chapter Multigrid techniques for finite elements on locally refined meshes. Wiley,Chichester, 2000.

M. Bentele. Rekonstruktion und Visualisierung dynamischer Prozesse. Master's thesis, University Heidelberg, Heidelberg, Germany, 1998.

M. Born and E. Wolf. *Principles of Optics*. 6th edition. Pergamon Press, Oxford, 1984.

R. Bösinger. Messungen zur Schmidtzahlabhängigkeit des Gasaustausches. Master's thesis, University Heidelberg, Heidelberg, Germany, 1986.

M. Coantic. A model of gas transfer across air-water interfaces with capillary waves. *J. Geophys. Res.*, 91(C3):3925–3943, 1986.

G. Csanady. The role of breaking wavelets in air-sea transfer. *J. Geophys. Res.*, 95 (C1):749–759, 1990.

P. Danckwerts. Significance of liquid-film coefficients in gas absorption. *Industrial and Engineering Chemistry*, 43:1460–1467, 1951.

J. Dieter, R. Bremeyer, F. Hering, and B. Jähne. Flow measurements close to the free air/sea interface. In *Proceedings to the Seventh International Symposium on Applications of Laser Techniques to Fluid Mechanics*, 1994.

S. Eichkorn, T. Münsterer, U. Lode, and B. Jähne. *Handbook of Computer Vision and Applications*, volume 3, chapter Fluorescence Imaging of Air-Water Gas Exchange, pages 647–661. Academic Press, San Diego, 1999.

D. Engelmann, C. Garbe, M. Stöhr, P. Geissler, F. Hering, and B. Jähne. Stereo Particel Tracking. In *Proceedings of the 8th International Symposium on Flow Visualization, Sorrento, Italy, September 1-4,*, pages 240.1–249.9, 1 Sept. 1998.

D. Engelmann, C. Garbe, M. Stöhr, and B. Jähne. Three dimensional flow dynamics beneath the air-water interface. In *Proceedings of the Symposium on the Wind-Driven Air-Sea Interface, Sydney, Australia, 11-15 January 1999*, page 181, 11 Jan. 1999a.

D. Engelmann, M. Stöhr, C. Garbe, and F. Hering. *Handbook of Computer Vision and Applications*, volume 3, chapter Particle-Tracking Velocimetry, pages 663–697. Academic Press, San Diego, 1999b.

O. Faugeras and G. Toscani. Camera calibration for 3D computer vision. In *Proc. Int. Workshop on Industrial Application of Machine Vision and Machine Intelligence, Silken, Japan*, pages 240–247, 1987.

O. Faugers. *Three-Dimensional Computer Vision, A Geometric Viewpoint*. MIT Press, Cambridge, Massachusetts, 1993.

J. Fryer. *Handbook of Non-Topographic Photogrammetry*, chapter Camera calibration in non-topographic photogrammetry, pages 59–69. American Society of Photogrammetry and Remote Sensing, Falls Church, VI, USA, 1989.

C. Garbe. Entwicklung eines Systems zur dreidimensionalen Particle Tracking Velocimetry mit Genauigkeitsuntersuchungen und Anwendungen bei Messungen in einem Wind-Wellen Kanal. Master's thesis, University Heidelberg, Heidelberg, Germany, 1998.

P. Geissler and T. Scholz. *Handbook of Computer Vision and Applications*, volume 3, chapter Depth-from-Focus for the Measurement of Size Distributions of Small Particles, page 670. Academic Press, San Diego, 1999.

M. Gharib and C. Willert. Particle tracing revised. In *Proceedings, 1st National Fluid dynamics Congress, Cincinnati/Ohio, AIAA-88-3776-CP.*, 1988.

I. Grant. Particle image velocimetry: A review. In *Proc. Inst. Mech. Engrs.*, volume 211 of C, pages 55–76, 1997.

F. Hering. *Lagrangesche Untersuchungen des Strömungsfeldes unterhalb der wellenbewegten Wasseroberfläche mittels Bildfolgenanlyse*. PhD thesis, University Heidelberg, Heidelberg, Germany, 1996.

F. Hering, G. Balschbach, and B. Jähne. A Novel System for the Combined Measurement of Wave- and Flow-Fields Beneath Wind Induced Water Waves. In *XVIII ISPRS-Congress Vienna, 9-19 July 1996*, 9 July 1996.

F. Hering, C. Leue, D. Wierzimok, and B. Jähne. Particle tracking velocimetry beneath water waves, part II: water waves. *Experiments in Fluids*, 24(1):10–16, Jan. 1998.

L. Hesselink. Digital image processing in flow visualization. *Ann. Rev. Fluid Mech*, 20:421–485, 1988.

J. Hinze. *Turbulence.* McGraw-Hill, New York, 1959.

J. Höhle. Zur Theorie und Praxis der Unterwasser-Photogrammetrie. Schriften der DGK. Reihe C, Heft 163, DGK, Germany, 1971.

W. Huber. Aufbau eines gaschromatografischen Meßsystems für Gasaustauschmessungen; Windkanalmessungen zur Schmidtzahl und Wellenbildabhängigkeit des Gasaustausches. Master's thesis, Univ. Heidelberg, Heidelberg, Germany, 1984. pp. 93.

B. Jähne. *Zur Parametrisierung des Gasaustausches mit Hilfe von Laborexperimenten*. PhD thesis, University Heidelberg, Heidelberg, Germany, 1980.

B. Jähne. *Transfer Processes across the Free Water Surface.* Habilitation, Institute of Environmental Physics, University Heidelberg, 1985.

B. Jähne. *Digitale Bildverarbeitung*. 4. Auflage. Springer Verlag, 1997.

H. Klages. Beiträge zur experimentellen Untersuchung und Anwendung von Heissluftsonden. Bericht 14/1977, Max-Planck Institut für Strömungsforschung Göttingen, 1977.

R. Klette, A. Koschan, and K. Schlüns. *Computer Vision.* Vieweg, 1996.

J. Klinke. *Optical measurements of small-scale wind-generated water surface waves in the laboratory and the field.* PhD thesis, University Heidelberg, Heidelberg, Germany, 1996.

H. Knutsson and C. Westin. Normalized and Differential Convolution. Methods for Interpolation and Filtering of Incomplete and Uncertain Data. In *CVPR conference, New York City, USA, June 1993, IEEE*, pages 515–523. IEEE, June 1993.

M. Koochesfahani and P. Dimotakis. Laser induced fluorescence measurements of mixing fluid concentration in a liquid shear layer. *AiAA J.*, 23:1699–1707, 1985.

M. Koochesfahani and P. Dimotakis. Mixing and chemical reactions in a turbulent liquid mixing layer. *J. Fluid Mech.*, 170:83–112, 1986.

C. Leue. Segmentierungsverfahren bei der Strömungsvisualisierung. Master's thesis, University Heidelberg, Germany, 1996.

H. Maas. *Digitale Photogrammetrie in der dreidimensionalen Strömungsmeßtechnik.* PhD thesis, University Zürich, Switzerland, 1992.

J. Matas and J. Kittler. Spatial and Feature Clustering: Applications in Image Analysis. In *Proc. of 6th International Conference on Computer Analysis of Images and Patterns, CAIP '95, Prague, September 6-8*, volume 970 of *in Lecture Notes in Computer Science*. Springer Verlag, Berlin, 1995.

T. Melen. *Optical 3-D Measurement Techniques II*, chapter Extracting Physical Camera Parameters from the 3 by 3 Direct Linear Transformation Matrix., pages 355–365. Herbert Wichmann Verlag, Zürich, Switzerland, Oct. 1993.

A. Monin and A. Yaglom. *Statistical Fluid Mechanics, Mechanics of Turbulence*, volume 2. Cambridge: MIT Press, 1975.

S. Müller, A. Prohl, R. Rannacher, and S. Turek. Implicit time-discretization of the non-stationary incompressible Navier-Stokes equations. In Wittum, G., Hackbusch,W., editor, *Proc, 10th GAMM-Seminar, Kiel, January 14-16*. Vieweg, 14 Jan. 1994.

T. Münsterer. *LIF Investigation of the Mechanism Controlling Air-Water Mass Transfer.* PhD thesis, University of Heidelberg, Heidelberg, Germany, 1996.

T. Netsch. *Dreidimensionale Particel Tracking Velocimetry.* PhD thesis, University Heidelberg, Heidelberg, Germany, 1995.

H. Oertel and H. Oertel. *Optische Strömungsmesstechnik.*, chapter 2, page 279. ISBN 3 7650 1012 X. G. Braun Verlag GmbH Karlsruhe, 1989.

R. Rannacher and S. Turek. A simple nonconforming quadriliteral Stokes element. *Numer. Math. Part. Diff. Equ.*, (8):97–11, 1992.

M. Schäfer and S. Turek. *Flow Simulation with High-Performance Computers II*, volume 52 of *Notes on Numerical Fluid Mechanics*, chapter Benchmark computations of laminar flow around cylinder, pages 547–566. Vieweg, 1996.

R. Schwarte, H. Heinol, B. Buxbaum, T. Ringbeck, Z. Xu, and K. Hartmann. *Handbook of Computer Vision and Applications*, volume I, chapter Principles of Three-Dimensional Imaging Techniques., page 469. Academic Press, San Diego, 1999.

T. Shih and W. Faig. Physical interpretation of the extended DLT-model. In *Proceedings of ASPRS Fall Convention*, pages 385–394, Reno, Nevada, 1987. American Society for Photogrammetry and Remote Sensing.

G. Spedding and Rignot. Performance analysis of grid interpolation techniques for fluid flows. *Exp. Fluids*, (15):417–430, 1990.

M. Stöhr. Entwicklung dreidimensionaler Particle Tracking Velocimetry zur Messung der Zweiphasenströmung in Gas-Flüssig-Reaktoren. Master's thesis, University Heidelberg, Heidelberg, Germany, 1998.

P. Sturm and S. Maybank. On Plane-Based Camera Calibration: A General Algorithm, Singularities, Applications. In *IEEE Computer Society Conference on Computer Vision and Pattern Recognition*, volume 1, pages 432–7, Los Alamitos, CA, USA, 1999. IEEE Comput. Soc.

J. Tschiersch and B. Jähne. Gas exchange through a rough water surface in a circular wind tunnel; wave characteristics under limited and unlimited fetch; preliminary results. In L. Broecker, H.-C. and Hasse, editor, *Symp. Capillary Waves Gas Exch.*, number 17, pages 63–70, Hamburg, Germany, 1980. Univ. Hamburg Press.

A. Tsinober, E. Kit, and T. Dracos. *Measuring Invariant (Frame Independent) Quantities Composed of Velocity Derivatives in Turbulent Flows.* Springer Verlag, Berlin/Heidelberg, advances in Turbulence 3 edition, 1991.

S. Turek. *Efficient solvers for incompressible flow problems: An algorithmic and computational approach.* LNCSE 6. Springer-Verlag, 1999.

D. Uttenweiler and R. Fink. *Handbook of Computer Vision and Applications*, volume I, chapter Dynamic Fluorescence Imaging., page 323. Academic Press, San Diego, 1999.

W. Vetterling, W. Press, S. Teucholsky, and B. Flannery. *Numerical recipes in C*. Cambridge University Press, 1992.

J. Wiedmann. *Laser-Doppler-Anemometrie.* Springer Verlag, Berlin, 1984.

D. Wierzimok and F. Hering. Quantitative Imaging of Transport in Fluids with Digital Image Processing, 1993.

H. Wolf. Aufrüstung von 2D-Bildverarbeitungssystemen zu 3D-Systemen mit aktiver strukturierter Beleuchtung. In *Tagungsunterlagen {"}Aktuelle Entwicklung und industrieller Einsatz der Bildverarbeitung{"}*, page 1. MIT Management, Aachen, 1996.

Z. Zhang. A Flexible New Technique for Camera Calibration. Technical Report MSR-TR-98-71, Microsoft Research, Redmond, WA 98052, 1998.